Fresh Water Forcing of the North Atlantic.

by

Stella M. Aura

A thesis submitted to the
Faculty of Graduate Studies and Research
in partial fulfilment of the requirements for the degree of

MASTER OF SCIENCE

Department of Atmospheric and Oceanic Sciences
McGill University
Montréal, Québec

Abstract

Several numerical experiments are carried out using the Bryan-Cox Ocean General Circulation Model to investigate the variability of the North Atlantic thermohaline circulation under steady, non-zonal, surface forcing and realistic geometry. To this end the annual mean surface forcing fields were derived from the climatological data sets of Levitus (1982), Hellerman and Rosenstein (1983) and, Schmitt et al. (1989). Further, Arctic freshwater flux, an important part of the hydrological cycle within the North Atlantic Deep Water formation region, is taken into account.

It is found that under present-day climatological surface forcing the system may oscillate at interdecadal period. The mechanism driving the oscillations is linked to changes in both the horizontal and vertical extent of convection in the northern "Labrador Sea". The structure of the surface freshwater flux forcing plays a major role in both the initiation and sustenance of the interdecadal oscillations. Allowing for a freshwater flux into the northern region of the "Labrador Sea" inhibits the interdecadal variability. The oscillations, however, appear, relatively insensitive to Arctic fresh water transport into the "Greenland Sea".

A detailed three-dimensional discussion of the physics behind the interdecadal oscillations is presented.

Résumé

Plusieurs expériences numériques ont été effectuées en utilisant le modèle Bryan-Cox de la circulation générale de l'océan afin d'étudier la variabilité de la circulation thermohaline de l'océan nord Atlantique en imposant des conditions non-zonales stables en surface et une géométrie réaliste. Dans ce but, les paramètres utilisés comme conditions limites en surface ont été dérivés des données climatologiques (Levitus (1982), Hellerman et Rosenstein (1983), et Schmitt et al. (1989)). De plus, on a tenu compte du flux d'eau douce arctique qui constitue une partie importante du cycle hydrologique dans les régions où se forme la masse d'eau profonde de l'océan nord Atlantique.

Il s'avère qu'en utilisant des données climatologiques, le système peut osciller à une période interdécadaire. Le mécanisme de forçage de ces oscillations est lié aux changements de l'étendue horizontale et verticale de la convection dans le nord de la "mer du Labrador". La structure de la condition limite du flux d'eau douce joue un rôle capital pour déclencher puis soutenir ces oscillations interdécadaire. La variabilité interdécadaire est inhibée par le flux d'eau douce dans le nord de la "mer du Labrador". Les oscillations, cependant, apparaissent relativement insensibles au transport d'eau douce arctique dans la "mer du Groenland".

Une discussion détaillée de la physique tridimensionnelle de ces oscillations est présentée.

Acknowledgements

I sincerely thank my supervisor, Dr. Andrew J. Weaver for the devoted support and encouragement he accorded me throughout the course of this research work. I am indebted to Von Jochem Marotzke for providing us with the Schmitt et al. (1989) Evaporation minus Precipitation data. I am grateful to Paul Myers and Tertia Hughes for useful discussions and comments and to Thierry Reynaud and Robert Matte for editting the Résumé. To Anna Koziol I say "dziękuję" and to Njuki Mureithi "asante sana" for their invaluable assistance. A special word of thank you is extended to Vicki Loschiavo and Barbara Batt for their moral support.

Financial support was provided through a Canadian International Development Agency (C.I.D.A.) scholarship under the Kenya-Canada General Training Fund (G.T.F.) programme and was administered by the Kenya High Commission (Ottawa).

Table of Contents

List of Figures

List of Tables

1 Introduction

The need to understand the climate system better has become urgent in view of the potential for inadvertent climate modification by our industrial society. Gases and particulates are released to the atmosphere and affect climate both locally, regionally and, perhaps globally.

It has long been recognised that the poleward heat transport and heat storage by the ocean have a moderating effect on the earth's climate. Due to its capacity of storing heat and carbon dioxide (CO_2), the ocean may buffer the anthropogenic additional greenhouse effect (e.g. Bryan and Spelman, 1985). As the present North Atlantic ocean circulation leads to large-scale meridional heat transport to high northern latitudes and to deep water formation and ventilation which is suggested to provide a controlling effect on variations in atmospheric CO_2 levels , a reorganisation of ocean circulation would promote large climate effects.

Recently, there have been numerous observations of low-frequency variability in the air-sea-ice climate system. Interdecadal fluctuations have been observed in the global surface air temperatures (Ghil and Vautard, 1991). Multidecadal wet and dry periods observed in the Sahel region of West Africa (Nicholson, 1986) have been found to be strongly associated with the multidecadal variations of intense hurricane activity along the United States Atlantic and Carribbean coastlines (Gray, 1990). Krishnamurti et al. (1986) observed a decadal time scale pressure oscillation in the global sea level pressure. Decadal fluctuations have been found in the sea-ice coverage in the Barents sea and on the Labrador shelf (Mysak and Manak, 1989; Ikeda, 1990). The time scale associated with such variability suggests that its source lies within the ocean.

Temporal variability has been observed in the properties of the North Atlantic waters as well. Walsh and Johnson (1979) found that a buildup of sea-ice occured in the Arctic during the late 1960's and 1970's. Lazier (1980) observed a decrease in the upper-ocean ($0 - 200m$) salinity in the central Labrador Sea, at Ocean Weather Station (OWS) Bravo during the 1960's and 1970's. Brewer et al. (1983) and Swift (1984) documented a freshening and cooling of the deep waters of the North Atlantic between 1972 and 1982. Lazier (1988) presents evidence that the temperature and salinity changes in the Denmark Strait overflow water in the Labrador Sea underwent a series of sign reversals in the period 1962 – 1986. In a study of Greenland ice core records Hibler and Johnsen (1979) found the strongest spectral peak to occur at a period of about 20 years with a statistically significant amplitude. A review of temporal variability in the properties of the ocean can be found in Levitus (1989).

The reasons behind these climatic changes are not yet clear but some of them coincide with known changes in the salinity of the sub-polar gyre. The timing of the temperature decreases in 1968 and 1981 (Lazier, 1988), for example, corresponds with the movement of fresher than normal water around the North Atlantic and European Arctic during the past two decades, in the surface intermediate layers. This low salinity water, described by Levitus (1989) as one of the most persistent and extreme variations in ocean climate yet observed this century, was first documented by Dickson et al. (1975). The "Great Salinity Anomaly" (GSA), as it is known, manifested itself as a widespread freshening of the upper layer of the sub-polar gyre waters during the period 1968 – 1982 (Dickson et al., 1988). The deep water in both the Norwegian and Labrador Seas became significantly cooler, fresher and less oxygenated (Brewer et al., 1983). Dickson et al. (1988) describe the GSA as largely

an advective phenomenon.

The GSA appears to have played a major role in the formation of large sea-ice anomalies in the Greenland Sea (Malmberg, 1969; Vinje, 1970) and then later on in the Labrador Sea (Mysak and Manak, 1989). Mysak and Manak (1989) also noted that coincident with the passage of the GSA from the Greenland Sea into the Labrador Sea there was a shift of areal sea-ice extent anomalies from one region to the other. Dickson et al. (1988) have indicated that the last instance of a cold anomaly of the magnitude of the GSA in the subarctic gyre was in the early 1900's. At minimum there appears to have been a large scale redistribution of heat and salt in the North Atlantic ocean (Levitus, 1989). Mysak et al. (1990), propose that the GSA may be a manifestation of an interdecadal signal which links various high latitude processes in the Atmosphere-Hydrosphere-Cryosphere part of the climate system. Associated with the GSA was a suppression of convection and hence deep water formation in different parts of the northwest Atlantic (Malmberg, 1969; Lazier, 1980).

Turning on and off of deep water production in the northern Atlantic, would be expected to produce a regional climate change (Broecker et al., 1985). Paleoclimatic data indicates that after the last glacial maximum the North Atlantic deep water (NADW) circulation underwent dramatic fluctuations on a time scale of $\leq$ 500 years (Boyle and Keigwin, 1987; Street-Perrot and Perrot, 1990). One of the ebbs of the NADW coincided with the Younger Dryas cooling event observed on the European continent, in Greenland and, in the high latitude surface waters of the North Atlantic ocean (Broecker et al., 1985; Boyle and Keigwin, 1987). Ruddiman and McIntyre (1981) show that the extent and orientation of the sub-polar gyre underwent oscillatory changes during this period. Boyle and Keig-

win (1982, 1987) found a shift from stronger to weaker NADW formation coincident with the Younger Dryas period. This event was one of the shortest well-documented extreme climate reversals occuring over a period of 1000 – 2000 years (Boyle and Keigwin, 1987). Broecker et al. (1988) proposed that the sudden injection of large volumes of melt-water into the North Atlantic, just south of the Labrador Sea, was responsible for the shutting off of deep-water production during the Younger Dryas period. Freshening tends to stabilize the water column, thereby inhibiting deep convection and reducing the compensating northward transport of heat across the equator by the thermohaline circulation (Rooth, 1982).

The thermohaline circulation is defined as the part of the ocean circulation that is driven by fluxes of heat and salt through the ocean's surface. The large scale thermohaline circulation, commonly thought to manifest itself in the meridional overturning i.e., the zonally integrated mass transport in the latitude-depth plane, is an important mechanism for the meridional transport of heat and salt (e.g., Bryan, 1962; Hall and Bryden, 1982). On the global scale, the thermohaline circulation is a large scale phenomenon linking all the world oceans (Gordon, 1986). Support for the concept that the various ocean basins are communicating via a thermohaline circulation was found in the numerical models of Cox (1989) and Maier-Reimer and Mikolajewicz (1989). Changes in this circulation, and hence its poleward heat transport, would have a significant impact on global climate.

The present-day world ocean is such that deep water forms primarily in the North Atlantic, with rates estimated between 14Sv (Warren, 1981) and 20Sv (Broecker, 1979), while the Pacific ocean exhibits mainly upwelling. Warm salty water spreads into the northern North Atlantic, where it is cooled primarily by evaporation as a consequence of

its anomalously high temperature relative to the atmosphere (Warren, 1983). This in turn maintains a relatively high salinity and density despite an abundance of precipitation. The cooled salty water sinks to the deep ocean, marking the formation of the North Atlantic Deep Water (NADW) (Warren, 1981; Killworth, 1983). The Greenland Sea has long been known to be a major site of deep water formation (Killworth, 1979; Warren, 1981); Rudels et al. (1989) observed deep convection in this region. The other site of deep water formation in the North Atlantic is the Labrador Sea (Lazier, 1973; Clarke and Gascard, 1982). An review of deep ocean circulation can be found in Weaver and Hughes (1992).

The NADW spreads throughout most of the Atlantic, mixing with the deeper Antarctic Bottom Water (AABW) on its way southward, and is exported to the Indian and Pacific oceans via the Antarctic Circumpolar Current (ACC) and deep western boundary currents (Gordon, 1986). The trajectories of the AABW and NADW can be traced by their temperature and salinity (TS) characteristics throughout the world ocean (Mantyla and Reid, 1983). The NADW joins the rapidly moving deep ACC, south of 30°S, which blends it with new deep water generated along the edge of the Antarctica and also with old deep water recirculated back into Antarctic from the deep Pacific and Indian Oceans (Broecker, 1991). The NADW water mass influences most of the global ocean (Reid and Lynn, 1971).

The NADW returns to the surface in the northern Indian and Pacific oceans. In reality this upwelling is widely spread with a large amount taking place in the Antarctic (Broecker, 1991). Gordon (1986) proposed that the return flow for the compensating upper layer water towards the northern North Atlantic required to feed the NADW production is accomplished within the ocean's warm thermocline water. This implies that the main

thermoclines of the world ocean are linked as they participate in a thermohaline-driven global scale circulation associated with the NADW production.

Gordon's proposed *warm* water route, *the global conveyor*, is as follows: The upwelled water flows from the Pacific to the Indian ocean through the Indonesian Archipeleago, is advected across the Indian ocean, transferred southward in the Mozambique Channel and enters the South Atlantic by a branch of the Agulhas that does not complete the retroflection pattern, and then northward within the subtropical gyre of the South Atlantic and, finally as cross-equatorial flow into the western North Atlantic where deep water formation occurs. A slight modification to Gordon's conveyor circulation was recently proposed by Hughes et al. (1992); they hypothesized that some of the waters from the equatorial Pacific circulate around the Indian ocean and are then transported poleward in the Leeuwin Current, returning to the south Atlantic via the eastward flowing ACC i.e, Pacific to Atlantic transport of sub-Arctic water within the Drake Passage (the *cold* water route). Based on ocean chemistry analysis, Broecker (1991) suggested that the main return path is the cold water route.

The process of NADW formation is self-perpetuating in that as the surface layer water sinks and is exported southward within the deep layer, more upper layer water is drawn into the northern North Atlantic. This in turn drives the high evaporation rates continuing the NADW formation process (Gordon, 1986).

Based on a diverse collection of paleoclimatic data, Broecker et al. (1985) hypothesized that during glacial times the deep ocean circulation was in a mode of operation different from today's. Siegenthaler and Wenk (1984) suggested that changes of the ocean surface

circulation were responsible for rapid atmospheric CO_2 variations during, and at the end, of the last ice age. In the context of ocean circulation and climate change, one of the main lessons to be learned from paleoclimatic records is the possibility of very rapid climate changes, like the onset and cessation of the Younger Dryas period (Broecker, (1987))

Recently, Ocean General Circulation Models (OGCMs) have been used to study the properties of the thermohaline circulation with particular emphasis on its stability and variability.

In attempting to explain the observed oceanic variability it is common to seek variability in the ocean's external forcing e.g., solar heating, winds, evaporation minus precipitation, attractive force of heavenly bodies and ice formation. Recent numerical studies have uncovered a multitude of self-contained dynamical systems that undergo variations on a wide range of time scales, without the aid of any varying external influences (e.g., Lorenz, 1990). James and James (1989) observed internal variability at the decadal time scale in a fully non-linear, primitive equation, atmospheric general circulation model. Recently, a number of investigators have demonstrated the existence of decadal and interdecadal internal variability of the thermohaline circulation, under steady forcing, in different ocean circulation models e.g., Weaver and Sarachik (1991*a*); Weaver et al. (1991). Numerous studies have also recently demonstrated the possible existence of multiple equilibria in the thermohaline circulation, a concept advanced originally by Chamberlin (1906) and Stommel (1961). In most of these studies, transition from one model equilibrium state to another was attained either by adding salinity anomalies to the system e.g., Bryan (1986*a*,*b*), Marotzke et al. (1988), Marotzke (1989), Marotzke and Willebrand (1991), or upon a switch in surface boundary

condition type i.e., from Newtonian *restoring* conditions to *mixed* boundary conditions e.g., Weaver and Sarachik (1991*a*,*b*), Marotzke and Willebrand (1991), Weaver et al. (1991). Marotzke (1991) shows how some of the results concerning the stability of the thermohaline circulation, under mixed boundary conditions, are sensitive to the convective scheme used in the models. Stocker and Wright (1991) show how changes in the net atmospheric Atlantic-to-Pacific fresh water flux could induce hysteresis behaviour in the thermohaline circulation.

Important for occurence of variability of the thermohaline circulation in OGCMs, is the use of *mixed surface boundary conditions* i.e., a Newtonian restoring condition on surface temperature together with a specified flux condition on surface salinity. There is justification for use of these boundary conditions in that sea surface temperature (SST) is strongly constrained by oceanic heat flux, which in turn depends upon air-sea temperature differences, whereas sea surface salinity (SSS) has negligible direct effects on evaporation, precipitation and, continental runoff which provide its surface forcing. Thus, in ocean modelling studies, an appropriate boundary condition for surface salinity is a virtual salt flux which is independent of surface salinity though it may depend on surface temperature (Bryan, 1986*a*). A detailed discussion of the implications of using restoring and mixed boundary conditions can be found in Weaver and Sarachik (1991*a*). A review of phenomena related to the use of mixed boundary conditions is given by Welander (1986).

One of two different approaches is usually taken for obtaining salt fluxes for use in OGCMs. One is to derive the fluxes from observational data sets of evaporation and precipitation. Moore and Reason (1992) discuss some of the ways in which this can be done.

This procedure is usually avoided due to lack of sufficient observational data. The other, more common approach is to spin up the model to steady state using restoring boundary conditions on both temperature and salinity, diagnose the salinity flux required to maintain this steady state, and then further integrate using this diagnosed surface salinity flux as a specified flux boundary condition e.g., Bryan (1986*a*,*b*); Marotzke (1989); Stocker and Wright (1991); Wright and Stocker (1991); Marotzke and Willebrand (1991); Weaver and Sarachik (1991*a*); Weaver et al. (1991). The rationale behind this approach is that the resultant freshwater flux field, in theory, yields SST fields that compare reasonably well with observed climatological data e.g., Myers and Weaver (1992).

All of the above studies, except Moore and Reason (1992), have been confined to zonally averaged models or highly idealised models consisting of either a single flat bottomed rectangular basin or two such basins connected at one end.

Crucial to the occurence of internal variability of the thermohaline circulation, under mixed boundary conditions, is the structure of the evaporation minus precipitation ($E - P$) forcing fields and the relative importance of fresh water flux versus thermal forcing (Weaver et al., 1992). Weaver et al. (1991) suggested that in the presence of a sufficiently strong local maximum, at high latitudes, in the $E - P$ forcing fields, self-sustained oscillations of the ocean circulation may be excited. The annual $E - P$ fields of Schmitt et al. (1989) exhibit two local maxima at high latitudes: One maximum is located off the southwestern coast of Greenland; and, the other stretches eastward from the east coast of Greenland, near 65° latitude. These type of features may be expected to induce internal variability in the thermohaline circulation (e.g., Weaver et al., 1992).

An important part of the hydrological cycle within the NADW formation region is the southward flux of fresh water from the Arctic into the upper layers: The addition of Pacific water to the Arctic sea via the shallow Bering Straits and excess fresh water primarily due to continental runoff introduced directly into the Arctic Sea result in a net southward flux of low-salinity water into the open North Atlantic Ocean (Gordon and Piola, 1983). Baumgartner and Reichel (1975) give a total annual accumulation of fresh water into the Arctic Sea north of 65° north as 0.13Sv ($1Sv=10^6 m^3 s^{-1}$). The total Arctic accumulation of fresh water and Bering Straits input must ultimately spread into the open Atlantic south of 65° north. This is accomplished by the shallow southward flowing East Greenland Current into the western half of the the North Atlantic (Gordon and Piola, 1983; Aagaard and Carmack, 1989). Integration of the Arctic water is assumed to occur in the latitude band 40° – 65° north (Gordon and Piola, 1983). Through its export of fresh water the Arctic Ocean ultimately may control the ocean ventillation which occurs in the Greenland and Iceland Seas.

Aagaard and Carmack (1989) show that the present small salinity and density stratification in the convective gyres in the Greenland and Iceland Seas is likely maintained in part by local precipitation excess and in part by a lateral influx of fresh water from the East Greenland Current. They suggest that in the extreme case of a relatively large influx into the interior the convection would cease and the convective gyres would be capped by a fresh water lid in what would be a small-scale, present-day, analog of the halocline catastrophe proposed for past deglaciations (e.g., Broecker et al., 1985). Aagaard and Carmack (1989) suggest that the GSA, which Dickson et al. (1988) hypothesized as having originated north

of Iceland, can be accounted for by a moderate outflow from the Arctic Ocean. It is, therefore, evident that the Arctic fresh water flux may play an important role in the NADW formation and climate.

The objective of this study is to test if internal variability of the simulated thermohaline circulation is robust under steady, non-zonal, forcing and realistic geometry. The surface boundary conditions are derived from the observed climatological data sets of Levitus (1982), Hellerman and Rosenstein (1983) and, Schmitt et al. (1989). Despite the uncertainties inherent in these fields they are among the most reliable estimates of air-sea parameters available. Arctic freshwater transport into the northern North Atlantic is taken into account. All forcing functions are constant in time and the effects of sea ice are not considered.

The outline of this thesis is as follows: A broad overview of the model is given in chapter 2. In chapter 3 a description of the model domain and the surface forcing fields are presented. Chapter 4 covers a description of the experiments and an extensive discussion of the results. The summary and conclusions are presented in chapter 5.

2 The numerical model

The ocean general circulation model (OGCM) used in this study is the Cox (1984) version of the Bryan-Cox primitive equation model based on the computational method of Bryan (1969). A broad overview of the model is presented.

2.1 The model equations

The primitive equations for the ocean are derived from the Navier-Stokes equations using some basic assumptions. First, density is treated as constant except where it is coupled to gravity in the bouyancy term of the vertical momentum equations i.e., the Boussinessq approximation. Thus the ocean is considered incompressible and local density variations are assumed to be small perturbations of the basic state density field. Second, the local acceleration and other terms of the same order are neglected in the equation for vertical motion, reducing it to the hydrostatic approximation. Vertical motion thus changes from a prognostic to a diagnostic variable through continuity. Third, only the large-scale motion is treated explicitly, and stresses exerted by sub-grid processes are parameterized as enhanced molecular mixing, in terms of horizontal and vertical viscosities and diffusivities, using a *turbulent viscosity* hypothesis. Temperature and salinity are evaluated using conservation equations, again utilizing a turbulent closure scheme. The equations are linked by an equation of state.

The above approximations reduce the Navier-Stokes system of equations to the *primitive equations*. For model computations the equations are formulated in spherical coordinates with λ, ϕ, z representing longitude, latitude, and depth. Seven variables specify the condi-

tion of the ocean: Three velocity components (u, v, w), potential temperature (T), salinity (S), pressure (p) and density (ρ). The model equations are as follows:

The horizontal momentum equations are given by,

$$\frac{\partial u}{\partial t} + \mathcal{L}(u) - fv = -\frac{1}{\rho_0 a \cos\phi}\frac{\partial p}{\partial \lambda} + A_{MV}\frac{\partial^2 u}{\partial z^2} + F^{\lambda} \tag{1}$$

$$\frac{\partial v}{\partial t} + \mathcal{L}(v) + fu = -\frac{1}{\rho_0 a}\frac{\partial p}{\partial \phi} + A_{MV}\frac{\partial^2 v}{\partial z^2} + F^{\phi} \tag{2}$$

where, $f = 2\Omega \sin\phi$ is the Coriolis parameter, A_{MV} is the vertical eddy viscosity coefficient, F^{λ} and F^{ϕ} are the meridional and zonal stresses, respectively,

$$F^{\lambda} = A_{MH}\{\nabla^2 u + \frac{(1-\tan^2\phi)u}{a^2} - \frac{2\sin\phi}{a^2\cos^2\phi}\frac{\partial v}{\partial \lambda}\}$$

$$F^{\phi} = A_{MH}\{\nabla^2 v + \frac{(1-\tan^2\phi)v}{a^2} + \frac{2\sin\phi}{a^2\cos^2\phi}\frac{\partial u}{\partial \lambda}\}$$

where, A_{MH} is the horizontal eddy viscosity coefficient. $\mathcal{L}$ denotes the advection such that,

$$\mathcal{L}(\sigma) = \frac{1}{a\cos\phi}\frac{\partial}{\partial \lambda}(u\sigma) + \frac{1}{a\cos\phi}\frac{\partial}{\partial \phi}(v\sigma\cos\phi) + \frac{\partial}{\partial z}(w\sigma)$$

For the coarse resolution model used in this study the Rossby number is very small thus the momentum equations are linearized i.e., $\mathcal{L}$ is set equal to zero. The horizontal Laplacian, ∇^2, is given by,

$$\nabla^2(\sigma) = \frac{1}{a^2\cos^2\phi}\frac{\partial^2\sigma}{\partial\lambda^2} + \frac{1}{a^2\cos\phi}\frac{\partial}{\partial\phi}(\frac{\partial\sigma}{\partial\phi}\cos\phi)$$

The vertical momentum equation i.e., the hydrostatic approximation is given by,

$$\frac{\partial p}{\partial z} = -\rho g \tag{3}$$

The mass continuity equation reads,

$$\frac{1}{a\cos\phi}\frac{\partial u}{\partial \lambda} + \frac{1}{a\cos\phi}\frac{\partial}{\partial \phi}(v\cos\phi) + \frac{\partial w}{\partial z} = 0 \tag{4}$$

The conservation equations for potential temperature and salt are given by,

$$\frac{\partial T}{\partial t} + \mathcal{L}(T) = A_{TV}\frac{\partial^2 T}{\partial z^2} + A_{TH}\nabla^2 T + C_A(T) \tag{5}$$

$$\frac{\partial S}{\partial t} + \mathcal{L}(S) = A_{TV}\frac{\partial^2 S}{\partial z^2} + A_{TH}\nabla^2 S + C_A(S) \tag{6}$$

where A_{TH} and A_{TV} are the horizontal and vertical eddy diffusivities, respectively. The term C_A schematically represents convective adjustment: the effects of stratification are taken into account using an implicit vertical diffusion scheme (IVD) such that the vertical diffusivity (A_{TV}) is finite ($1.0 cm^2 s^{-1}$) for the stable case and infinite ($10^4 cm^2 s^{-1}$) for the unstable case.

The nonlinear equation of state for sea water is given by,

$$\rho = \rho(T, p, S) \tag{7}$$

For model computations, the polynomial approximation of Bryan and Cox (1972) is used.

2.2 Boundary conditions

The bottom and the lateral walls are assumed insulating and impermeable i.e., a no flux condition is imposed on both heat and salt. A *no slip* condition ($u = v = 0$) is applied at the lateral walls. A symmetry condition holds at the equator. At the bottom boundary a *free slip* condition ($\frac{\partial u}{\partial z} = \frac{\partial v}{\partial z} = 0$) is imposed, with $w = 0$ at $z = -H$; H being the depth of the ocean (assumed flat).

Surface boundary conditions require some additional considerations. In particular, air-sea interaction processes must be parameterized. At the surface, vertical displacements of the ocean are not allowed i.e., $w = 0$ at $z = 0$. This constraint, the *rigid-lid* approximation, has the effect of excluding kinematic effects of surface variations and filtering out the external gravity waves which, otherwise, would limit the time step of the integration (Bryan, 1969).

Coupling of the ocean to the "atmosphere" is accomplished through surface wind stresses (τ^{λ}, τ^{ϕ}). For ocean modelling the surface wind stresses used are normally obtained either from climatological data sets derived from observations (e.g., Moore and Reason, 1992) or by using a simple analytic function reflecting the major features of the observed wind distribution (e.g., F. Bryan, 1987; Weaver and Sarachik, 1990; Weaver and Sarachik, 1991*a*). In all the experiments to be described the model was forced at the surface with the annual mean wind stresses of Hellerman and Rosenstein (1983).

Further coupling to the "atmosphere" is achieved by imposing boundary conditions on both temperature and salinity at the ocean surface. Two different types of boundary conditions were applied to the ocean model surface temperature and salinity fields: *restoring*

and *mixed* boundary conditions.

In the control experiment, both temperature (T) and salinity (S) were relaxed to their observed annual mean surface values as given by Levitus (1982) such that

$$Q^T(\lambda,\phi) = -\rho_0\, C_p \frac{\Delta z_1}{\tau_R}(T_1(\lambda,\phi) - T^*(\lambda,\phi)) \tag{8}$$

$$Q^S(\lambda,\phi) = -\rho_0 \frac{\Delta z_1}{\tau_R}(S_1(\lambda,\phi) - S^*(\lambda,\phi)) \tag{9}$$

where Q^T and Q^S are the fluxes of heat and salt into the ocean, $\Delta z_1 = 50m$ the thickness of the uppermost model grid box, $\rho_0 = 1000 kgm^{-3}$ a reference density, $C_p = 4000 Jkg^{-1}K^{-1}$ the specific heat at constant pressure, $\tau_R = 50$ days the damping constant, assumed the same for both temperature and salinity, T_1 and S_1 the temperature and salinty of the uppermost ocean grid box, and T^* and S^* the reference temperature and salinity, respectively. The latter are taken as the annually averaged sea surface temperatures (SST) and salinities (SSS) obtained from the climatological atlas of Levitus (1982).

Restoring the sea surface temperature to prescribed values has its justification with the work of Haney (1971); a strong feedback exists between sea surface temperature and its atmospheric forcing. Surface salinity, on the other hand, has little or no direct effects on evaporation and precipitation which provide its surface forcing. A prescribed flux law, where the net fresh water input is specified in terms of evaporation minus precipitation ($E - P$), is much more appropriate for the surface salinity. In the case of the experiments with mixed boundary conditions a specified flux boundary condition was imposed on the sea surface salinity while the Newtonian restoring boundary condition on temperature was

retained.

Surface salinity in the real ocean is modified by a fresh water flux which, locally, is given by the total rainfall, evaporation and continental runoff. In the presence of the rigid-lid constraint, however, it is not possible to force the ocean model directly with a fresh water flux. Normally a salinity flux is constructed such that the net global salinity flux vanishes (e.g Moore and Reason, 1992). In this work a fixed salt flux was constructed from the $E - P$ climatological data set of Schmitt et al. (1989) using a reference salinity $S_o = 35.12$ practical salinity units (psu), the basin mean salinity for the North Atlantic as calculated from Levitus (1982) climatological data, using a formula of the form,

$$Q^S(\lambda,\phi) = -\rho_o \frac{S_o}{Syr}(P(\lambda,\phi) - E(\lambda,\phi)) \tag{10}$$

where Syr is the number of seconds in a year.

2.3 Numerics and model parameters.

2.3.1 Numerics

The model equations are evaluated using a second order conserving differencing scheme (Bryan, 1969; Semtner, 1974; Cox, 1984) and are formulated on the B-Grid, following Arakawa and Lamb (1977). The differencing scheme is centred with respect to time for the pressure term and the non-linear terms e.g., advection, while forward time stepping is applied to the viscous term. A one time-step lag on the diffusion terms ensures numerical stability and periodic substitution of a backward Euler time step for the leapfrog differencing circumvents the splitting of solutions. A serious constraint on the time step of integration

is overcome by a semi-implicit treatment of the Coriolis term. This allows for a time step longer than the inertial period, if all other stability criteria are satisfied.

The Arakawa B-Grid is an energy conserving scheme. On this grid, the tracers (e.g temperature and salinity) and the barotropic streamfunction are evaluated on one grid while the horizontal velocities are computed on another mesh displaced half a grid interval both zonally and meridionally. Vertical velocity is evaluated, separately for both grids, at levels intermediate between the main grids. Lateral boundaries are placed on velocity points, giving the best representation of no-slip boundary conditions. Pressure, density and vertical velocity are solved for diagnostically from the hydrostatic equation, the equation of state and the continuity equations, respectively. The horizontal components of velocity; the temperature; and, the salinity are computed from the horizontal momentum and the conservation equations, respectively. The horizontal velocity is decomposed into barotropic and baroclinic components in order to eliminate the part of the pressure gradient which depends on the surface pressure.

2.3.2 Model parameters

In spatial centred difference numerical schemes the choice of model parameters is based on numerical stability considerations. The model closure parameters, the eddy viscosities and diffusivities, are constrained to satisfy the grid Reynolds and Peclet criteria, respectively. However, the condition involving the horizontal diffusivity need not be satisfied since strong geostrophic coupling between the velocity and the density fields, at most latitudes, is sufficient to suppress the spurious numerical modes (Bryan et al., 1975). Further, the

magnitudes of A_{TH} and A_{MH} should be small enough not to obscure heat and salt transport by currents yet A_{MH} should be chosen large enough to resolve the Munk layer, on the western boundary layer, due to the no-slip boundary condition. Lastly, the length of the time step of integration is constrained to satisfy the Courant-Frederichs-Levy (CFL) criterion. A detailed discussion of these constraints can be found in Bryan et al. (1975).

In this study the vertical and horizontal eddy viscosities (A_{MV}, A_{MH}) and diffusivities (A_{TV}, A_{TH}) were held constant over the whole domain: $A_{MV} = 10.0$, $A_{TV} = 1.0$, $A_{MH} = 1.5\times10^{9}$, $A_{TH} = 1.0\times10^{7}$. All units are in cm^2s^{-1}

In order to accelerate the convergence of the numerical model the split time-stepping techniques, following Bryan (1984), were employed in weak asynchronous integrations: a 2-hour time step was used for the barotropic and baroclinic velocity equations while the tracer equations for temperature and salinity were integrated with time steps ranging from 0.5 to 2 days depending on the the experiment. Asynchronous time stepping in the vertical was not applied.

In this study, all the experiments were started from resting homogeneous states with uniform temperature of 5° C. The initial salinity for the control run was 33.0 psu while that for the rest of the experiments was taken as 35.12 psu, the latter value being motivated from the basin mean for the North Atlantic as calculated from Levitus (1982) climatological data.

3 Model domain and forcing fields

In this section a description of the model domain is given. A brief discussion of the forcing fields together with some of the uncertainties inherent in these fields is carried out as well.

3.1 Model domain

The model domain constitutes a flat-bottomed northern hemisphere basin with realistic geometry (see figure 1), spanning $0^o - 75^o$ latitude and $6^o - 81^o$ West, with vertical depth 4020 m everywhere. The horizontal resolution is uniform at 3^o latitude by 3^o longitude. There are 20 levels of increasing depth in the vertical as shown in table 1.

3.2 The forcing fields

In all the model runs in this study the spin-ups were started from resting, homogeneous states. Coupling of the ocean with the "atmosphere" was achieved by imposing boundary conditions at the ocean surface.

The temperature and salinity fields were obtained from the Levitus (1982) climatological atlas of the world ocean. The Levitus atlas represents an objectively analysed synthesis of all the temperature, salinity and, oxygen data available from the National Oceanographic Data Center (NODC), Washington D.C. on a 1^o-resolution. Figures $1a - b$ illustrate the temperature and salinity fields over the North Atlantic on $1^o \times 1^o$ grids.

Uncertainties exist in the representativeness of this data in that the Levitus atlas presents smoothed analyses of historical averages based in certain areas on relatively few observations with some sampling biases. Despite the uncertainties inherent in these fields

Level	Depth of tracer level	Gridbox thickness	Depth of bottom of gridbox
1	25	50	50
2	75	50	100
3	125	50	150
4	180	60	210
5	250	80	290
6	340	110	390
7	450	120	510
8	585	150	660
9	750	180	840
10	950	220	1060
11	1190	260	1320
12	1470	300	1620
13	1770	300	1920
14	2070	300	2220
15	2370	300	2520
16	2670	300	2820
17	2970	300	3120
18	3270	300	3420
19	3570	300	3720
20	3870	300	4020

Table 1: Vertical discretization used in the model. Units are metres.

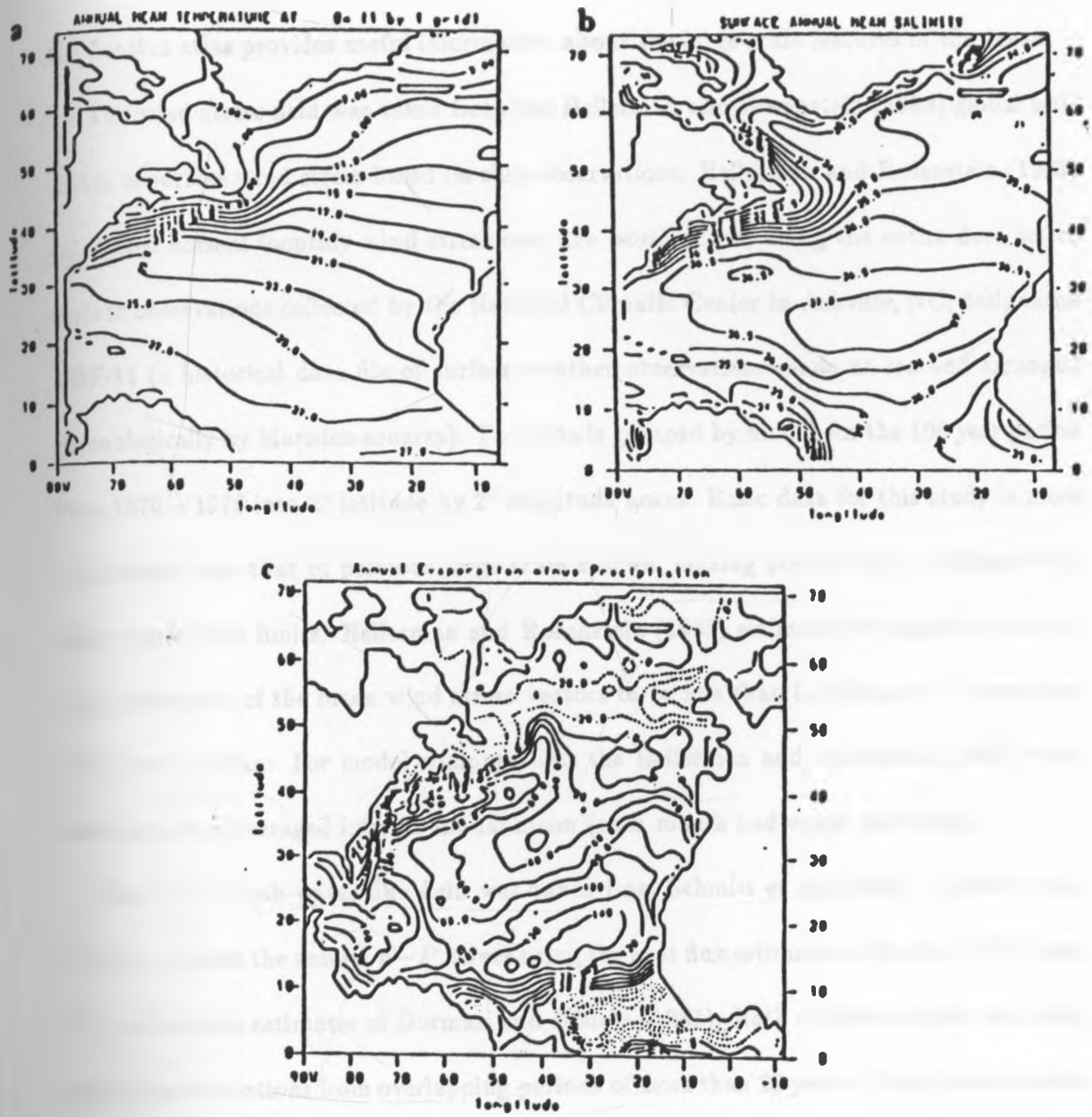

Figure 1: a) Levitus (1982) annual mean potential temperature (^0C) at the sea surface, b) Levitus (1982) mean annual salinity (psu) at the sea surface, and c) Schmitt et al. (1989) annual Evaporation minus Precipitation ($E - P$) fluxes in $cmyear^{-1}$).

the Levitus atlas provides useful information about the large-scale features of the ocean.

The wind stress field was taken from the Hellerman and Rosenstein (1983) global estimates of surface wind stress based on ship observations. Hellerman and Rosenstein (1983) calculated normal monthly wind stress over the world ocean, using the entire data set of surface observations collected by the National Climatic Center in Ashville, NC, designated TDF-11 (a historical data file of surface weather observations made at sea and arranged chronologically by Marsden squares). The data is grouped by month for the 106 year period from 1870 – 1976 into 2° latitude by 2° longitude boxes. Basic data for this study is more voluminous than that of previous large-scale studies, making possible data analyses with higher confidence limits. Hellerman and Rosenstein (1983) estimate the standard error in each component of the mean wind stress vectors to be less than 0.1 $dynescm^{-2}$ over most of the world ocean. For model computations the Hellerman and Rosenstein (1983) wind stress data was averaged into an annual mean (each month had equal weighting).

The $E - P$ fresh water flux field was taken from Schmitt et al. (1989). Schmitt et al. (1989) calculated the annual $E-P$ values using the heat flux estimates of Bunker (1976) and, the precipitation estimates of Dorman and Bourke (1981). Both of these studies are based upon ship observations from overlapping periods of more than 20 years. Uncertainties in the accuracy of each dataset are thought to be about 20% in well-sampled low-latitude regions. Data sparse high-latitude areas have larger uncertainties. Thus, the error in the derived quantities may be substantial in certain areas. These maps of $E - P$ have greater spatial and temporal resolution than any previous estimates e.g., Baumgartner and Reichel (1975). Figure 1c illustrates the Schmitt et al. (1989) fields on a 1°-resolution.

For model computations the data was rearranged onto 3° x 3° grid meshes such that the wind stress vectors were carried on one set of grid points, and the $E - P$, temperature and salinity values were carried on another set displaced 1.5° interval, both meridionally and zonally, from the wind stress vectors. Due to lack of data, the $E - P$ data at the northernmost grid points i.e., along 70.5° and 73.5° latitude, was set equal to that at 69.5° latitude. The lateral walls were placed on the wind stress points in accordance with the Arakawa B-grid formulation. Further, a simple zonal interpolation scheme was applied across the islands to eliminate landmasses from the domain of interest. The final model forcing fields are as illustrated in figure 2.

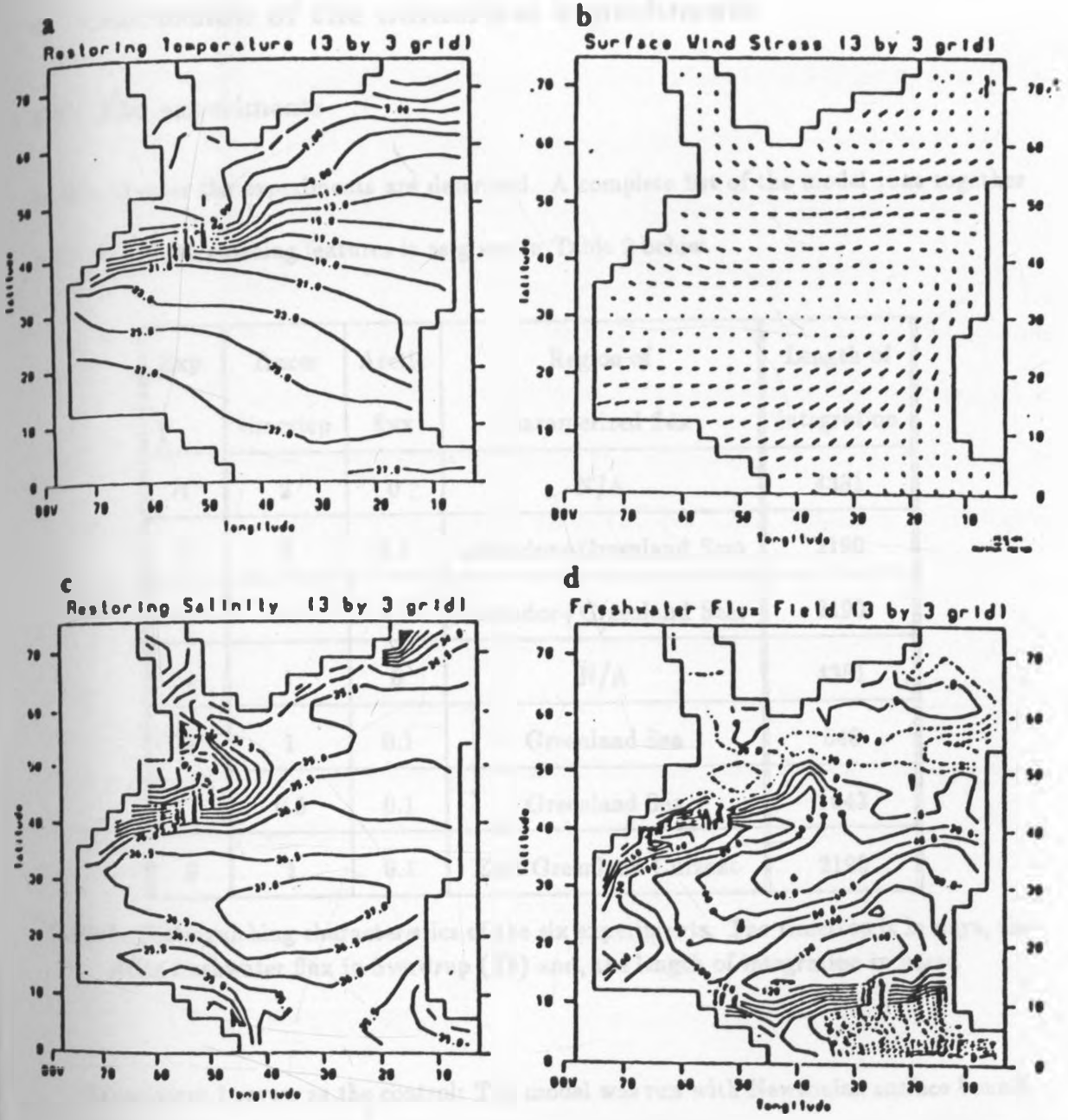

Figure 2: The model surface forcing fields on a $3° \times 3°$ horizontal resolution grid; a) temperature (^0C) derived from Levitus (1982), b) salinity (psu) derived from Levitus (1982), c) wind stress ($dynescm^{-2}$) derived from Hellerman and Rosenstein (1983) and d) fresh water fluxes ($cm/year$) derived from Schmitt et al. (1989). The contour interval in a) is 2 $°C$, in c) 0.5 psu, in d) 20 cms^{-1}. The maximum wind stress vector is 1.5 $dynescm^{-2}$.

4 Discussion of the numerical experiments

4.1 The experiments

In this chapter the experiments are described. A complete list of the model runs together with their distinguishing features is as given in Table 2 below.

Exp.	Tracer timestep	Arctic flux	Region of paramerized flux	Length of integration
1	2	0	N/A	4381
2	1	0.1	Labrador+Greenland Seas	2190
3	0.5	0.2	Labrador+Greenland Seas	2190
4	1	0	N/A	4381
5	1	0.1	Greenland Sea	548
	0.5	0.1	Greenland Sea	1643
6	1	0.1	East Greenland Current	2190

Table 2: Distinguishing characteristics of the six experiments. The timestep is in days, the Artic freshwater flux in Sverdrup (Sv) and, the length of integration in years.

Experiment 1 serves as the control: The model was run with Newtonian surface boundary conditions on both temperature and salinity. The purpose of this run was to determine the structure of the ocean circulation and output fields under present day surface climatological forcing. These fields were then used for comparison with output from other model runs in order to determine if the $E - P$ forcing fields give good SST and SSS model

structures.

The rest of the experiments were performed under mixed boundary conditions. In experiments 2, 3, 5 and 6 the effect of Arctic fresh water flux into the northern North Atlantic was considered. To parameterize the Arctic freshening, the fresh water flux was distributed evenly in the top 210 m of a specified region depending upon the experiment: In experiments 2 and 3 the flux was added uniformly along the northern boundary i.e., to both the "Labrador" and "Greenland Seas"; in experiment 5, the parameterization was confined to the northernmost grid boxes of the "Greenland Sea" region i.e., no flux was added to the "Labrador Sea"; in experiment 6 the fresh water flux was added only to the top 210 m of the two grid boxes adjacent to "Greenland" i.e., in the "East Greenland Current" region of the "Greenland Sea". To ensure conservation of salt, the net salt flux (surface $E - P$ minus Arctic freshwater flux) was calculated and added as an additional fresh water flux to the top 210 m of the region all across the equatorial boundary. This will be referred to in the text as the *equatorial flux condition.*

4.2 Discussion

4.2.1 The reference solution

In this section a description of the basic features of the circulation for the reference case, Exp. 1, is given with particular emphasis on the nature of the equilibrium solution.

The reference case was started from a resting homogeneous state with a temperature of 5 $^{\circ}C$ and salinity 33.0 *psu*. The model was integrated forward in time, under restoring boundary conditions on both temperature and salinity, for 4381 years of tracer time steps.

The solution at this stage was referred to as the equilibrium solution even though there were some very slight trends in the thermal fields. At this point in the integration the mean surface heat flux was 0.29 Wm^{-2}.

The surface (25 m) temperature and salinity fields for Exp. 1, at equilibrium, are shown in figures $3a - b$. Over most of the interior of the basin the surface values are close to their reference values $T^*(\lambda, \phi)$ and $S^*(\lambda, \phi)$ (cf. figures $1a - b$). This implies that the surface advective and diffusive time scales in the interior of the basin are much longer than the 50 days required for the boundary conditions to restore the surface properties to their reference values. Figures $3c - d$ show the temperature and salinity differences between Exp. 1 and Levitus (1982). The largest temperature differences occur in the Gulf Stream region where Exp. 1 is up to 3.2 $°C$ warmer than Levitus data. This region is characterised by large meridional temperature gradients in Exp. 1 which are rigorously maintained through strong relaxation to Levitus climatology values at the surface. Despite the relatively strong upwelling in the western boundary layer and the very weak upwelling in both the Labrador and the Greenland Seas, horizontal advection warms the surface waters significantly above the reference values in these regions while at the equator strong upwelling cools the local temperatures, particularly in the east. The upwelling along the western boundary layer is spurious and is due to poor representation of lateral mixing in the model (e.g., Veronis, 1975). Toggweiller et al. (1989) suggest the unphysical partitioning of mixing processes into horizontal and vertical components rather than components parallel and perpendicular to surfaces of constant density as a possible cause. Figure $3d$ shows SSS differences between Exp. 1 and Levitus data of up to 1.0 psu in the Gulf Stream, the latter

being fresher than the former in this region.

The surface horizontal velocity field is shown in figure 4*a*. The western boundary current has maximum velocities on the order of 23 cms^{-1}. This is an order of magnitude less than that observed in the Gulf Stream or other western boundary currents. A tight recirculation is located just offshore of the northward boundary current at about 30°N.

The vertical velocity at the base of the surface grid box is shown in figure 4*b*. The strong downwelling at the northeastern boundary, centred near 65°N, is the major site of deep water formation in this solution as will be discussed later.

The surface heat, salt and fresh water fluxes may be computed diagnostically from equations 8, 9 and 10 respectively. The fluxes of heat and fresh water for the equilibrium state of the reference solution are shown in figures 5*a* – *b*. The magnitudes of the fluxes are largest where the surface temperature and salinity deviate most from Levitus climatological values: along the western boundary current, in mid-gyre in the mid-latitudes, in the Greenland Sea and, near the equator. The heat flux (figure 5*a*) is positive (into the ocean) over most of the interior of the basin equatorward of the boundary between the sub-polar and sub-tropical gyres; in the western boundary layer and poleward of this boundary the heat flux is negative. Negative heat fluxes are also observed along the eastern boundary of the domain both in the tropics and the sub-tropics. Despite the idealized nature of the model, the pattern and magnitude of the surface heat flux agrees reasonably well with observations. Surface heat flux estimates of Bunker (1976) for the North Atlantic are shown in figure 6. The largest observed positive heat fluxes are near the equator, and the largest negative heat fluxes are along the western boundary current. Despite the high correlation between the reference

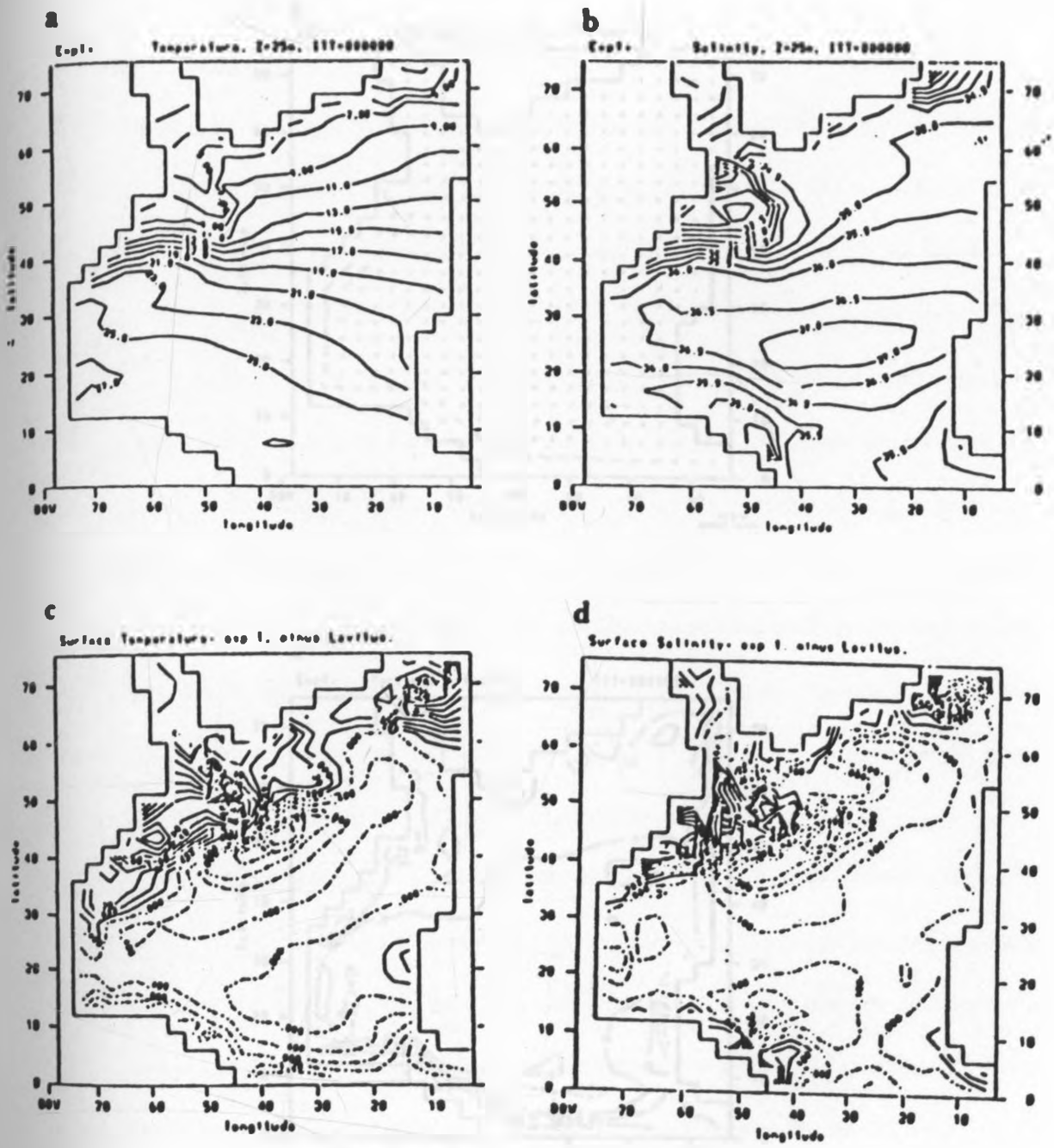

Figure 3: a) Surface temperature (°*C*) and b) surface salinity (*psu*) for the reference solution at equilibrium; c) temperature (°*C*) differences between Exp. 1 and Levitus (1982) (Exp. 1 - $T°$) and d) salinity differences between Exp. 1 and Levitus (1982) (Exp. 1 - $S°$). The contour interval in a) is 2 °*C*, b) 0.5 *psu* c) 0.4 °*C* and d) 0.1 *psu*.

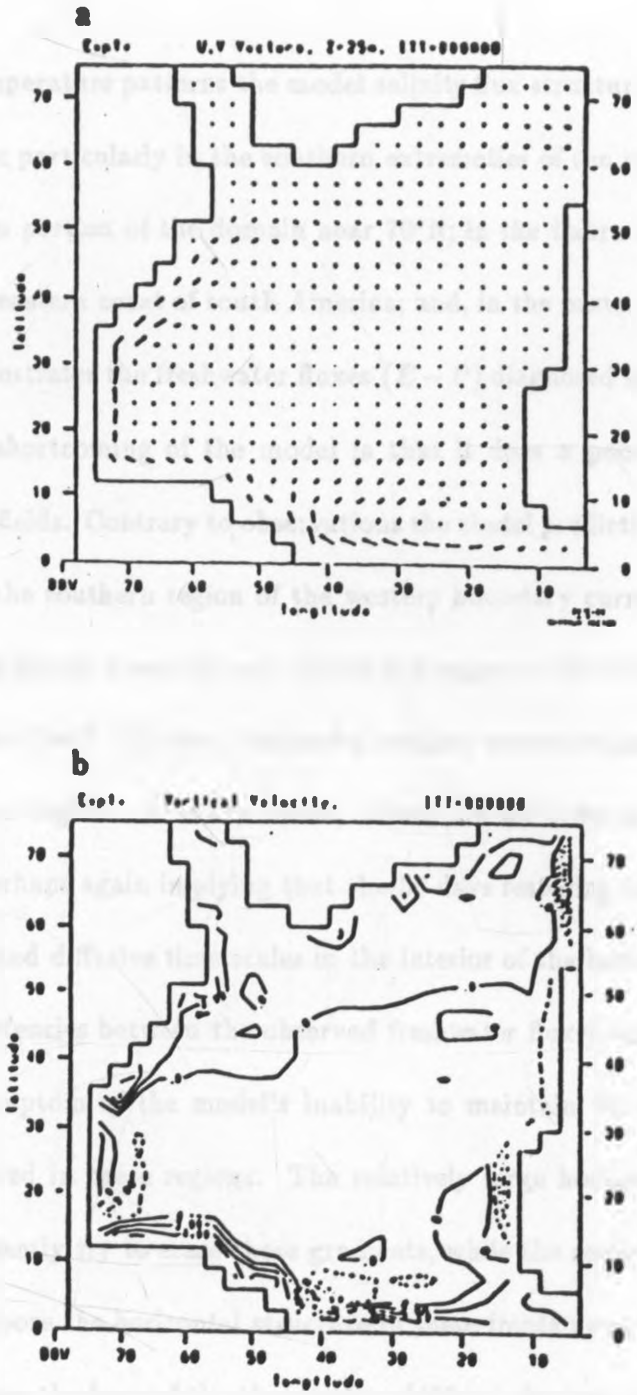

Figure 4: Exp. 1 a) Surface ($z = 25\ m$) horizontal velocity (cms^{-1}) and b) vertical velocity at the base of the surface grid box i.e $z = 50\ m$. The contour interval for the vertical velocity is $2 \times 10^{-4}\ cms^{-1}$. The maximum horizontal velocity vector is $23\ cms^{-1}$.

salinity and temperature patterns the model salinity flux structure (not shown) differs from that of heat flux particularly in the southern extremeties of the western boundary current; the northeastern portion of the domain near 70°N; in the Labrador Sea near 56°N, 48°W; along the northeastern coast of south America; and, in the eastern equatorial region.

Figure 5*b* illustrates the freshwater fluxes ($E - P$) diagnosed from the equilibrium state of Exp. 1. A shortcoming of the model is that it does a poor job of reproducing the observed $E - P$ fields. Contrary to observations the model predicts excess precipitation over evaporation in the southern region of the western boundary current; off the northern and eastern coasts of South America; and, within the region of the local evaporation maximum in the "Greenland Sea". Further, the model predicts excess evaporation over precipitation in the equatorial region. Also the model values are an order of magnitude larger than observations, perhaps again implying that the 50 days restoring time scale is much shorter than advective and diffusive time scales in the interior of the basin.

The inconsistencies between the observed freshwater fluxes and those predicted by the model are a symptom of the model's inability to maintain the large horizontal salinity gradients observed in these regions. The relatively large horizontal eddy diffusivities in the model constantly try to erase these gradients, while the restoring boundary conditions continuously impose the horizontal structure of these fronts upon the model SSS.

At a level near the base of the thermocline (450 m) the temperature and salinity fields (figures 7*a*, *b*) have lost the complicated structure of the surface layers and show distinctive features of the wind driven subtropical gyre. A notable feature of the horizontal velocity field at this level (figure 7*d*) is the change in orientation of the flow at the southern flank

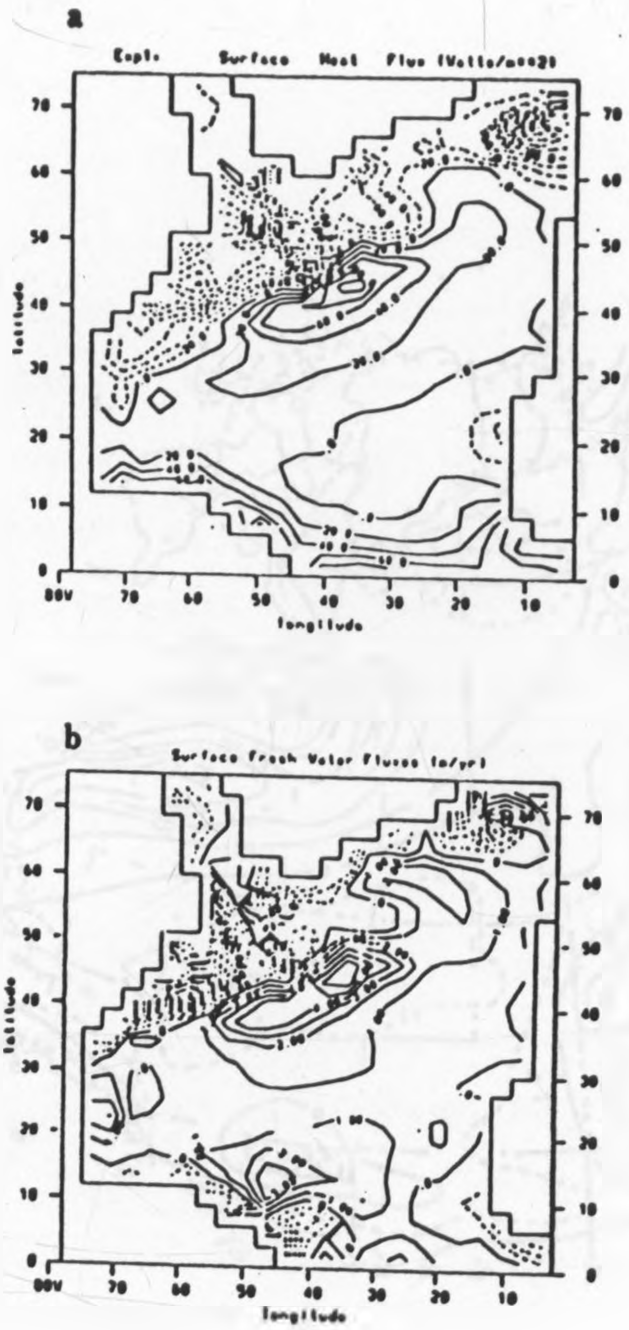

Figure 5: a) Surface heat flux (Wm^{-2}) and b) surface freshwater flux ($myear^{-1}$) diagnosed from the equilibrium state of Exp. 1. Positive values indicate heat into and fresh water out of the basin (i.e., net evaporation), respectively. The contour interval in a) is 20 Wm^2 and in b) 1 myr^{-1}.

Figure 6: Surface heat flux estimates for the North Atlantic taken from Bunker (1976). Positive values indicate heat into the ocean. The contour interval is 50 Wm^{-2}.

of the sub-tropical gyre: the south-east to north-west orientation that was apparent at the surface is now replaced by a more zonal one with westward flow at its southern flank. Associated with this is a reversal of flow along the northeastern coast of south America from northwestward at the surface to southeastward at 450 m. The equatorial undercurrent that was well defined at 125 m (not shown) is still apparent though much weaker. The maximum temperature is located in the recirculation region where the thermocline is deepest. The vertical velocity at this level (figure 7c) is downward in the sub-tropical gyre and upward in the sub-polar gyre, consistent with Ekman convergence in the former and divergence in the latter, and quite uniform over most of the interior. The upwelling along the western boundary and the eastern coast of Greenland remains quite strong. The strong downwelling near 65°N in the northeastern portion of the domain persists.

At a level well below the thermocline (3870 m) the temperature and salinity are very uniform in the interior. The deep undercurrent is the strongest feature of the horizontal velocity field (figure 8a) at this level; as it travels equatorward, the undercurrent rises in the western boundary current region of the model. The vertical velocity pattern (figure 8b) exhibits upwelling along the eastern coast of Greenland, strong downwelling in the northeastern portion along the eastern boundary of the domain at about 65°N, and a weak pattern over the rest of the domain.

The total meridional transport of heat by the ocean is the sum of the advective and diffusive components. The total advection can be decomposed into: Ekman transport, calculated from the surface wind stress and temperature in the top model grid boxes; transport by "z-mean", a barotropic gyre component due to advection of vertically averaged temper-

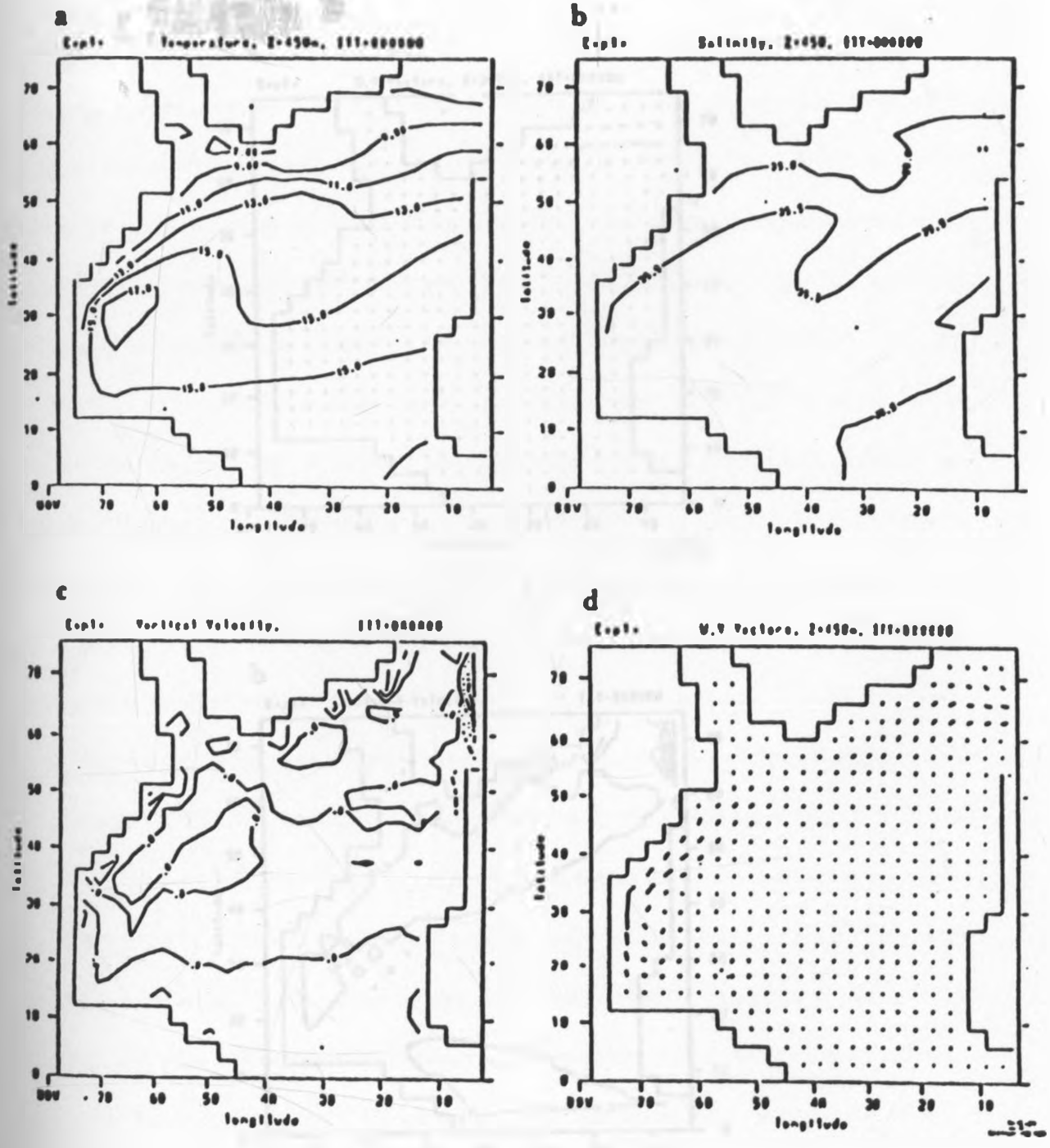

Figure 7: a) Temperature ($°C$) for Exp. 1 at 450 m, b) salinity (psu) for Exp. 1 at 450 m, c) vertical velocity (10^{-4} cms^{-1}) for Exp. 1 at 510 m, and d) horizontal velocity (cms^{-1}) for Exp. 1 at 450 m. The contour interval in a) is 2 $°C$, in b) 0.5 psu. The maximum horizontal vector in d) is 9.0 cms^{-1}.

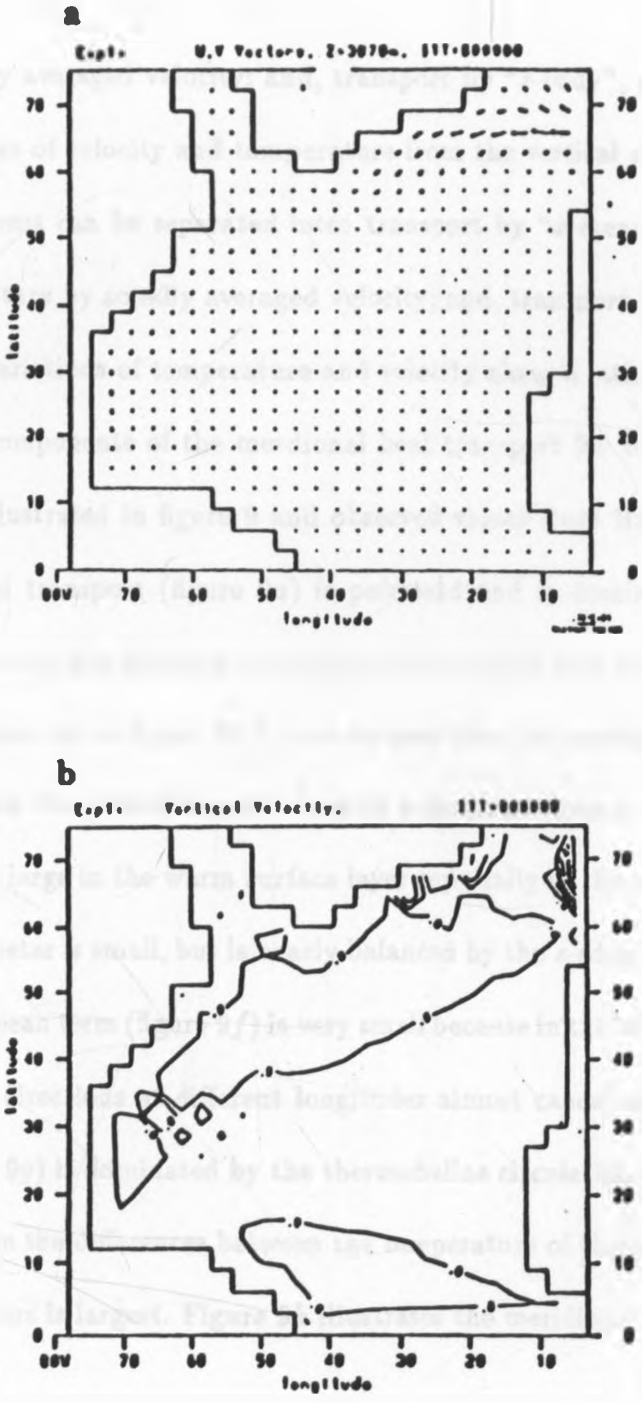

Figure 8: Exp 1: a) Horizontal velocity vectors (cms^{-1}) at 3870 m and b) vertical velocity (10^{-4} cms^{-1}) at 3720 m. The maximum horizontal velocity vector in a) is 7 cms^{-1}.

ature by vertically averaged velocity; and, transport by "z-eddy", a baroclinic term which involves departures of velocity and temperature from the vertical mean. Alternatively the advective component can be separated into: transport by "z-mean", advection of zonally averaged temperature by zonally averaged velocity; and, transport by "z-eddy", a residual quantity due to variations of temperature and velocity along a latitude circle.

Plots of the components of the merdional heat transport for the reference solution at equilibrium are illustrated in figure 9 and observed values from Hastenrath (1980) in figure 10. The total transport (figure 9*a*) is poleward and is dominated by the advective component (figure 9*b*); the diffusive term (figure 9*c*) is small and at times opposite in sign. On comparing figure 9*a* to figure 10 it can be seen that the model total meridional heat transport is smaller than the observed values by a factor of three or so. The Ekman transport (figure 9*d*) is large in the warm surface layer especially in the equatorial region where the Coriolis parameter is small, but is nearly balanced by the z-eddy term (figure 9*e*) at low latitudes. The z-mean term (figure 9*f*) is very small because in the wind-driven gyres, transports in opposite directions at different longitudes almost cancel one another. Transport by x-mean (figure 9*g*) is dominated by the thermohaline circulation and is very effective at low latitudes where the differences between the temperature of the surface waters and that of the bottom waters is largest. Figure 9*h* illustrates the meridional transport by x-eddy.

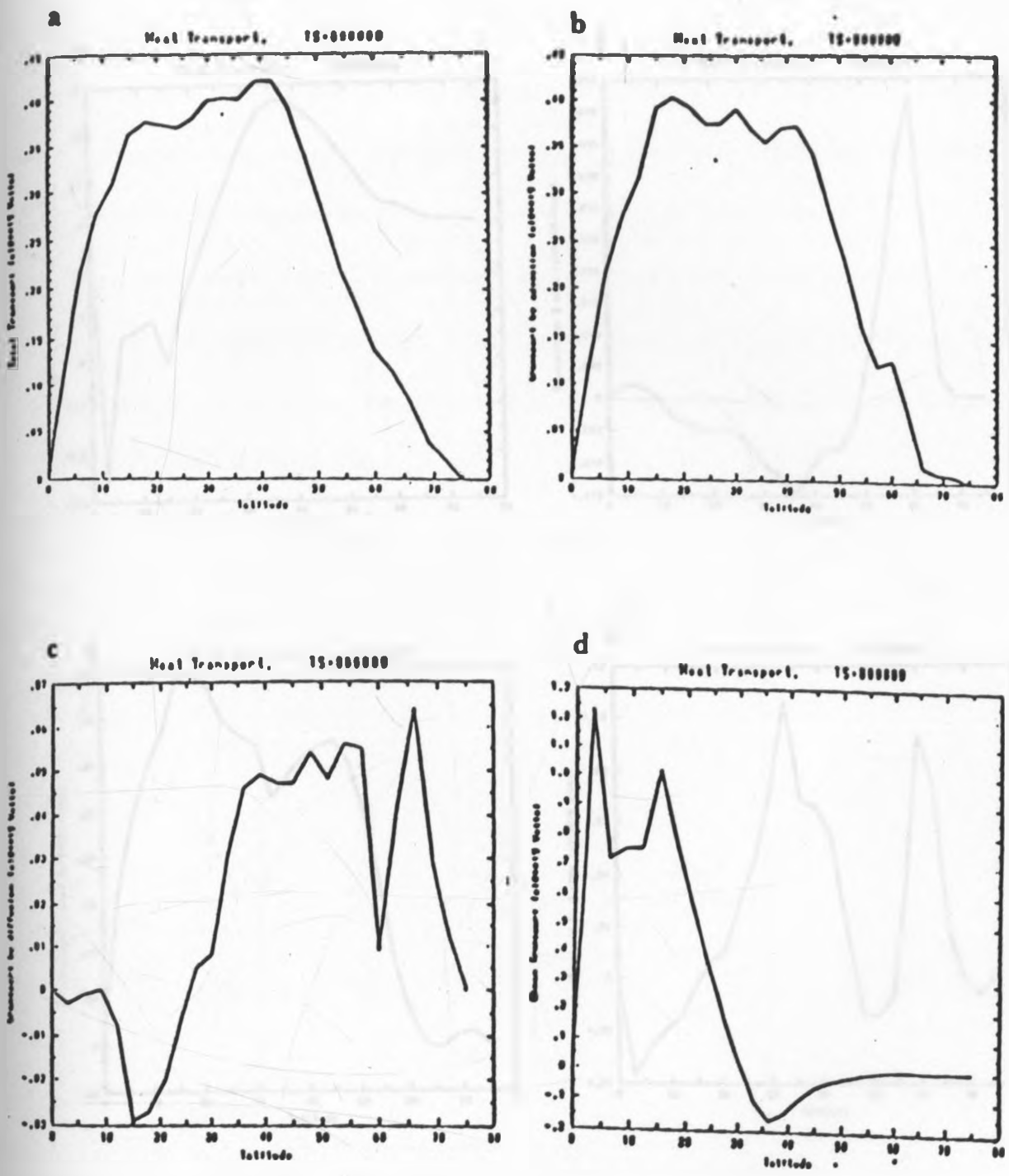

Figure 9: Exp 1: Meridional heat transport at equilibrium, in Petawatts ($1\ PW = 10^{15}\ W$); a) Total transport, b) transport by advection, c) transport by diffusion, d)Ekman transport, e) transport by z-eddy, f) transport by z-mean, g) transport by z-mean and h) transport by z-eddy.

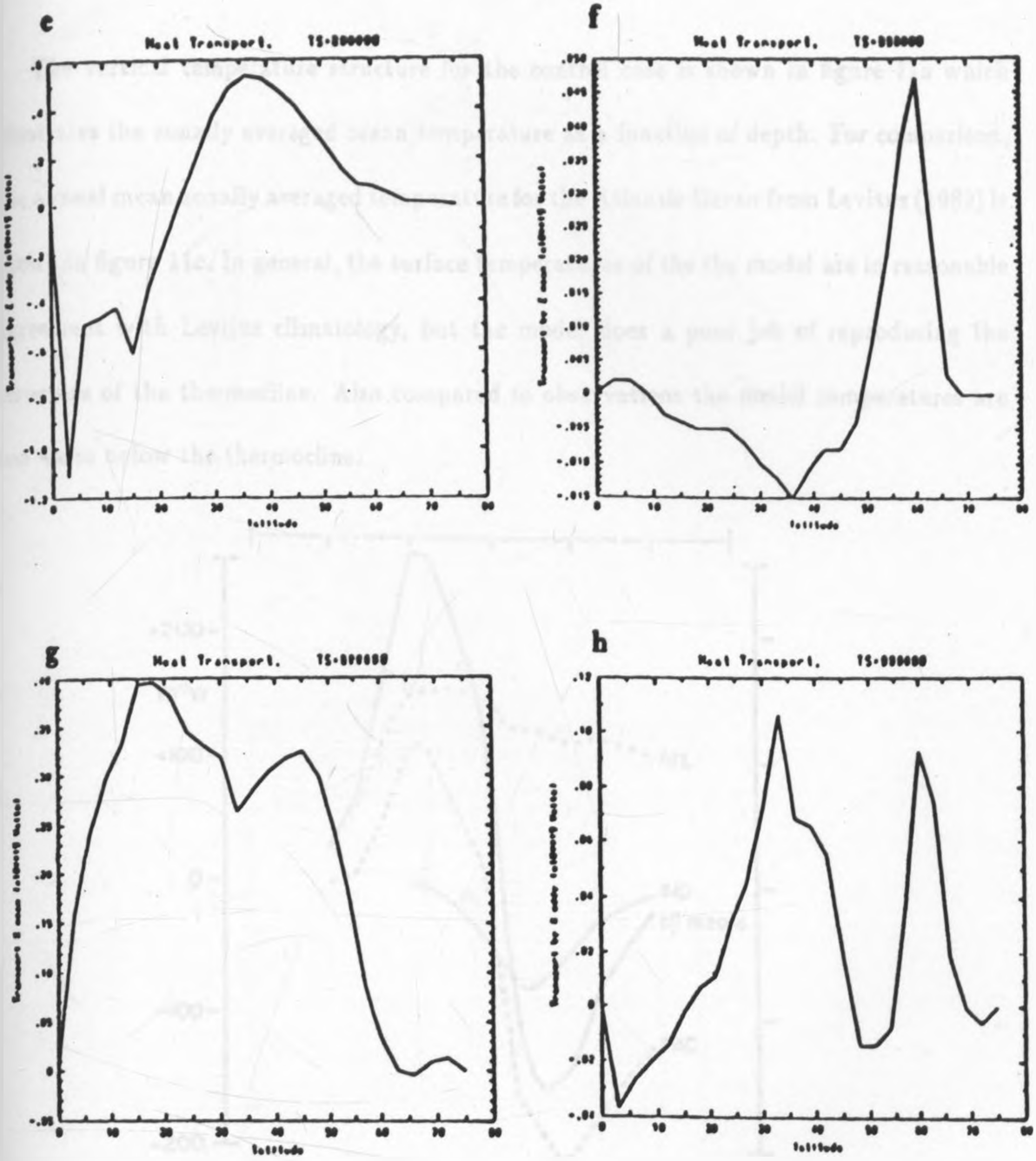

Figure 9: Exp 1: Meridional heat transport at equilibrium, in Petawatts ($1\ PW = 10^{15}\ W$); a) Total transport, b) transport by advection, c) transport by diffusion, d)Ekman transport, e) transport by x-eddy, f) transport by x-mean, g) transport by x-mean and h) transport by x-eddy.

The vertical temperature structure for the control case is shown in figure 11a which illustrates the zonally averaged ocean temperature as a function of depth. For comparison, the annual mean zonally averaged temperature for the Atlantic Ocean from Levitus (1982) is shown in figure 11c. In general, the surface temperatures of the the model are in reasonable agreement with Levitus climatology, but the model does a poor job of reproducing the structure of the thermocline. Also compared to observations the model temperatures are too warm below the thermocline.

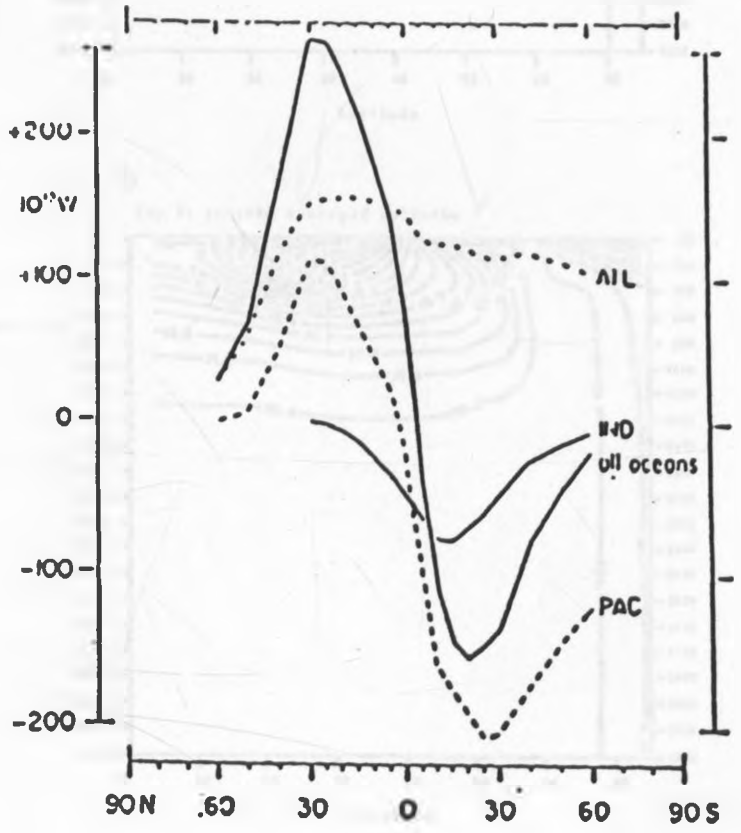

Figure 10: Annual mean meridional heat transports by the Indian (thin solid), Atlantic (dash dotted) and Pacific (dashed) and all oceans combined (heavy solid) taken from Hastenrath (1980). Units are 10^{13} W.

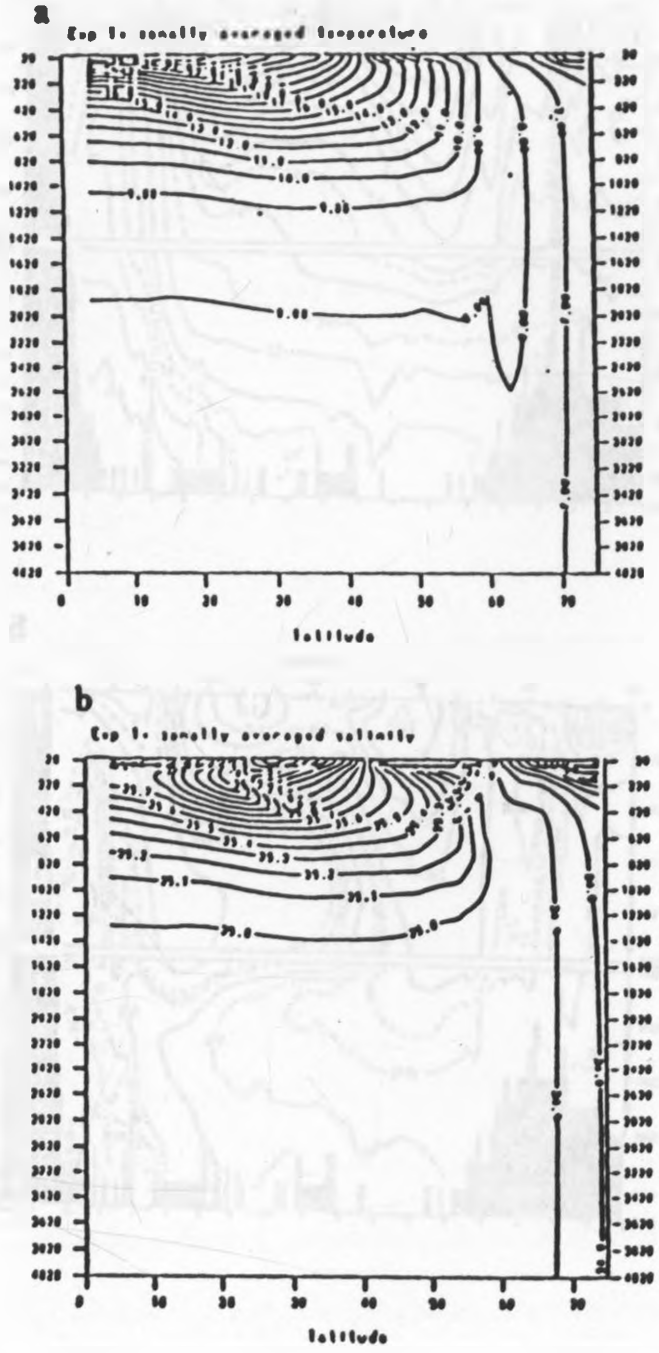

Figure 11: a) Zonally averaged temperature ($°C$) for Exp. 1 as a function of depth, b) zonally averaged salinity (psu) for Exp 1 as functions of depth, c) annual mean zonally averaged temperature ($°C$) from Levitus (1982) and d) annual mean zonally averaged salinty (psu) from Levitus (1982).

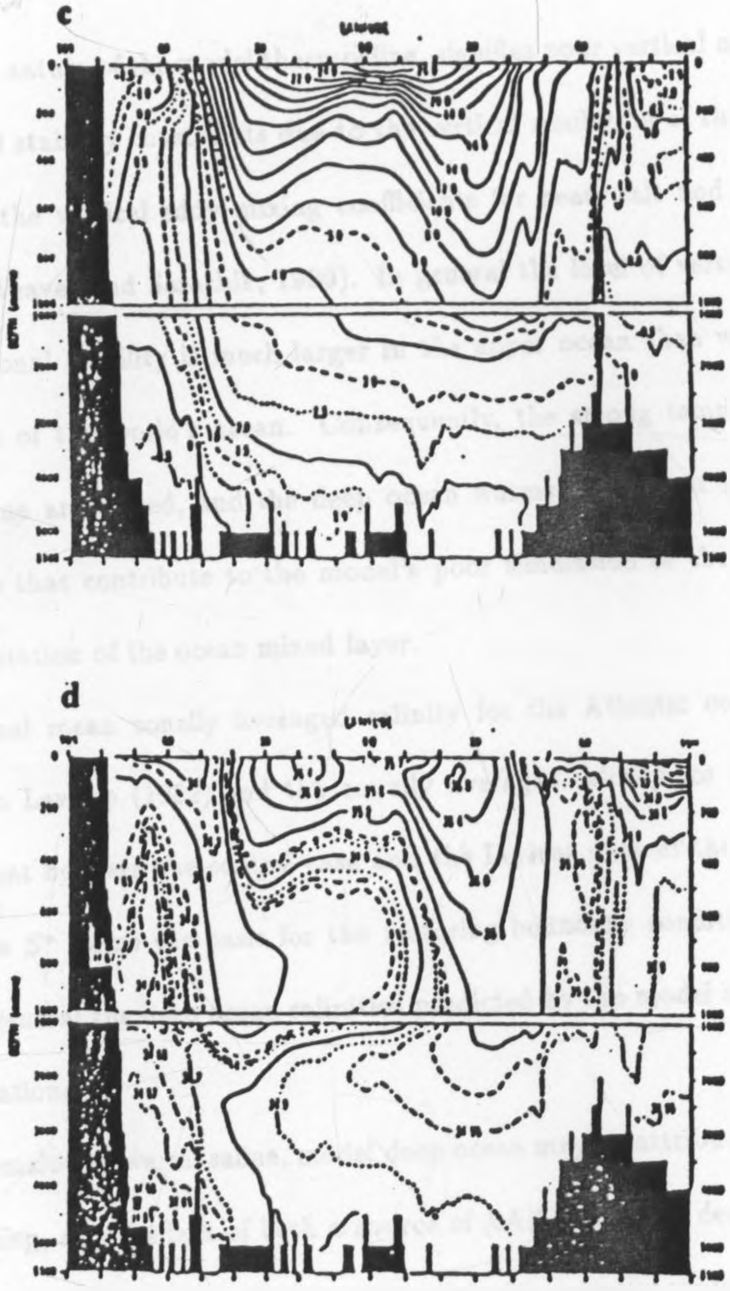

Figure 11: a) Zonally averaged temperature (°C) for Exp. 1 as a function of depth, b) zonally averaged salinity (psu) for Exp 1 as functions of depth, c) annual mean zonally averaged temperature (°C) from Levitus (1982) and d) annual mean zonally averaged salinty (psu) from Levitus (1982).

The diffuse nature of the model thermocline, signifies poor vertical mixing in the model. Computational stability constraints due to the vertical resolution of the model restrict the magnitude of the vertical eddy mixing coefficients for heat, salt and momentum (Bryan et al., 1975; Weaver and Sarachik, 1990). In general the level of vertical mixing required for computational stability is much larger in the upper ocean than would be anticipated in most areas of the world's ocean. Consequently, the strong temperature gradients of the thermocline are erased, and the deep ocean warms up as heat is mixed downwards. Other factors that contribute to the model's poor simulation of the thermocline include poor representation of the ocean mixed layer.

The annual mean zonally averaged salinity for the Atlantic ocean is shown in figure 11*d* from Levitus (1982) and the zonally averaged salinity for Exp. 1 in figure 11*b*. The agreement between the control case and the Levitus data at the surface is reasonable since Levitus S^* forms the basis for the restoring boundary condition on salinity during Exp. 1. In general the deep ocean salinities predicted by the model are up to 0.2 *psu* more than observations.

The anomalously warm, saline, model deep ocean may be attributed to the use of steady surface forcing, and the lack of both a source of AABW and the deep overflow water from the Arctic basin in the model. Forcing the model with annually averaged fields results in the regions of deep water formation (cf. figure 12*a*) being coincident with regions in which the surface restoring σ_t is largest; both T (figure 11*a*) and S (figure 11*b*) are relatively high at $65^o - 70^o$ (figure 8*b*) where deep water forms. In reality, the ocean and atmosphere interact continually with each other; the forcing is never steady. Accounting for time dependence

in the forcing, in terms of seasonality for example, may yield more realistic deep ocean temperature and salinity structures. Further, parameterization of the deep AABW and the Arctic water mass input into the model domain would be appropriate.

The meridional overturning streamfunction is generally thought of as a manifestation of the thermohaline circulation and may be derived from the continuity equation as follows: Consider the continuity equation in spherical coordinates,

$$u_\lambda + (v\cos\phi)_\phi + a\cos\phi w_z = 0 \tag{11}$$

where a is the radius of the earth. The zonal integration of equation (11) from the western boundary λ(west) to the eastern boundary λ(east) yields,

$$\int_{\lambda(west)}^{\lambda(east)} (v\cos\phi)_\phi d\lambda + a\cos\phi \int_{\lambda(west)}^{\lambda(east)} w_z d\lambda = 0 \tag{12}$$

since $u = 0$ at λ(west), λ(east). Equation (12) is non-divergent and the meridional overturning streamfunction Φ may therefore be defined by,

$$-\Phi_z = \int_{\lambda(west)}^{\lambda(east)} va\cos\phi d\lambda \tag{13}$$

$$\frac{1}{a}\Phi_\phi = \int_{\lambda(west)}^{\lambda(east)} wa\cos\phi d\lambda \tag{14}$$

Figure 12 shows the meridional overturning streamfunction (Φ) for the reference experiment at equilibrium. The model attains this steady state within a few hundred years of integration as illustrated by a plot of the kinetic energy density (figure 13). The dominant

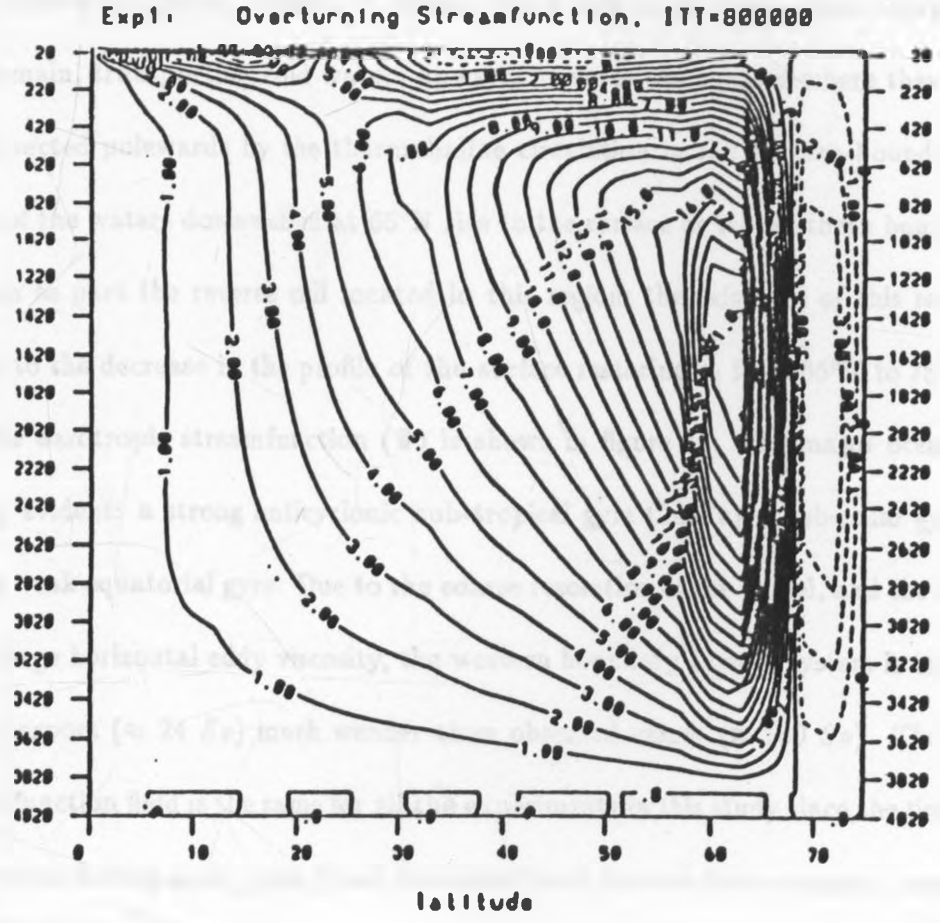

Figure 12: The meridional overturning stream function (Φ) for the reference case at equilibrium. Units are Sverdrups ($1\ Sv = 10^6\ m^3 s^{-1}$).

feature of the meridional volume transport is the sinking region near 65°N of about 22 Sv due to the formation of North Atlantic Deep Water (NADW). This value is comparable with observed estimates in the range $15 - 20$ Sv (e.g., Hall and Bryden, 1982; Gordon, 1986). The rate of deep water formation is, however, dependent upon the magnitude of the vertical eddy diffusivity (Bryan, 1986*a*). A broad return flow in the deep ocean occupies most of the domain, transporting cold waters upwards towards the equator where they warm, and are advected polewards by the thermohaline circulation in the western boundary current. Some of the waters downwelled at 65°N rise to the surface at the northern boundary of the domain as part the reverse cell located in this region; the existence of this reverse cell is linked to the decrease in the profile of the surface restoring σ_t from 65°N to 75°N.

The barotropic streamfunction (Ψ) is shown in figure 14. The major ocean gyres are clearly evident: a strong anticyclonic sub-tropical gyre (24 Sv); a sub-polar gyre (10 Sv); and, a weak equatorial gyre. Due to the coarse resolution of the model, and the correspondingly large horizontal eddy viscosity, the western boundary current system is too wide, and the transport ($\approx$ 24 Sv) much weaker than observed values ($\approx$ 100 Sv). The barotropic streamfunction field is the same for all the experiments in this study since the time-invariant wind stress forcing is the same for all the model runs; the non-linear terms in the momentum equations are neglected; and, the ocean is flat-bottomed.

4.2.2 Experiment 2.

This case, Exp. 2, was started from a resting homogeneous state with temperature of 5 $^{\circ}C$ and salinity 35.12 *psu*. To simulate Arctic fresh water flux into the North Atlantic, 0.1 Sv

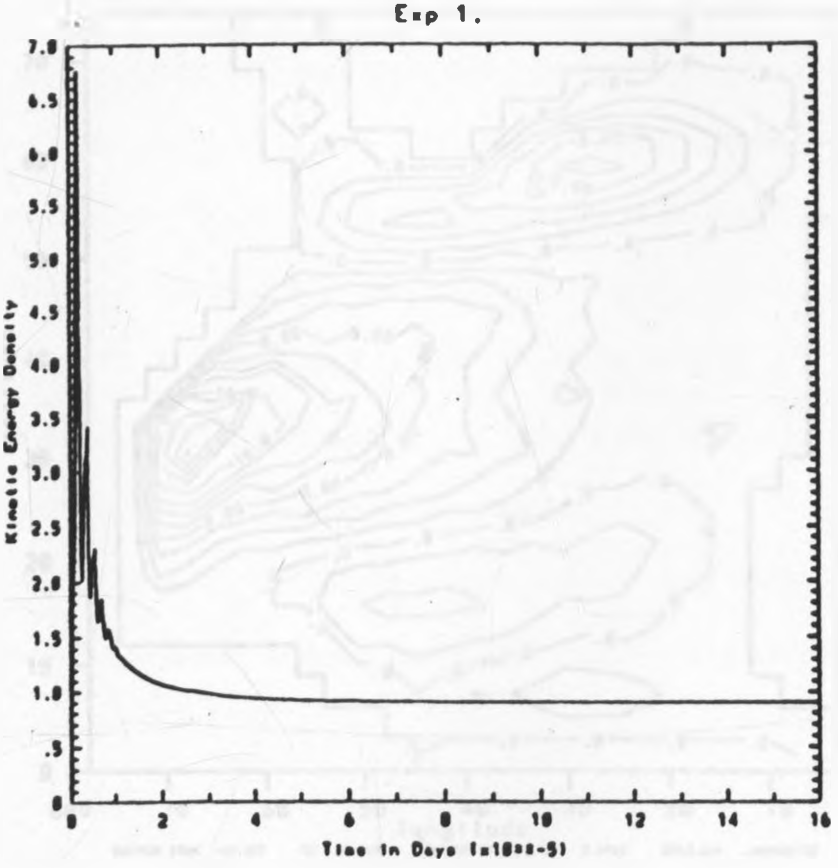

Figure 13: a) Time series of kinetic energy throughout the 4381 years of integration of the control experiment. Units are $10^{-1}\ kgm^{-1}s^{-2}$.

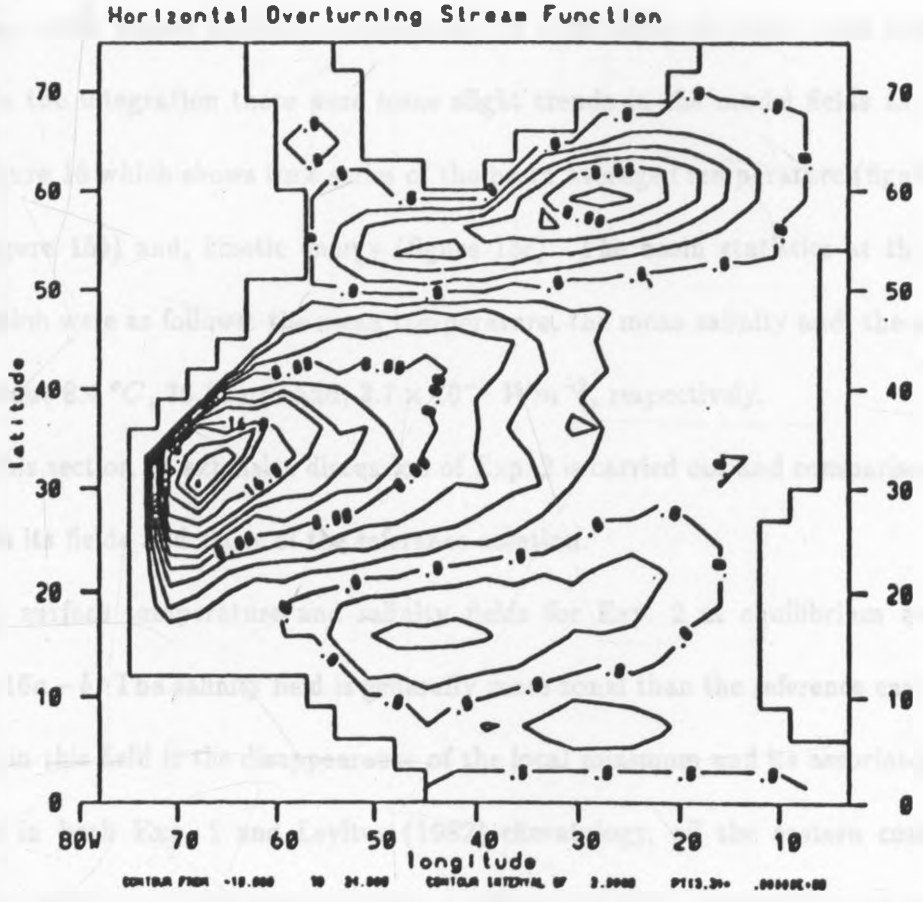

Figure 14: The barotropic stream function (Ψ) for all the model runs. Units are Sverdrups ($1\ Sv = 10^6\ m^3 s^{-1}$).

of fresh water were distributed evenly in the top 210 m of the northernmost grid boxes i.e., in both the "Labrador" and the "Greenland Seas". Further, the equatorial flux condition was imposed at the southern boundary of the domain. The model was integrated forward in time, under mixed boundary conditions, for 2190 years of tracer time steps. At this point in the integration there were some slight trends in the model fields as can be seen from figure 15 which shows time series of the basin averaged temperature (figure 15a), heat flux (figure 15b) and, kinetic energy (figure 15c). The basin statistics at the end of the integration were as follows: the mean temperature, the mean salinity and, the net heat flux were about 8.4 ^{o}C, 35.12 psu and, $3.7 \times 10^{-2}\ Wm^{-2}$, respectively.

In this section an extensive discussion of Exp. 2 is carried out and comparisons are made between its fields and those of the reference solution.

The surface temperature and salinity fields for Exp. 2 at equilibrium are shown in figures 16$a-b$. The salinity field is generally more zonal than the reference case. A notable feature in this field is the disappearance of the local minimum and its associated gradients, evident in both Exp. 1 and Levitus (1982) climatology, off the eastern coast of North America, where the Saint Lawrence river outflows and the Labrador Current exports fresh water equatorwards and the Gulf Stream separates. Figures 16$c-d$ show the differences in temperature and salinity between Exp. 2 and Exp. 1. It is found that: Exp. 2 is cooler and fresher than Exp. 1 in the equatorial region and in the northern part of the domain; Exp. 2 is cooler and more saline than Exp. 1 south of Greenland and in the northern Labrador Sea; and, Exp. 2 is both significantly warmer and more saline than Exp. 1 in the Gulf Stream region.

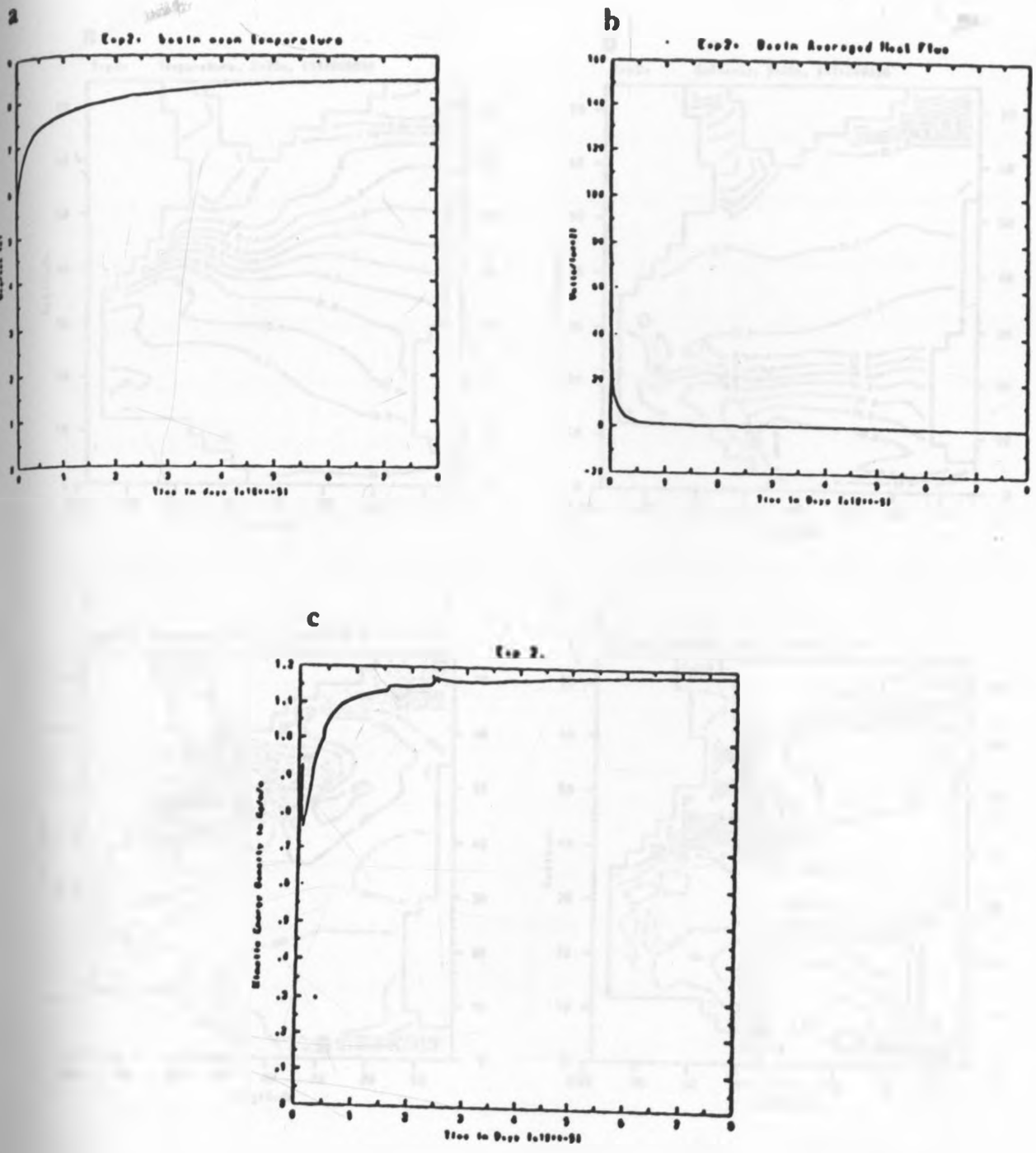

Figure 15: Time series of basin averaged a) temperature (°C), b) heat flux (Wm^{-2}) and c) kinetic energy density ($10^{-1}\ kgm^{-1}s^{-2}$) throughout the 2190 years of integration of Exp. 2.

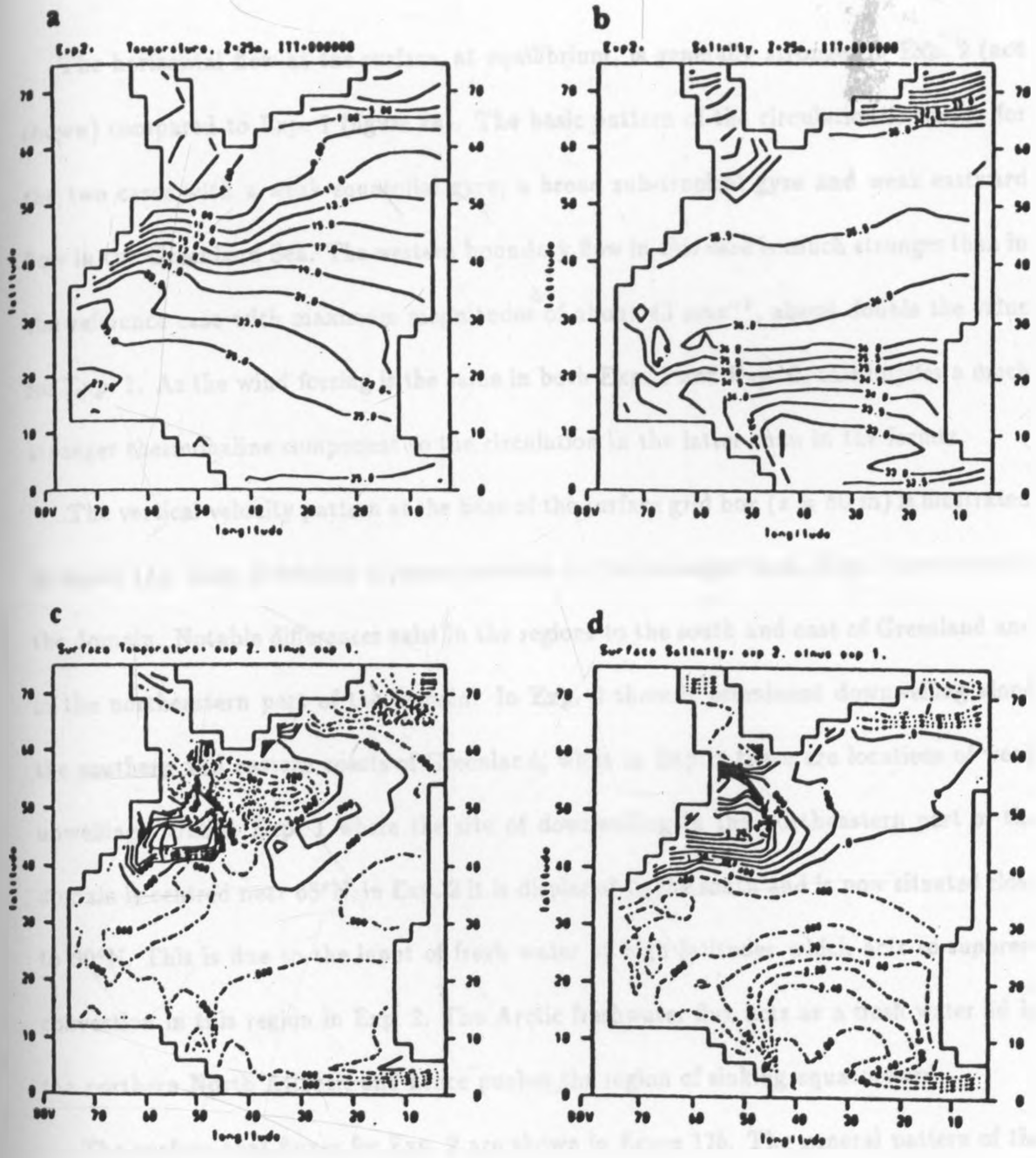

Figure 16: a) Surface ($z = 25\ m$) temperature ($°C$) for Exp. 2, b) surface salinity (psu) for Exp. 2, c) temperature ($°C$) differences between Exp. 2 and Exp. 1 (Exp. 2 - Exp. 1), and d) salinity (psu) differences between Exp. 2 and Exp. 1 (Exp. 2 - Exp. 1).

The horizontal flow at the surface, at equilibrium, is generally stronger in Exp. 2 (not shown) compared to Exp. 1 (figure 4*a*). The basic pattern of the circulation is similar for the two cases with a weak equatorial gyre, a broad sub-tropical gyre and weak eastward flow in the Greenland Sea. The western boundary flow in this case is much stronger than in the reference case with maximum magnitudes of about 43 cms^{-1}, about double the value for Exp. 1. As the wind forcing is the same in both Exp. 1 and Exp. 2, this implies a much stronger thermohaline component to the circulation in the latter than in the former.

The vertical velocity pattern at the base of the surface grid box ($z = 50\ m$) is illustrated in figure 17*a*. Exp. 2 exhibits a pattern similar to, but stronger than, Exp. 1 over most of the domain. Notable differences exist in the regions to the south and east of Greenland and in the northeastern part of the domain. In Exp. 2 there is prominent downwelling along the southern and eastern coasts of Greenland, while in Exp. 1 these are locations of weak upwelling. Unlike Exp. 1 where the site of downwelling in the northeastern part of the domain is centred near 65°N, in Exp. 2 it is displaced to the south and is now situated close to 60°N. This is due to the input of fresh water at high latitudes which acts to suppress convection in this region in Exp. 2. The Arctic freshwater flux acts as a fresh water lid in the northern North Atlantic and hence pushes the region of sinking equatorward.

The surface heat fluxes for Exp. 2 are shown in figure 17*b*. The general pattern of the locations of the areas of heat loss and gain is similar for both Exp. 2 and Exp. 1 but the magnitudes are generally higher in Exp. 2. Notable differences in the surface heat fluxes for the two model runs are as follows: Exp. 2 exhibits larger magnitudes than Exp. 1 in the equatorial region and in the northern Gulf Stream due to a stronger thermohaline circula-

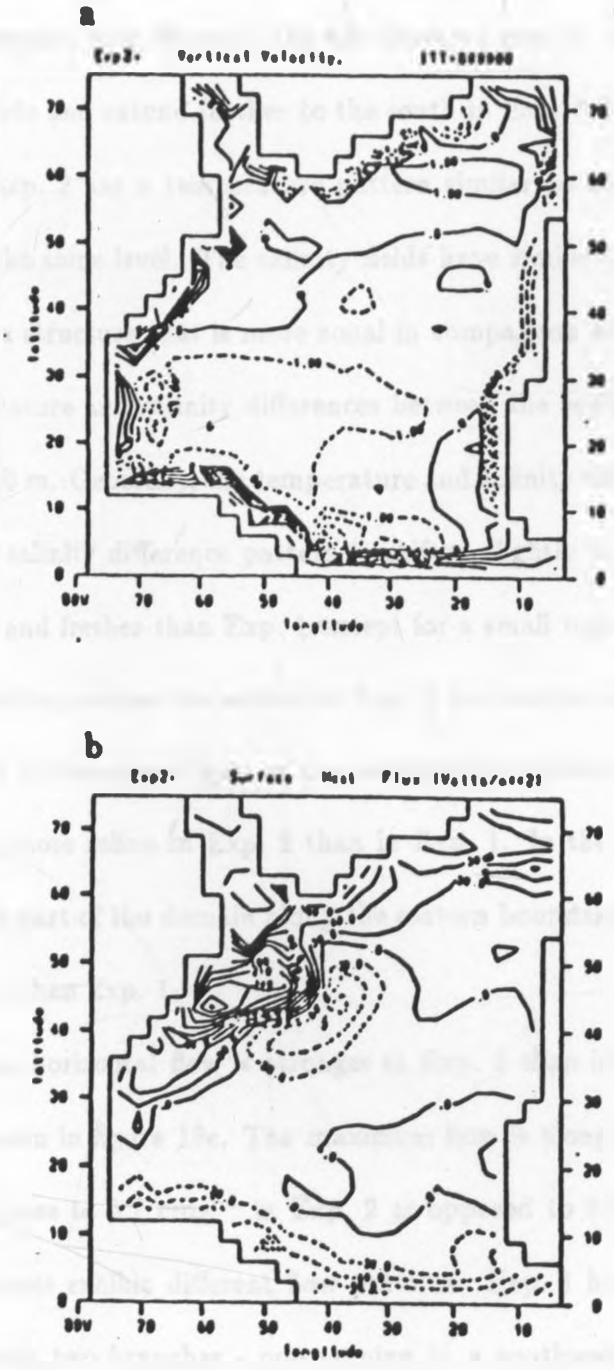

Figure 17: Exp. 2 a) vertical velocity (10^{-4} cms^{-1}) at the base of the surface grid box i.e., z = 50 m and b) surface (z = 25 m) heat flux (Wm^{-2}) diagnosed at equilibrium. Positive values indicate heat into the basin and upwelling, respectively.

tion; and, the negative heat fluxes in the northeastern part of the domain are significantly lower in magnitude and extend further to the south in Exp. 2 in comparison with Exp. 1.

At 450 m, Exp. 2 has a temperature pattern similar to but less zonal in comparison with Exp. 1 at the same level. The salinity fields have similar patterns for both cases but Exp. 2 exhibits a structure that is more zonal in comparison with Exp. 1. Figures 18a – b show the temperature and salinity differences between the equilibrium solutions of Exp. 2 and Exp. 1 at 450 m. Generally, the temperature and salinity difference patterns are similar except that the salinity difference pattern is shifted slightly to the west. South of 50°N, Exp. 2 is cooler and fresher than Exp. 1 except for a small region located near 30°N along the eastern boundary where the waters in Exp. 2 are warmer and more saline than those in Exp. 1. In the northernmost part of the northeastern portion of the domain, the waters are warmer and more saline in Exp. 2 than in Exp. 1. In the vicinity of 60° latitude, in the northeastern part of the domain along the eastern boundary, the waters are cooler and fresher in Exp. 2 than Exp. 1.

At 450 m the horizontal flow is stronger in Exp. 2 than in Exp. 1. The flow pattern for Exp. 2 is shown in figure 18c. The maximum flow is along the western boundary and has magnitude close to 9.7 cms^{-1} in Exp. 2 as opposed to 9.1 cms^{-1} in Exp. 1. In the north the two cases exhibit different flow patterns: Exp. 1 has eastward flow just south of Greenland with two branches - one turning in a southwestward direction to become part of the subtropical gyre and the other moving northeastward and eastward into the Greenland Sea, converging at the northeastern boundary near 65°N where deep water forms (cf. figure 7d); In Exp. 2, on the other hand, the thermohaline circulation converges towards

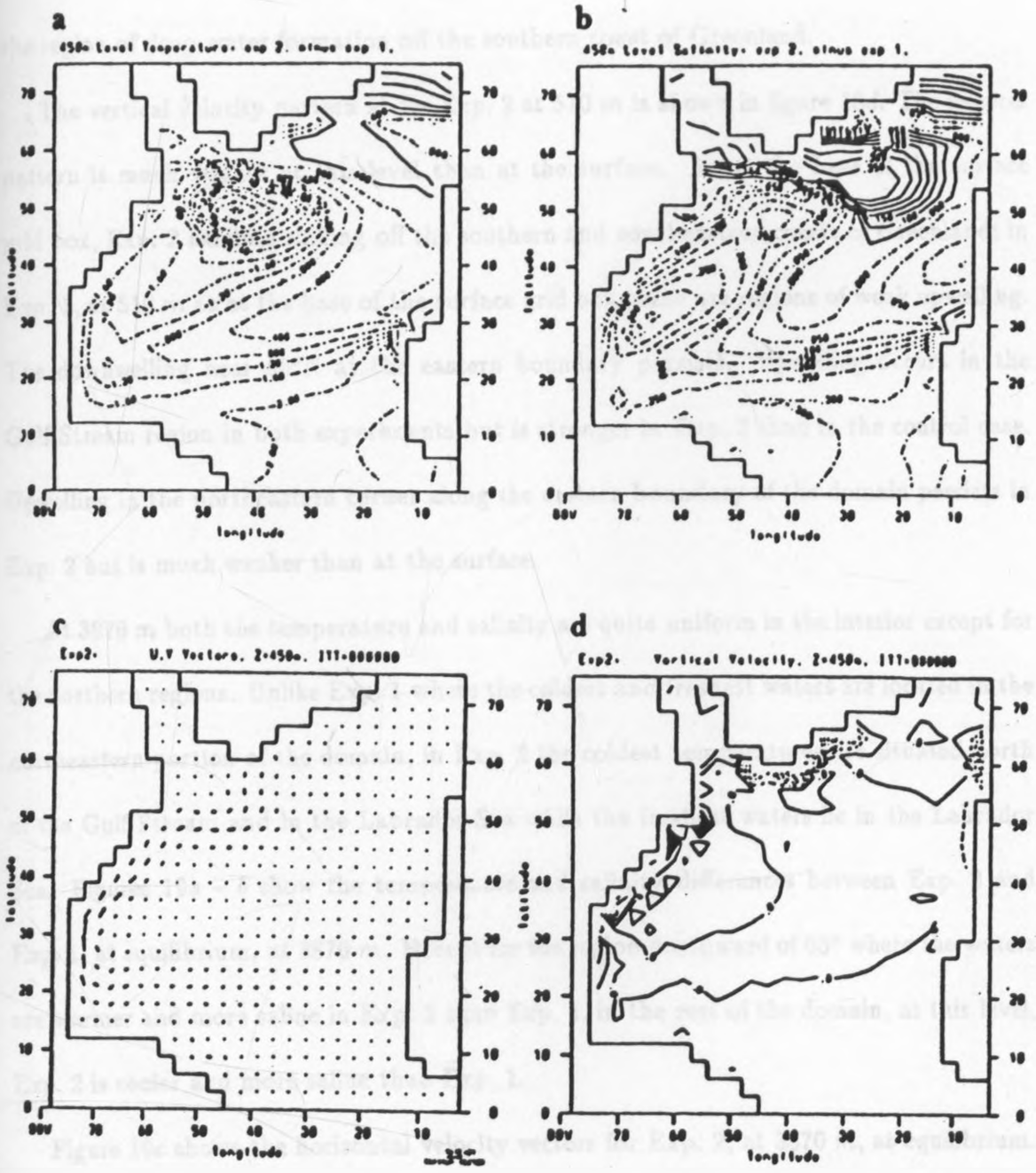

Figure 18: a) Temperature ($°C$) differences between Exp. 2 and Exp. 1 (Exp. 2 - Exp. 1) at 450 m, b) salinity (psu) differences between Exp. 2 and Exp. 1 (Exp. 2 - Exp. 1) at 450 m, c) horizontal velocity vectors (cms^{-1}) for Exp. 2 at 450 m and d) vertical velocity (10^{-4} cms^{-1}) for Exp. 2 at 510 m. The contour interval in a) is 0.4 $°C$, in b) 0.4 psu. The maximum horizontal velocity vector is 9.7 cms^{-1}.

the region of deep water formation off the southern coast of Greenland.

The vertical velocity pattern at for Exp. 2 at 510 m is shown in figure 18d. The general pattern is much weaker at this level than at the surface. As at the base of the surface grid box, Exp. 2 exhibits sinking off the southern and southeastern coasts of Greenland; in Exp. 1, at 510 m as at the base of the surface grid box these are regions of weak upwelling. The downwelling near 65°N at the eastern boundary persists. Upwelling occurs in the Gulf Stream region in both experiments but is stronger in Exp. 2 than in the control case. Upwelling in the northeastern corner along the eastern boundary of the domain persists in Exp. 2 but is much weaker than at the surface.

At 3870 m both the temperature and salinity are quite uniform in the interior except for the northern regions. Unlike Exp. 1 where the coldest and freshest waters are located in the northeastern portion of the domain, in Exp. 2 the coldest temperatures are situated north of the Gulf Stream and in the Labrador Sea while the freshest waters lie in the Labrador Sea. Figures 19a – b show the temperature and salinity differences between Exp. 2 and Exp. 1, at equilibrium, at 3870 m. Except for the region northward of 65° where the waters are warmer and more saline in Exp. 2 than Exp. 1, in the rest of the domain, at this level, Exp. 2 is cooler and more saline than Exp. 1.

Figure 19c shows the horizontal velocity vectors for Exp. 2, at 3870 m, at equilibrium. As in Exp. 1 the strongest feature of the horizontal flow field is the deep return path of the thermohaline circulation. The flow patterns differ considerably between the two experiments (cf. figure 8a and figure 19c) reflecting the different sites of deep water formation.

The vertical velocity field for Exp. 2 at 3720 m is shown in figure 19d. There are major

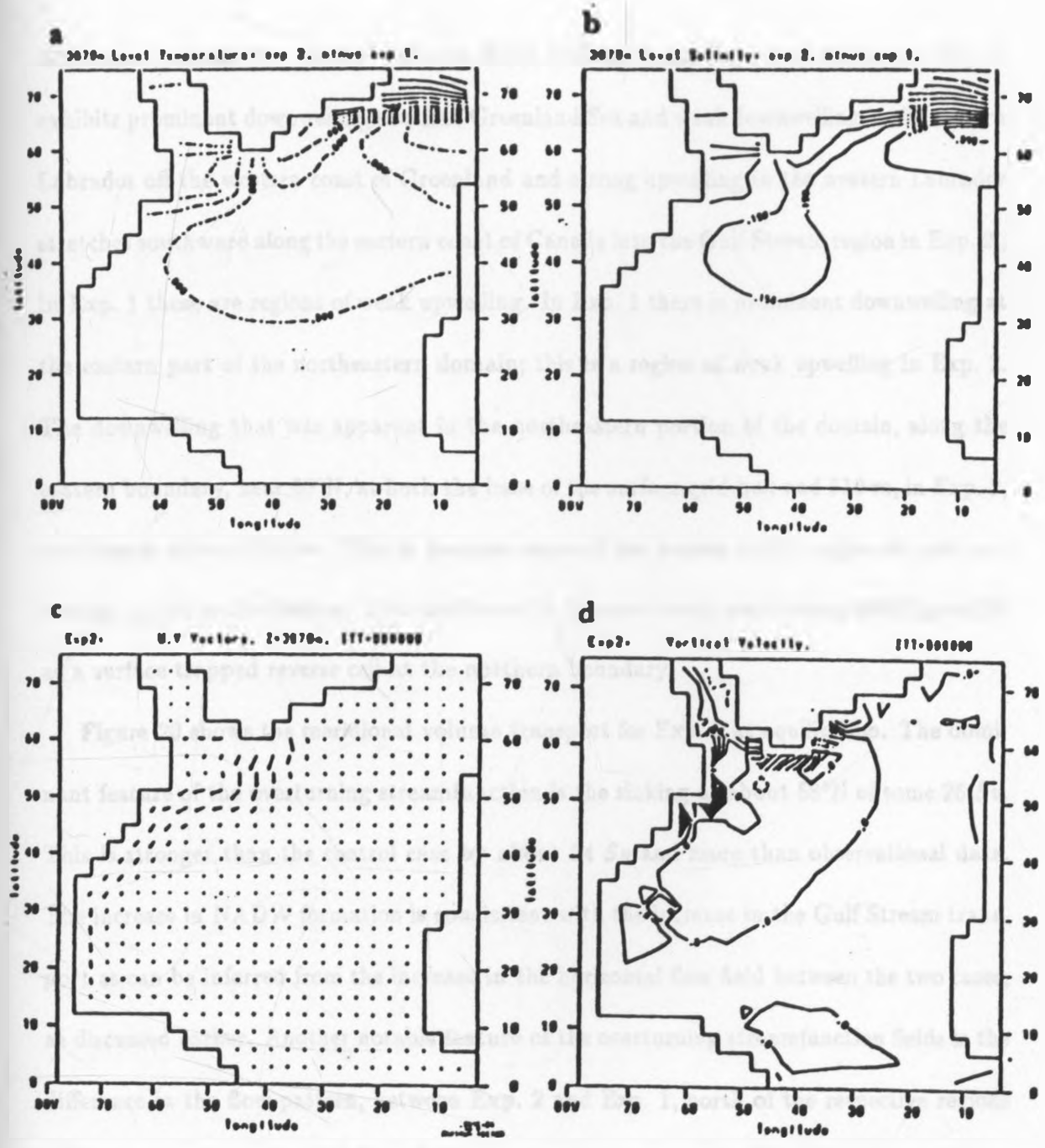

Figure 19: a) Temperature (°C) differences between Exp. 2 and Exp. 1 (Exp. 2 - Exp. 1) at 3870 m, b) salinity (psu) differences between Exp. 2 and Exp. 1 (Exp. 2 - Exp. 1) at 3870 m, c) horizontal velocity vectors (cms^{-1}) for Exp. 2 at 3870 m and d) vertical velocity w (10^{-4} cms) for Exp. 2 at 3720 m. Positive values of w indicate upwelling.

differences between the vertical velocity fields of Exp. 2 and Exp. 1 at this level: Exp. 2 exhibits prominent downwelling south of Greenland Sea and weak downwelling in the eastern Labrador off the western coast of Greenland and strong upwelling in the western Labrador stretches southward along the eastern coast of Canada into the Gulf Stream region in Exp. 2.; In Exp. 1 these are regions of weak upwelling. In Exp. 1 there is prominent downwelling at the eastern part of the northeastern domain; this is a region of weak upwelling in Exp. 2. The downwelling that was apparent in the northeastern portion of the domain, along the eastern boundary, near 60°N, at both the base of the surface grid box and 510 m, in Exp. 2, vanishes at about 1320 m. This is because some of the waters in this region do not cool enough to sink to the bottom. This is reflected in the meridional overturning field (figure 20) as a surface trapped reverse cell at the northern boundary.

Figure 20 shows the meridional volume transport for Exp. 2 at equilibrium. The dominant feature of the overturning streamfunction is the sinking at about 58°N of some 26 Sv. This is stronger than the control case by about 24 Sv and more than observational data. The increase in NADW formation is consisitent with the increase in the Gulf Stream transport as can be inferred from the increase in the horizontal flow field between the two cases, as discussed earlier. Another notable feature of the overturning streamfunction fields is the difference in the flow pattern, between Exp. 2 and Exp. 1, north of the respective regions of deep water formation. In Exp. 1 there is one major reverse cell in this region whereas in Exp. 2 there are two: a surface trapped cell of about 2 Sv and a bottom-trapped cell of about 3 Sv. The position of the lower cell coincides with that of the warm water patch, observed in the zonally averaged temperature field (figure 21a), in the deep ocean, as dis-

cussed below. At the northern boundary, north of 70°N, below 1020 m in Exp. 2, unlike Exp. 1, there are signs of weak positive overturning in the plot of the streamfunction.

The Arctic flux acts as a fresh water lid in the northern North Atlantic thereby inhibiting deep convection far to the north; deep water now forms more equatorward in Exp. 2 than Exp. 1, as discussed above. This results in a warmer, more saline, model deep ocean in the former compared to the latter, as discussed below.

The zonally averaged temperature field for the equilibrium solution of Exp. 2 is shown in figure 21a. The zonally averaged temperature structure is quite similar to that for the control case (cf. figure 11a) except that the deep ocean is warmer in Exp. 2: the 8° isotherm is located between 820 m and 1020 m in Exp. 2 while in Exp. 1 it is situated at a much lower depth i.e, at about 2020 m. Major differences in the temperature fields exist between the two cases in the deep ocean. Whereas in Exp. 1 temperatures are lower than 7 $°C$, from the surface to the bottom of the basin, northward of 70°N, in Exp. 2 the temperature structure in this region is slightly more complicated. In the northern north Atlantic, Exp. 2 has a pool of relatively warm water trapped at the surface above 220 m between 65°N and the northern boundary; and, below 1620 m, northward of 60°N, the 7° isotherm separates the warmer basin from a pool of cooler waters in the middle of which is located a patch of relatively warmer water centred near 65°N.

The zonally averaged ocean salinity for Exp. 2 is illustrated in figure 21b. The basic structure is similar to that for Exp. 1 (cf. figure 11b) especially at the surface. The magnitudes at the surface are comparable for Exp. 2 and Exp. 1. Differences exist in both the salinity patterns and magnitudes in the deep ocean: Exp. 2 is more saline than

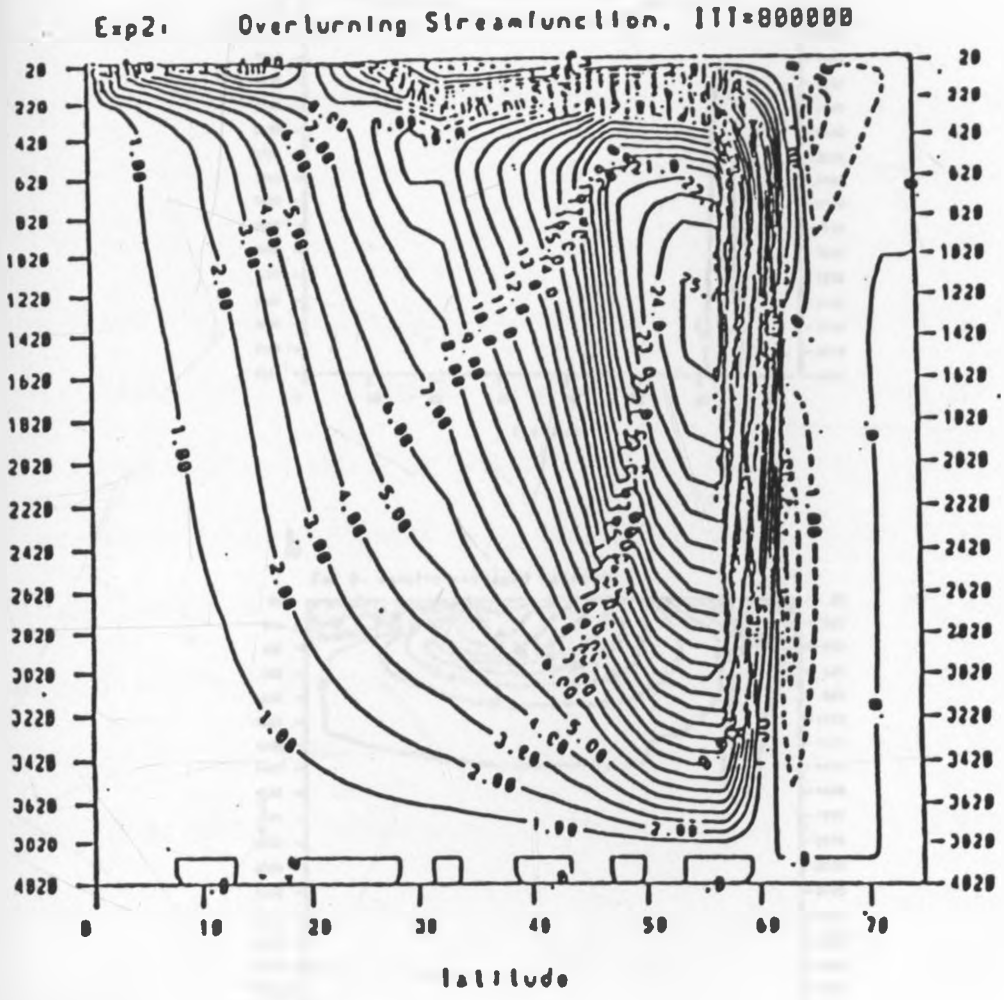

Figure 20: The meridional volume transport for Exp. 2 at equilibrium (Sv). The contour interval is 1 Sv.

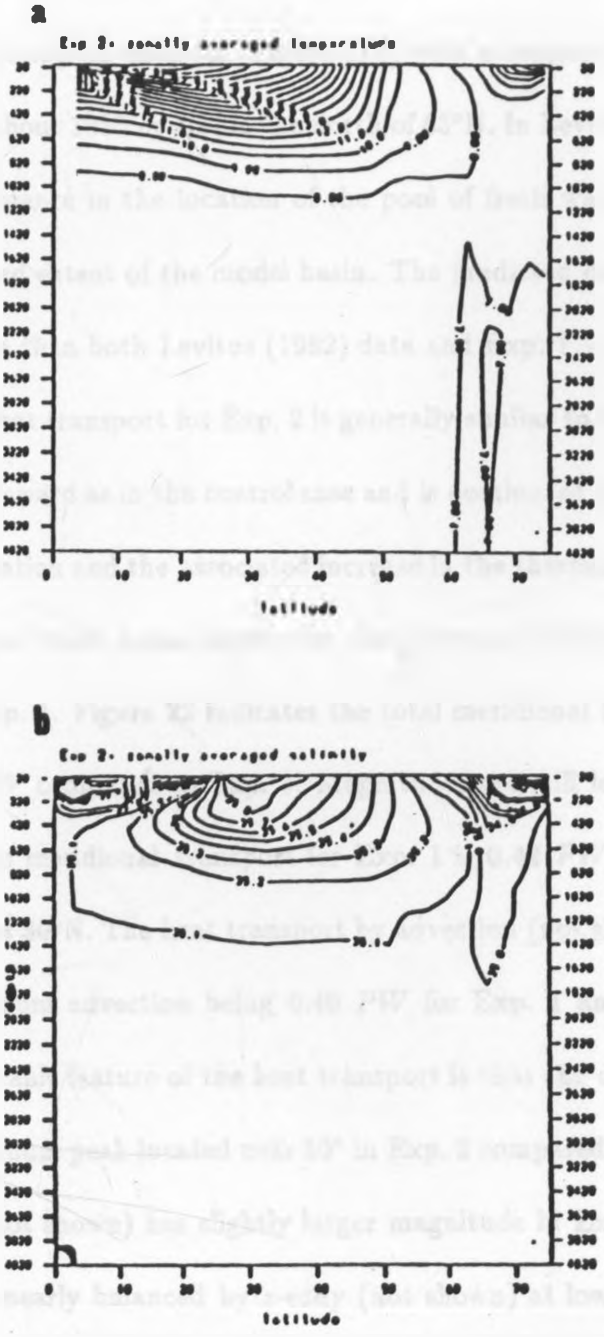

Figure 21: a) Zonally averaged temperature (°C) and b) zonally averaged salinity (*psu*) for Exp. 2 at equilibrium. The contour interval in a) is 1 °*C* and in b) 0.1 *psu*.

Exp. 1; and, at high latitudes, unlike Exp. 1, the salinity structure for Exp. 2 resembles Levitus (1982) climatological data (cf. Figure 11*d*) with a tongue of fresh water extending from the surface to about 1820 *m* just to the north of 65°N. In Levitus this feature is located near 75°N. The difference in the location of the pool of fresh water may be explained by the smaller northward extent of the model basin. The predicted deep ocean salinity values for Exp. 2 are higher than both Levitus (1982) data and Exp. 1

The pattern of heat transport for Exp. 2 is generally similar to that of Exp. 1. The total heat transport is poleward as in the control case and is dominated by advection. The higher rate of NADW formation and the associated increase in the thermohaline component of the Gulf Stream transport leads to an increase in the poleward transport of heat in Exp. 2 in comparison with Exp. 1. Figure 22 indicates the total meridional heat transport in Exp. 2 of more than 0.1 *PW* compared to Exp. 1. Magnitudes are still less than one half of that observed. Maximum meridional transport for Exp. 1 is 0.42 *PW* at 40°N while that for Exp. 2 is 0.53 *PW* at 30°N. The heat transport by advection (not shown) is larger in Exp. 2 than Exp. 1, maximum advection being 0.40 *PW* for Exp. 1 and 0.56 *PW* for Exp. 2, both at 17°N. A notable feature of the heat transport is that the diffusive component (not shown) has its maximum peak located near 50° in Exp. 2 compared with near 65° in Exp. 1. Ekman transport (not shown) has slightly larger magnitude in Exp. 2 than in Exp. 1 and as in the control is nearly balanced by z-eddy (not shown) at low latitudes. z-mean (not shown), like in Exp. 1, is small in magnitude.

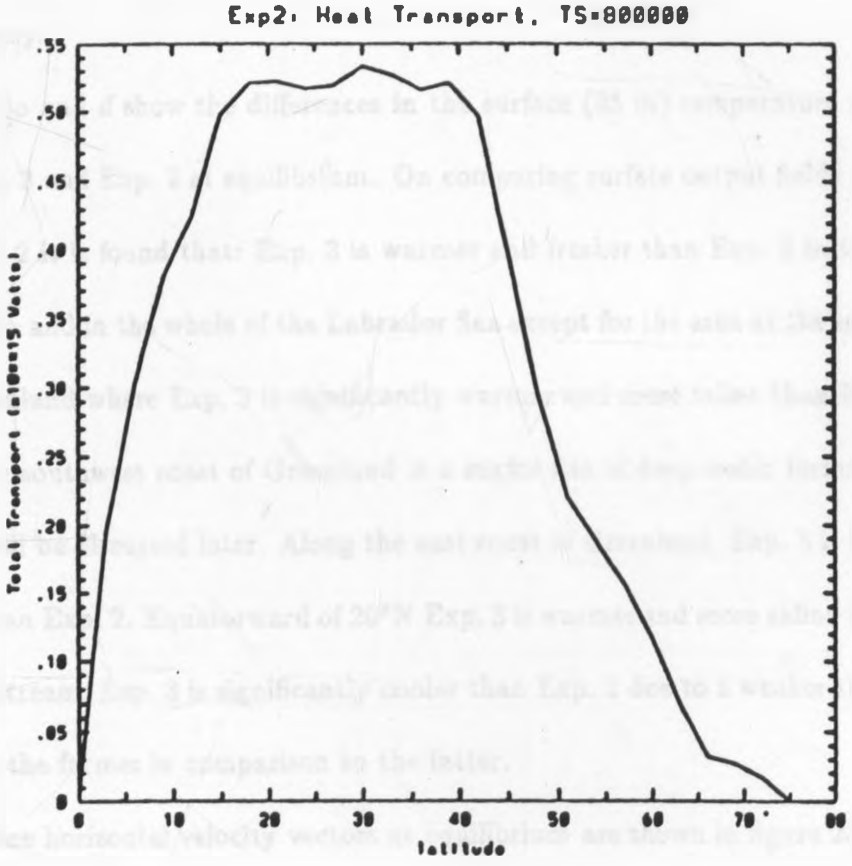

Figure 22: Total meridional heat transport for Exp. 2 at equilibrium in PetaWatts (1 PW = 10^{15} W).

4.2.3 Experiment 3.

This model run was similar to Exp. 2 except that the Arctic fresh water flux was doubled to 0.2 Sv and the tracer time step halved to 0.5 days. In this section comparisons are made between the output fields of Exp. 3 and Exp. 2. Comparisons with Exp. 1 are made only where necessary.

Figures 23*a* and *d* show the differences in the surface (25 m) temperature and salinity fields for Exp. 3 and Exp. 2 at equilibrium. On comparing surface output fields of Exp. 3 to those of Exp. 2 it is found that: Exp. 3 is warmer and fresher than Exp. 2 in the northern Greenland Sea and in the whole of the Labrador Sea except for the area at the southwestern coast of Greenland where Exp. 3 is significantly warmer and more saline than Exp. 2. This region, at the southwest coast of Greenland is a major site of deep water formation in this solution as will be discussed later. Along the east coast of Greenland, Exp. 3 is both fresher and cooler than Exp. 2. Equatorward of 20°N Exp. 3 is warmer and more saline than Exp. 2. In the Gulf Stream, Exp. 3 is significantly cooler than Exp. 2 due to a weaker thermohaline ciculation in the former in comparison to the latter.

The surface horizontal velocity vectors at equilibrium are shown in figure 23c. The flow patterns for Exp. 3 and Exp. 2 are basically similar except for the area in the northern Gulf Stream near 50° where the cyclonic pattern is more pronounced in Exp. 3 than Exp. 2; this is a region of deep water formation in this solution. Magnitudes are relatively higher in Exp. 3 than Exp. 1, the maximum flow being approximately 28 cms^{-1}, which is about 6 cms^{-1} more than Exp. 1, but much lower than Exp. 2. This is consistent with the decrease in the NADW formation rate between Exp. 2 and Exp. 3 as will be discussed later.

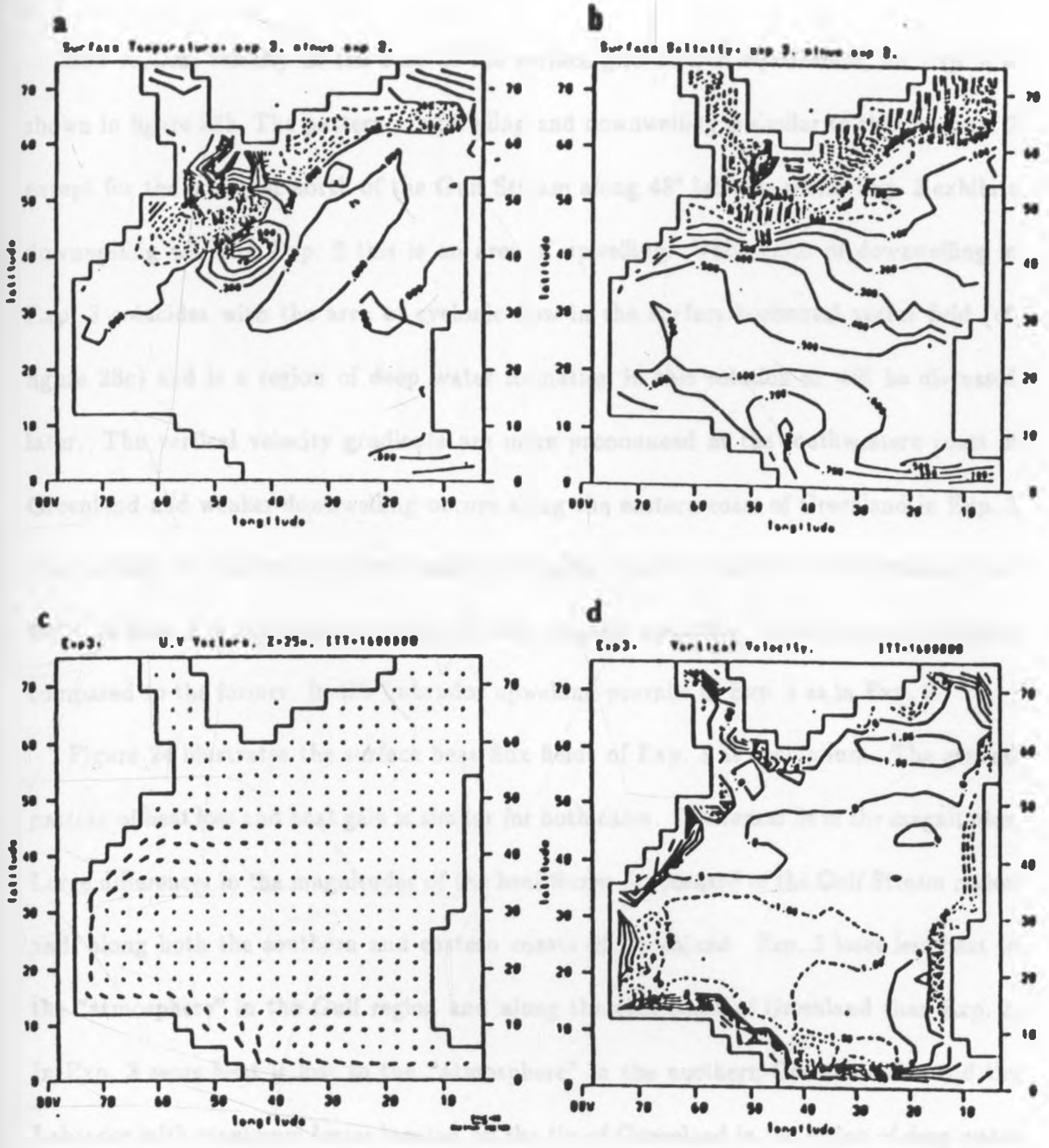

Figure 23: a) Temperature (°C) and b) salinity (psu) differences between Exp. 3. and Exp. 2. (Exp. 3 - Exp. 2) at the surface ($z = 25\ m$), c) horizontal velocity vectors (cms^{-1}) for Exp. 3 at $z = 25\ m$ and d) vertical velocity ($10^{-4}\ cms^{-1}$) for Exp. 3 at $z = 50\ m$. The contour interval in a) 0.3 $°C$, in b) 0.1 psu and in d) $1 \times 10^{-4}\ cms^{-1}$. The maximum vector in c) is 27.6 cms^{-1}.

The vertical velocity at the base of the surface grid box, at equilibrium, for Exp. 3 is shown in figure 23*b*. The pattern of upwelling and downwelling is similar to that for Exp. 2 except for the area just north of the Gulf Stream along 48° latitude where Exp. 3 exhibits downwelling while in Exp. 2 this is an area of upwelling. This region of downwelling in Exp. 3 coincides with the area of cyclonic flow in the surface horizontal vector field (cf. figure 23*c*) and is a region of deep water formation in this solution as will be discussed later. The vertical velocity gradients are more pronounced at the southwestern coast of Greenland and weaker downwelling occurs along the eastern coast of Greenland in Exp. 3 than in Exp. 2. The region of downwelling along the eastern boundary of the domain, near 60°N, in Exp. 2 is also evident in Exp. 3 with stronger upwelling to the north in the latter compared to the former. In the Labrador upwelling prevails in Exp. 3 as in Exp. 2.

Figure 24 illustrates the surface heat flux fields of Exp. 3 at equilibrium. The general pattern of heat loss and heat gain is similar for both cases. Differences lie in the magnitudes. Large differences in the magnitudes of the heat fluxes are located in the Gulf Stream region and, along both the southern and eastern coasts of Greenland. Exp. 3 loses less heat to the "atmosphere" in the Gulf region and along the east coast of Greenland than Exp. 2. In Exp. 3 more heat is lost to the "atmosphere" in the northern Greenland Sea and the Labrador with maximum losses located off the tip of Greenland in the region of deep water formation. This again is due to the more intense thermohaline ciculation in in Exp. 2 than in Exp. 3.

At 450 m, as in Exp. 2 at equilibrium, both the temperature and the salinity fields for Exp. 3 have lost most of the complicated structure of the surface pattern and exhibit

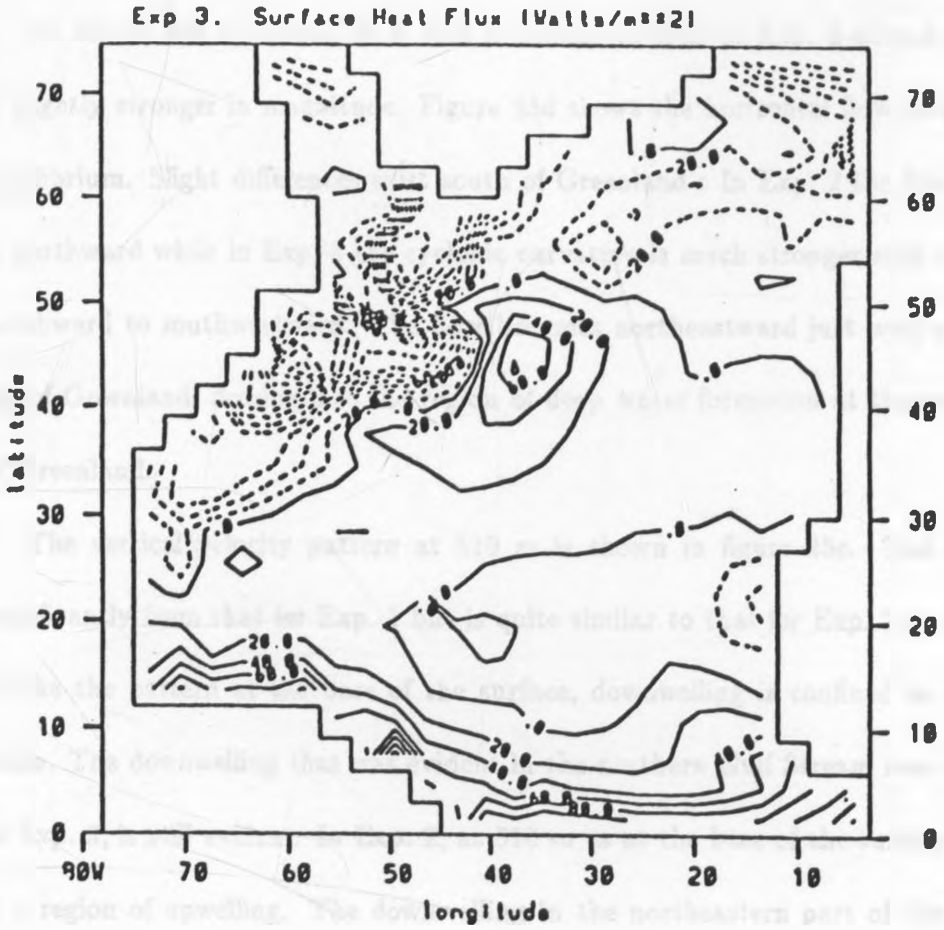

Figure 24: Surface heat flux (Wm^{-2}) at the equilibrium state of Exp. 3. The contour interval is 20 Wm^{-2}.

features of the wind-driven sub-tropical gyre. Figures 25*a* – *b* show the temperature and salinity differences between Exp. 3 and Exp. 2 at 450 *m* at equilibrium. Exp. 3 is warmer and more saline than Exp. 2 everywhere except south of Greenland and along the western boundary near 48° latitude, where it is warmer and fresher and in the northern Gulf Stream at about 45°N, 55°W where it is cooler and fresher.

At 450 *m* the horizontal flow field is similar to that of Exp. 2 at the same level but is slightly stronger in magnitude. Figure 25*d* shows the horizontal flow field for Exp. 3 at equilibrium. Slight differences exist south of Greenland : In Exp. 2 the flow in this region is northward while in Exp. 3 the cyclonic curvature is much stronger such that the flow is northward to southwestward. The flow becomes northeastward just west of the southern tip of Greenland, flowing into the region of deep water formation at the southwestern tip of Greenland.

The vertical velocity pattern at 510 *m* is shown in figure 25c. The pattern differs significantly from that for Exp. 1 but is quite similar to that for Exp. 2 at the same level. Unlike the pattern at the base of the surface, downwelling is confined to three localised areas. The downwelling that was evident in the northern Gulf Stream near 48°N, at 50 *m* in Exp. 3, is still evident. In Exp. 2, at 510 *m* as at the base of the surface grid box, this is a region of upwelling. The downwelling in the northeastern part of the domain along the eastern boundary persists even at this level but now, as in Exp. 2 it extends to the northern boundary. As in Exp. 2, Exp. 3 exhibits upwelling in the western Labrador Sea and weak downwelling along the west coast of Greenland. This is a complete reversal of the configuration at the surface where upwelling is along the west coast of Greenland while the

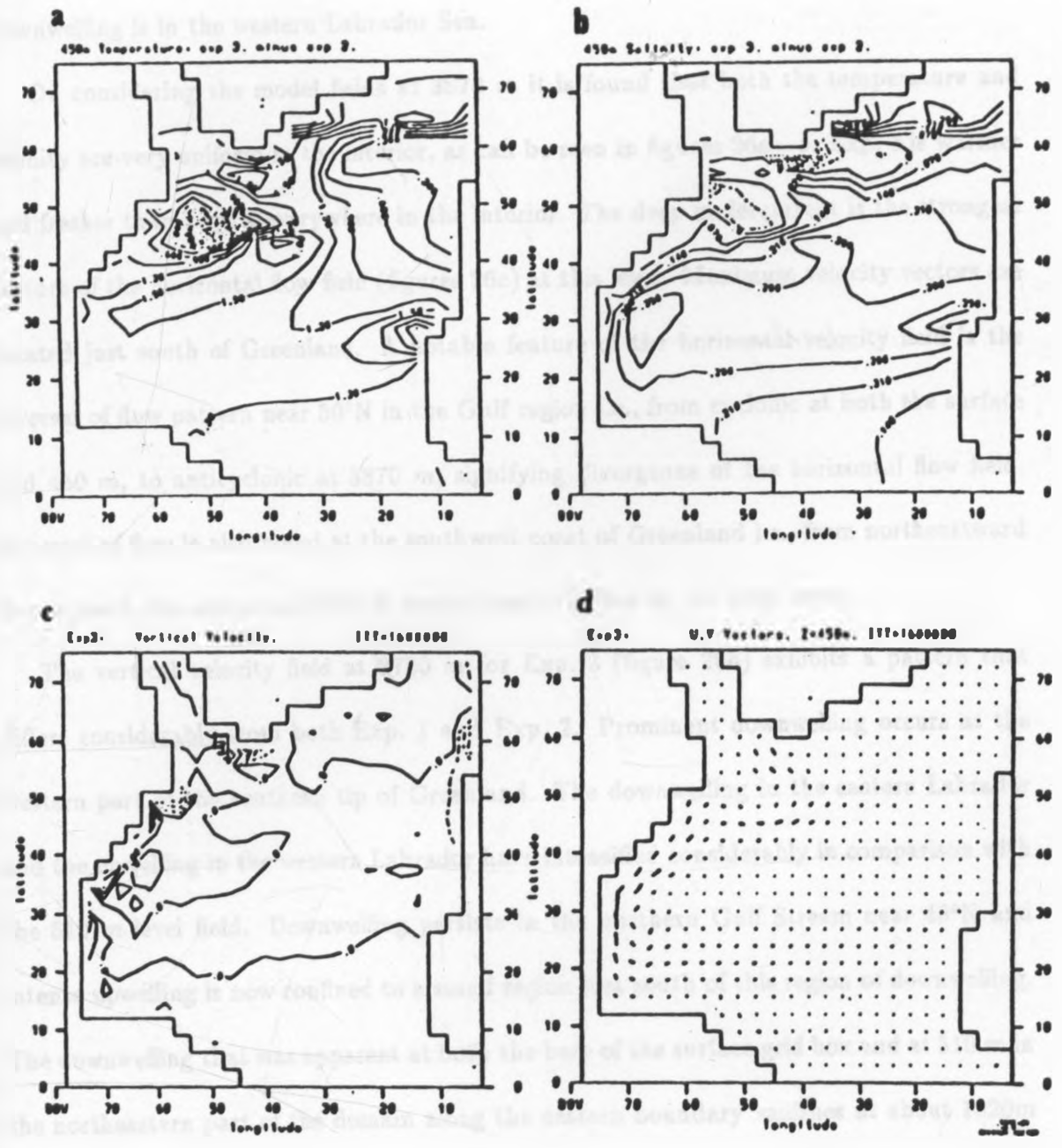

Figure 25: a) Temperature (°C) and b) salinity (*psu*) differences between Exp. 3 and Exp. 2 (Exp. 3-Exp. 2) at 450 *m*, c) vertical velocity (10^{-4} cms^{-1}) for Exp. 3 at 510 *m*, and d) horizontal velocity vectors (cms^{-1}) for Exp. 3 at 450 *m*. The contour interval in a) is 0.3 °*C*, in b) 0.07 *psu*, in c) 7×10^{-4} cms^{-1}. The maximum vector in d) is 9.8 cms^{-1}.

downwelling is in the western Labrador Sea.

On considering the model fields at 3870 m it is found that both the temperature and salinity are very uniform in the interior, as can be seen in figures 26a – b. Exp. 3 is warmer and fresher than Exp. 2 everywhere in the interior. The deep undercurrent is the strongest feature of the horizontal flow field (figures 26c) at this level. Maximum velocity vectors are located just south of Greenland. A notable feature of the horizontal velocity field is the reversal of flow pattern near 50°N in the Gulf region i.e., from cyclonic at both the surface and 450 m, to anticyclonic at 3870 m, signifying divergence of the horizontal flow field. Reversal of flow is also noted at the southwest coast of Greenland i.e., from northeastward flow at both the surface and 450 m to northeasterly flow in the deep ocean.

The vertical velocity field at 3720 m for Exp. 3 (figure 26d) exhibits a pattern that differs considerably from both Exp. 1 and Exp. 2. Prominent downwelling occurs at the western part of the southern tip of Greenland. The downwelling in the eastern Labrador and the upwelling in the western Labrador have intensified considerably in comparison with the 510 m level field. Downwelling persists in the northern Gulf Stream near 48°N and intense upwelling is now confined to a small region just south of this region of downwelling. The downwelling that was apparent at both the base of the surface grid box and at 510 m in the northeastern part of the domain along the eastern boundary vanishes at about 1320m as in Exp 1.

Figures 27a – b illustrate the zonally averaged temperature and salinity structures for Exp. 3 at equilibrium. The thermocline is diffuse like in Exp. 2. Figures 27c – d show the differences in the temperature and salinity structures of Exp. 3 and Exp. 2. Exp. 3

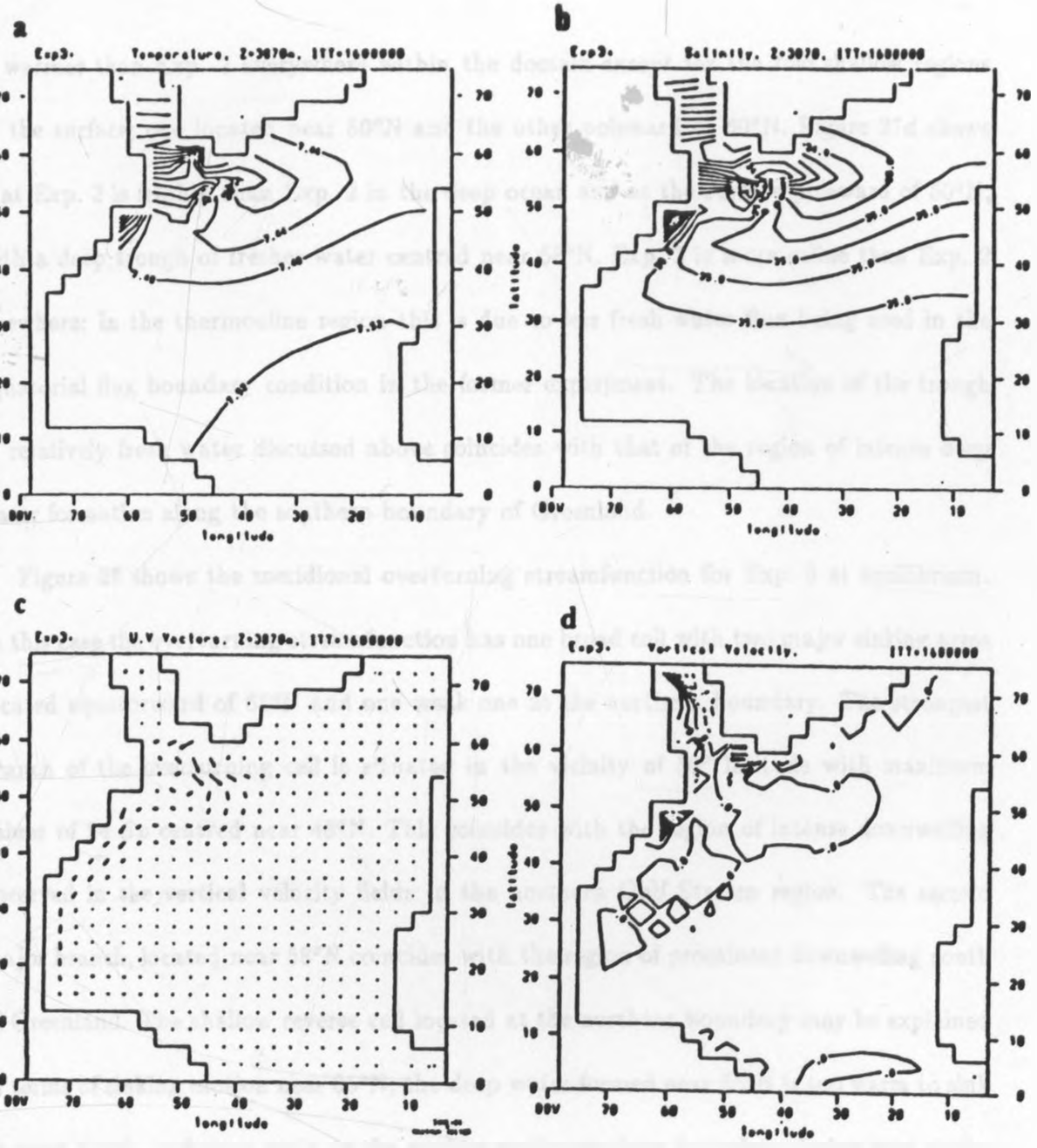

Figure 26: Exp. 3 a) Temperature (°C) at 3870 m, b) salinity (psu) at 3870 m, c) horizontal velocity vectors (cms^{-1}) at 3870m and d) vertical velocity (10^{-4} cms^{-1}) at 3720 m. The contour interval in a) is 0.04 $°C$, in d) 3×10^{-4} cms^{-1}. The maximum vector in c) is 3.3 cms^{-1}.

is warmer than Exp. 2 everywhere within the domain except for the two shallow regions at the surface; one located near 50°N and the other poleward of 60°N. Figure 27*d* shows that Exp. 3 is fresher than Exp. 2 in the deep ocean and at the surface poleward of 50°N, with a deep trough of fresher water centred near 58°N. Exp. 3 is more saline than Exp. 2 elsewhere; In the thermocline region this is due to less fresh water flux being used in the equatorial flux boundary condition in the former experiment. The location of the trough of relatively fresh water discussed above coincides with that of the region of intense deep water formation along the southern boundary of Greenland.

Figure 28 shows the meridional overturning streamfunction for Exp. 3 at equilibrium. In this case the overturning streamfunction has one broad cell with two major sinking arms located equatorward of 65°N and one weak one at the northern boundary. The strongest branch of the overturning cell is situated in the vicinity of 50° latitude with maximum values of 24 *Sv* centred near 48°N. This coincides with the region of intense downwelling observed in the vertical velocity fields in the northern Gulf Stream region. The second major branch, located near 58°N coincides with the region of prominent downwelling south of Greenland. The shallow reverse cell located at the northern boundary may be explained in terms of sinking motion near 65°N; the deep water formed near 65°N is too warm to sink to great depth, and rises again to the surface at the northern boundary, losing heat to the "atmosphere". The pattern of Φ differs significantly from both Exp. 1 and Exp. 2 north of the respective regions of downwelling.

Doubling the Arctic freshening leads to the formation of a fresh water lid that extends more to the south in Exp. 3 compared to Exp. 2. As a consequence deep water forms more

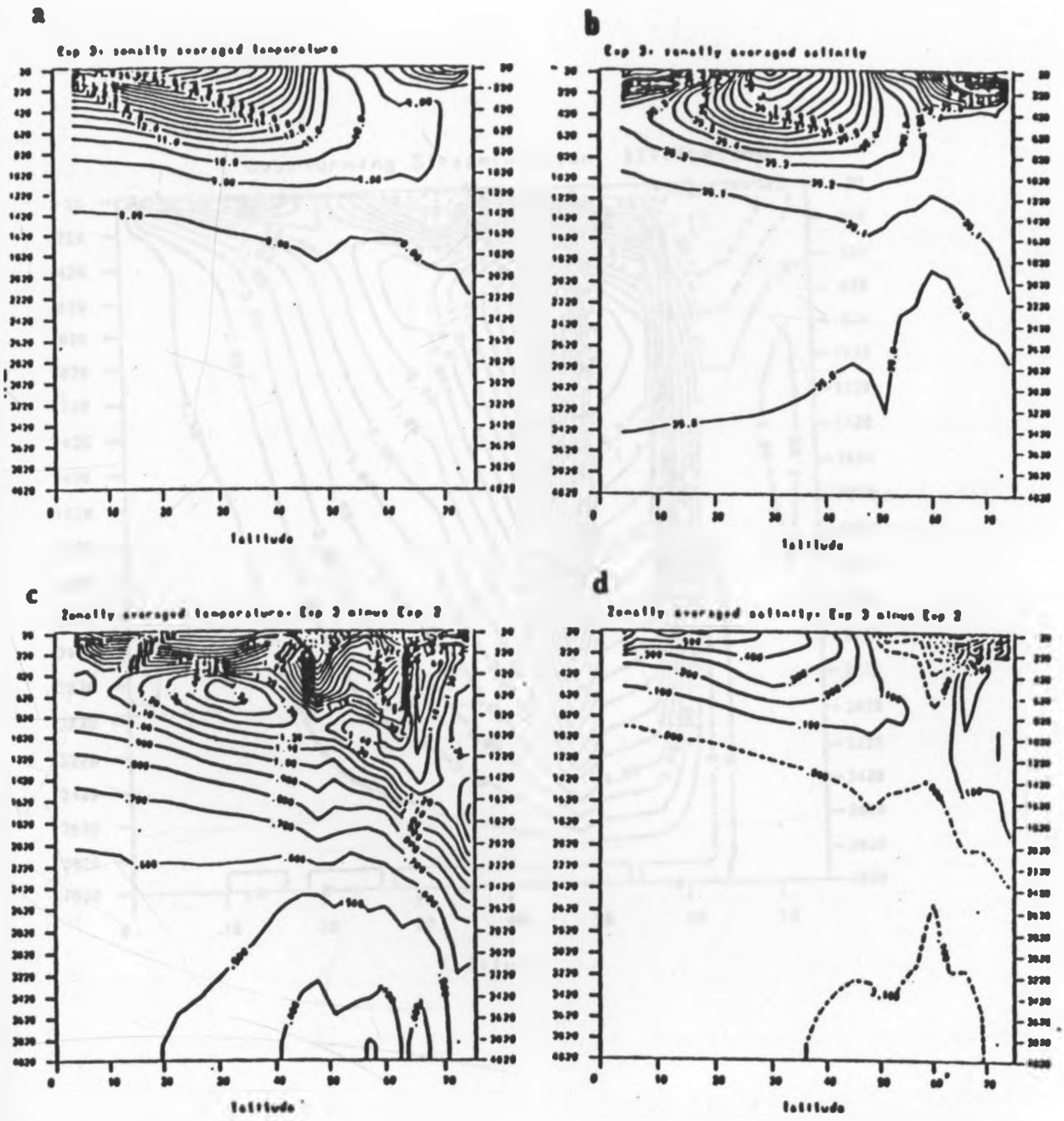

Figure 27: a) Zonally averaged temperature (°*C*) and b) zonally averaged salinity (*psu*) as functions of depth for the equilibrium state of Exp. 3; and, differences in the above structures for c) temperature (°*C*) and d) salinity (*psu*) between Exp. 3 and Exp. 2 (Exp. 3-Exp. 2). The contour interval in a) is 1 °*C*, in b) 0.1 *psu*, in c) 0.1 °*C*, in d) 0.1 *psu*.

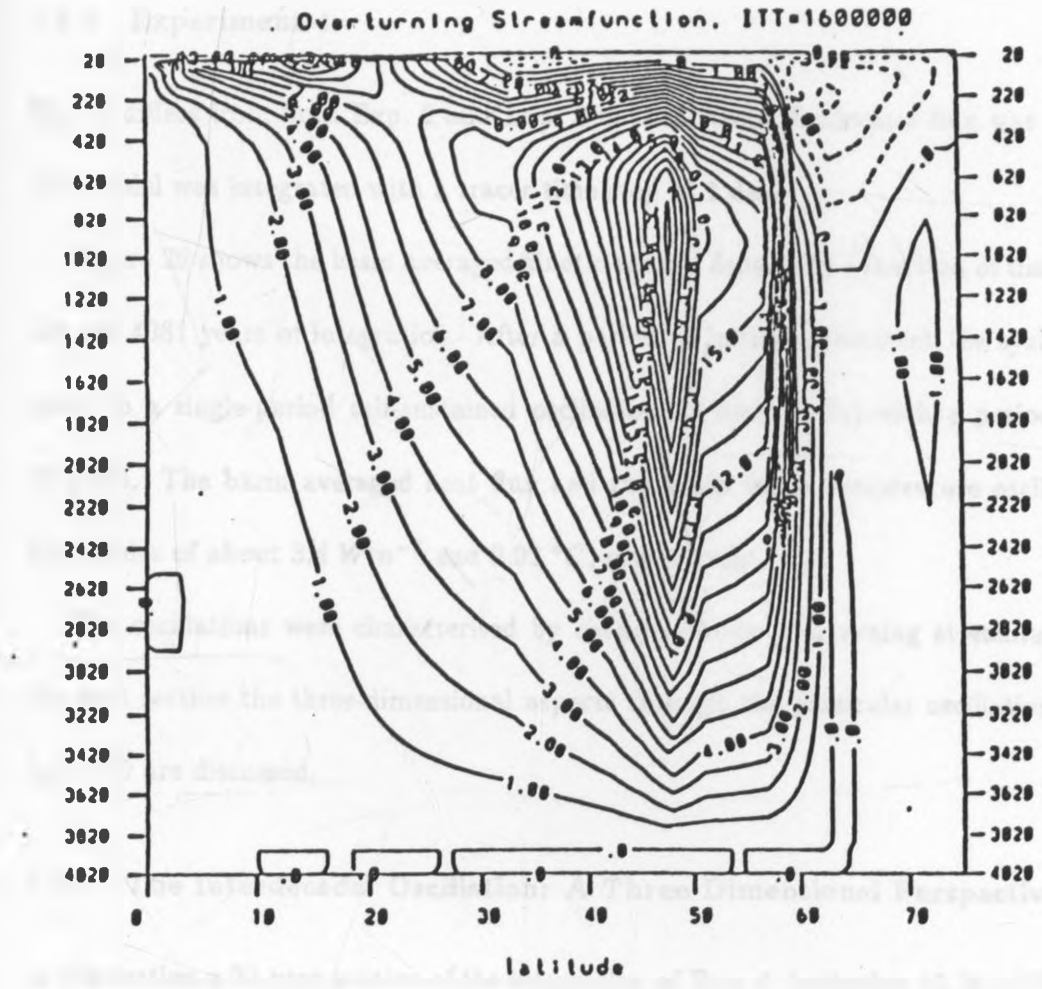

Figure 28: The meridional overturning streamfunction for Exp. 3 at equilibrium (Sv). The contour interval is 1 Sv.

equatorward in Exp. 3 compared to Exp. 2 as can be seen in the plot of the meridional overturning streamfunction.

4.2.4 Experiment 4.

Exp. 4 differs from both Exp. 2 and Exp. 3 in that Arctic freshwater flux was not added. The model was integrated with a tracer time step of 1 day.

Figure 29 shows the basin averaged kinetic energy density as a function of time throughout the 4381 years of integration. After a period of initial adjustment the system settled down to a single-period self-sustained oscillation (a limit cycle) with a period of about 22 years. The basin averaged heat flux and the basin mean temperature oscillated with amplitudes of about 3.4 Wm^{-2} and 0.02 ^{o}C, respectively.

The oscillations were characterised by changes in the overturning streamfunction. In the next section the three-dimensional aspects through the particular oscillation shown in figure 30 are discussed.

4.2.5 The Interdecadal Oscillation: A Three-Dimensional Perspective.

In this section a 22-year portion of the integration of Exp. 4, beginning 12.58×10^5 days into the spin-up is discussed. Since the system is in a limit cycle any randomly chosen period within the cycle is representative of the general oscillation. Figure 31 illustrates the total North Atlantic overturning streamfunction throughout the oscillation.

In the lowest kinetic energy state of the oscillation the meridional overturning circulation consists of three main features as illustrated in figure 31*a*:

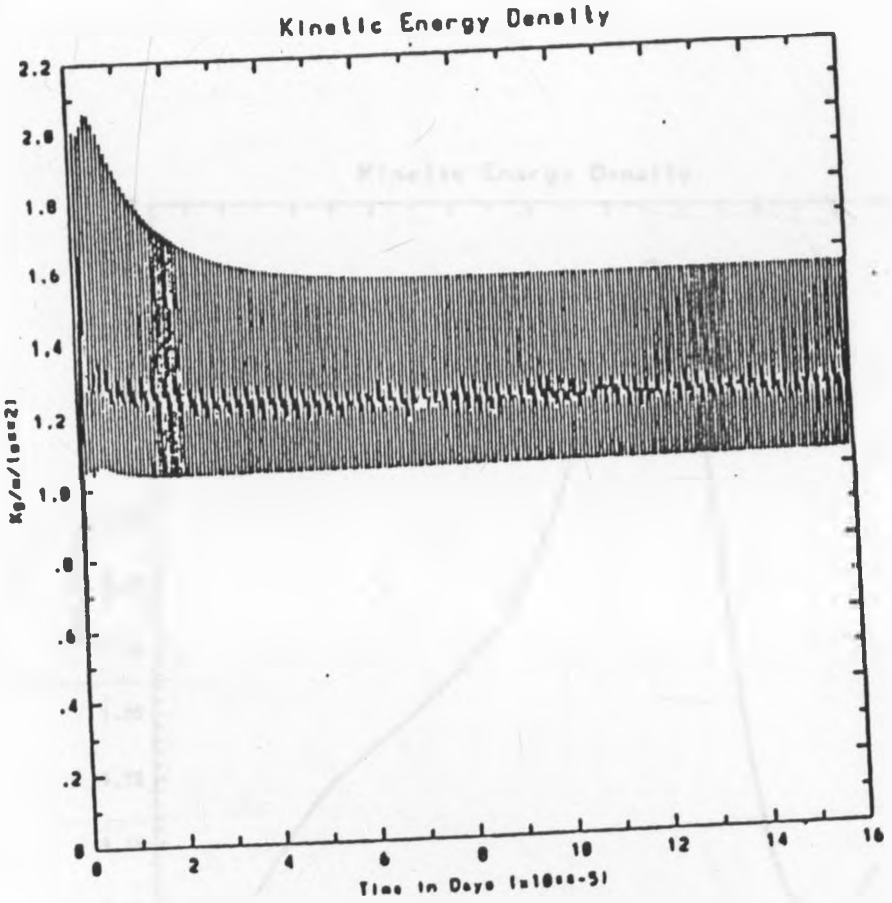

Figure 29: Time series of kinetic energy density ($10^{-1}\ kgm^{-1}s^{-2}$) for Exp. 4 throughout the 4381 years of integration.

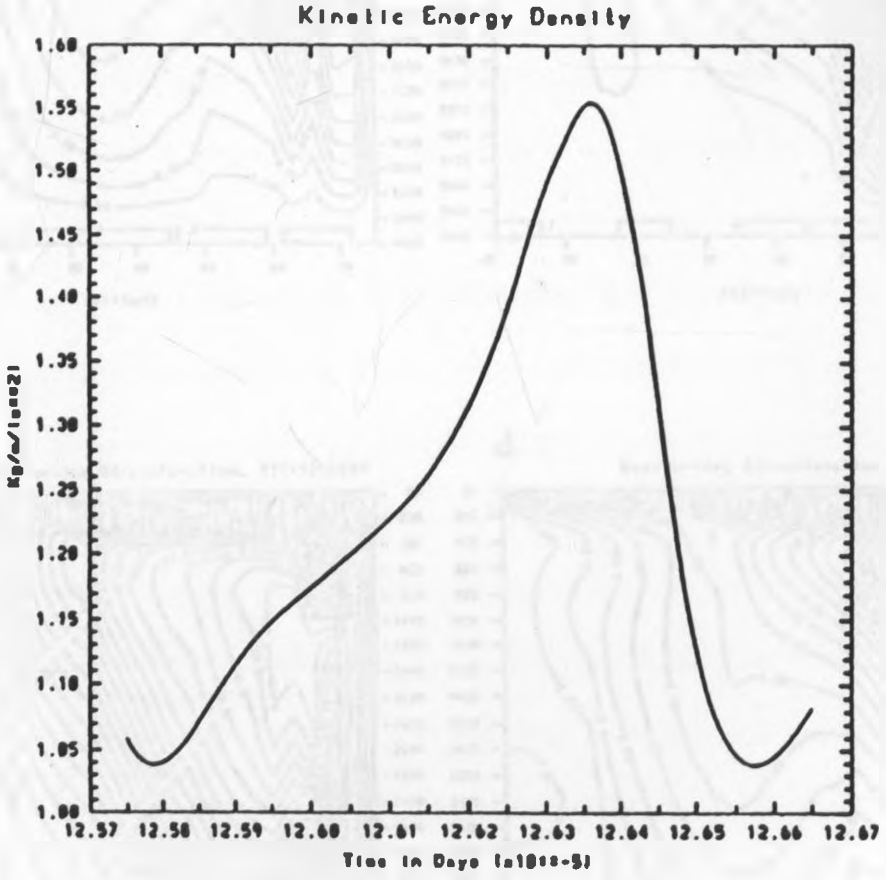

Figure 30: One complete oscillation in the time series of kinetic energy density (cf. Figure 29) for Exp. 4. Units are $10^{-1}\ kgm^{-1}s^{-2}$.

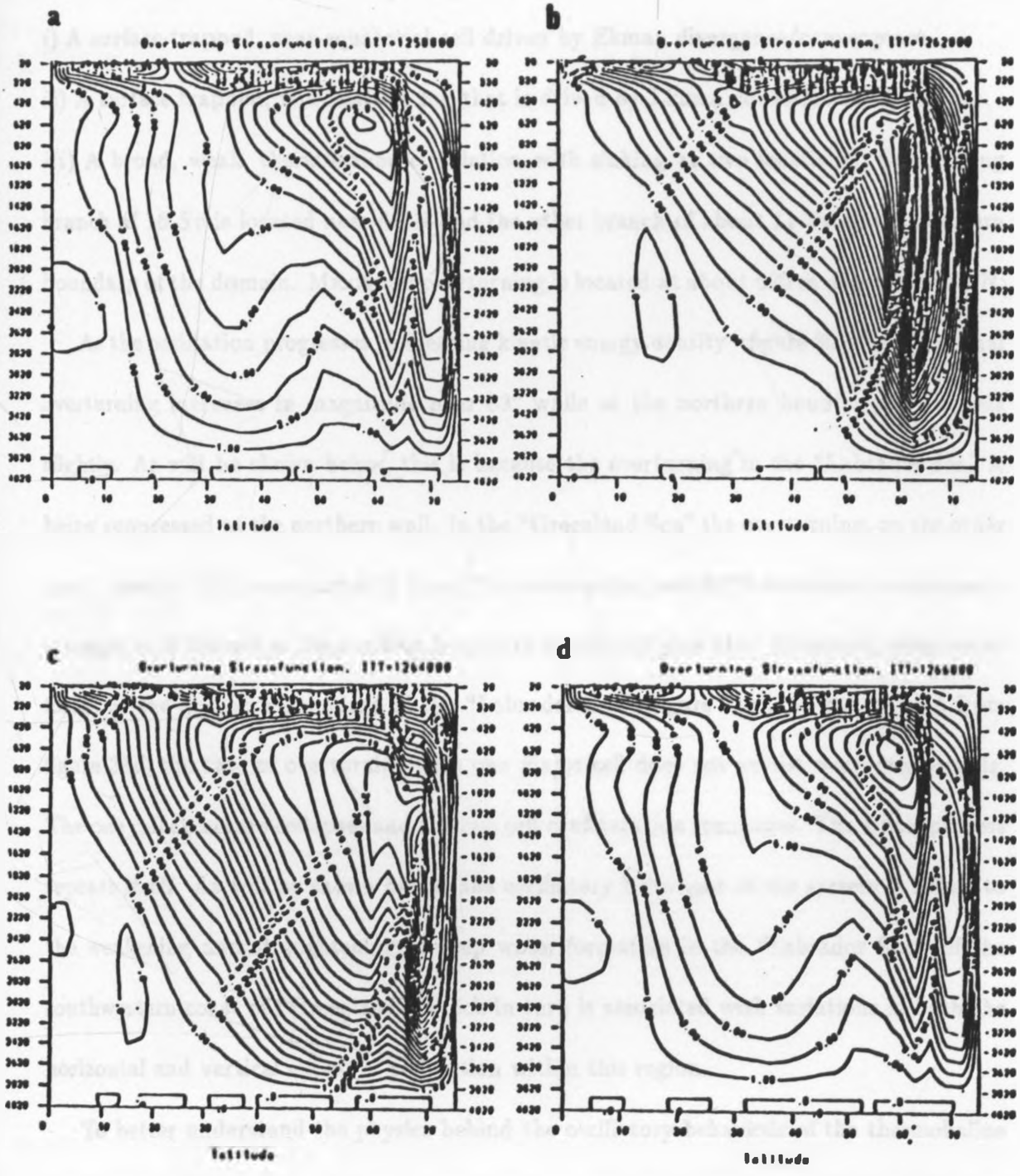

Figure 31: The total North Atlantic meridional overturning streamfunction (Sv) through the oscillation shown in figure 30 starting at year 3444.2 a) day=1258000, b) day=1262000, c) day=1264000 and d) day=1266000. The contour interval is 1 *Sv*.

i) A surface-trapped, near-equatorial cell driven by Ekman divergence/convergence.

ii) A surface-trapped, mid-latitude cell that is driven by Ekman convergence/divergence.

iii) A broad, weak, thermohaline circulation with sinking at two locations. One sinking branch of 16 Sv is located near 63°N and the other branch of about 11 Sv at the northern boundary of the domain. Maximum overturning is located at about 620 m depth near 58°N.

As the oscillation progresses (increasing kinetic energy density - figure 30) the meridional overturning increases in magnitude near 63° while at the northern boundary it weakens slightly. As will be shown below, this is because the overturning in the "Labrador Sea" is being suppressed at the northern wall. In the "Greenland Sea" the overturning, on the other hand, remains fairly constant with time. The overturning near 63°N continues to increase in strength until the cell at the northern boundary vanishes (figure 31*b*). Eventually deep water forms at the northern boundary of the "Labrador Sea" (figure 31*c*). As can be seen from figure 31*d*, the case of overturning with one major cell does not persist over long periods. The one cell structure collapses and the two cell configuration reemerges. The whole process repeats itself. As will be shown below, the oscillatory behaviour of the system is linked to the weakening and strenghtening of deep water formation in the "Labrador Sea" off the southwestern coast of "Greenland", which in turn is associated with variations in both the horizontal and vertical extent of convection within this region.

To better understand the physics behind the oscillatory behaviour of the thermohaline ciculation in this solution, a three-dimensional perspective through a particular oscillation is presented. Figure 32 illustrates a close-up of the meridional overturning in the "Labrador Sea", corresponding to figures 31a, b, c, d, respectively. Figures 33 and 34 show meridional

cross-sections of temperature and salinity (taken at one grid box off the western boundary, all along the coast), while figure 35 shows horizontal temperature sections at 64.5° latitude. Figure 36 illustrates horizontal velocity vectors at 750 m and the vertical velocity at 840 m; these figures correspond to figures 32a, c i.e., respresenting the weak and strong phases of the oscillation, respectively.

The interdecadal oscillations in this experiment are controlled by the structure of surface freshwater flux forcing field. Important for the oscillations are the local evaporation maxima at high latitudes in both the "Greenland Sea" and the "Labrador Sea". Oscillations occur in both the "Greenland" and "Labrador Seas"; the oscillations in the former region are much weaker than those in the latter, and the discussion is confined to the interdecadal variability in the "Labrador Sea" and hence to the local $E - P$ maximum located off the southwestern coast of "Greenland".

The discussion starts at the stage of the oscillation when meridional overturning in the "Labrador" is weak (figure 32a) and the system is least energetic (figure 30). At this stage in the oscillation thermally-driven convection is occuring, to great depth, all across the "Labrador Sea", as can be inferred from the near-vertical profiles of both the isotherms isohalines in this region (figures 33a, 34a, 35a). Consequently, the east-west pressure gradient in the "Labrador Sea" is weak and so, through geostrophy, is the overturning at high latitudes within this region. The north-south surface pressure gradient remains fairly strong, due to the surface boundary conditions, driving zonal flow in the "Labrador Sea". At this stage, deep water forms off the southwestern coast of "Greenland" at about 63°N as well as in the "Greenland Sea" as can be inferred from the plots of both the horizontal velocity at

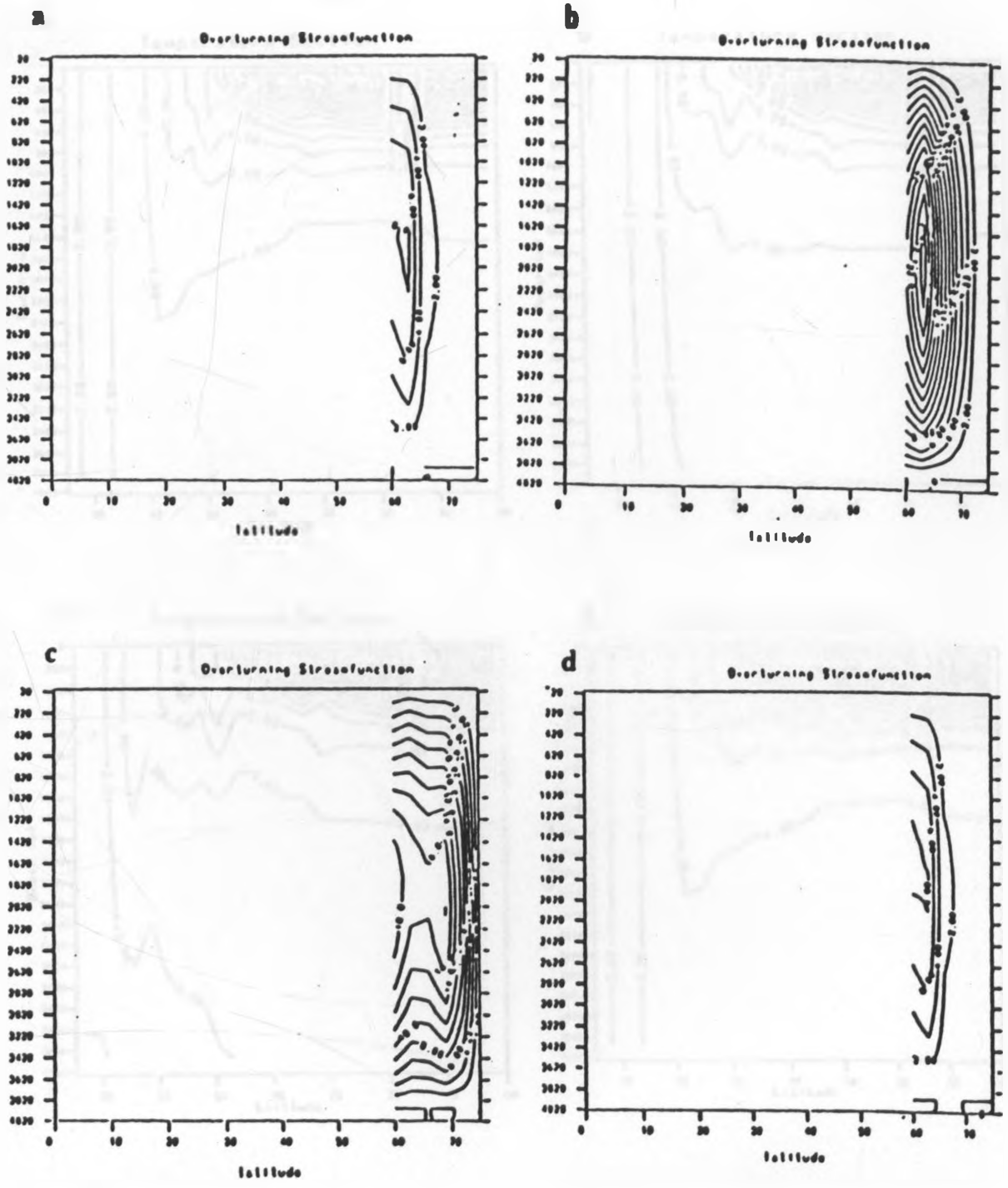

Figure 32: A close-up of the meridional overturning streamfunction (Sv) through the oscillation shown in figure 30 for the "Labrador Sea" at day a) 1258000, b) 1262000, c) 1264000, and d) 1266000. The contour interval is 2 *Sv*.

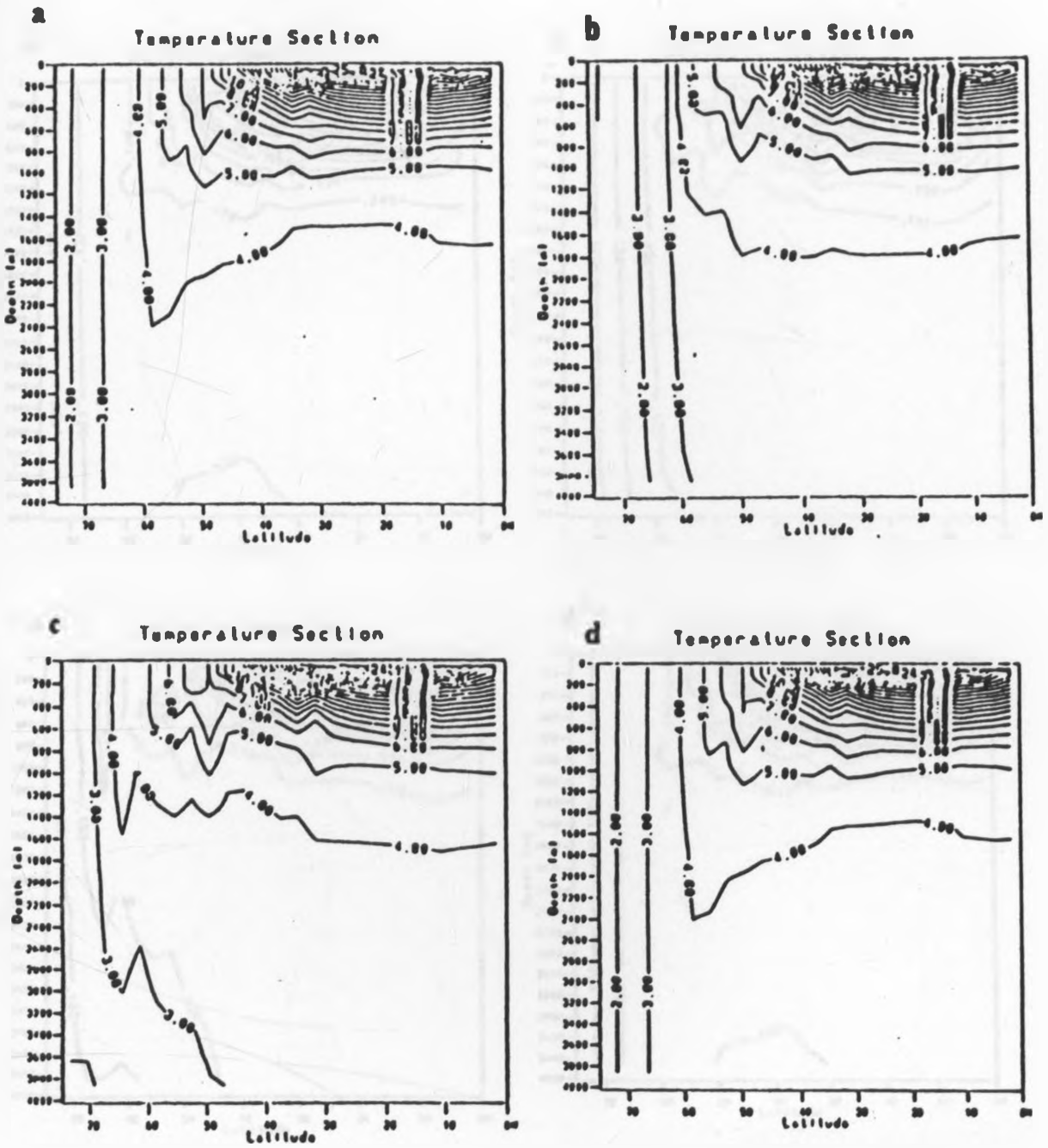

Figure 33: Meridional temperature sections, taken at one grid point off the western boundary of the model domain, corresponding to figure 32 at day a) 1258000, b) 1262000, c) 1264000 and d) 1266000. The contour interval is 1 ^{o}C.

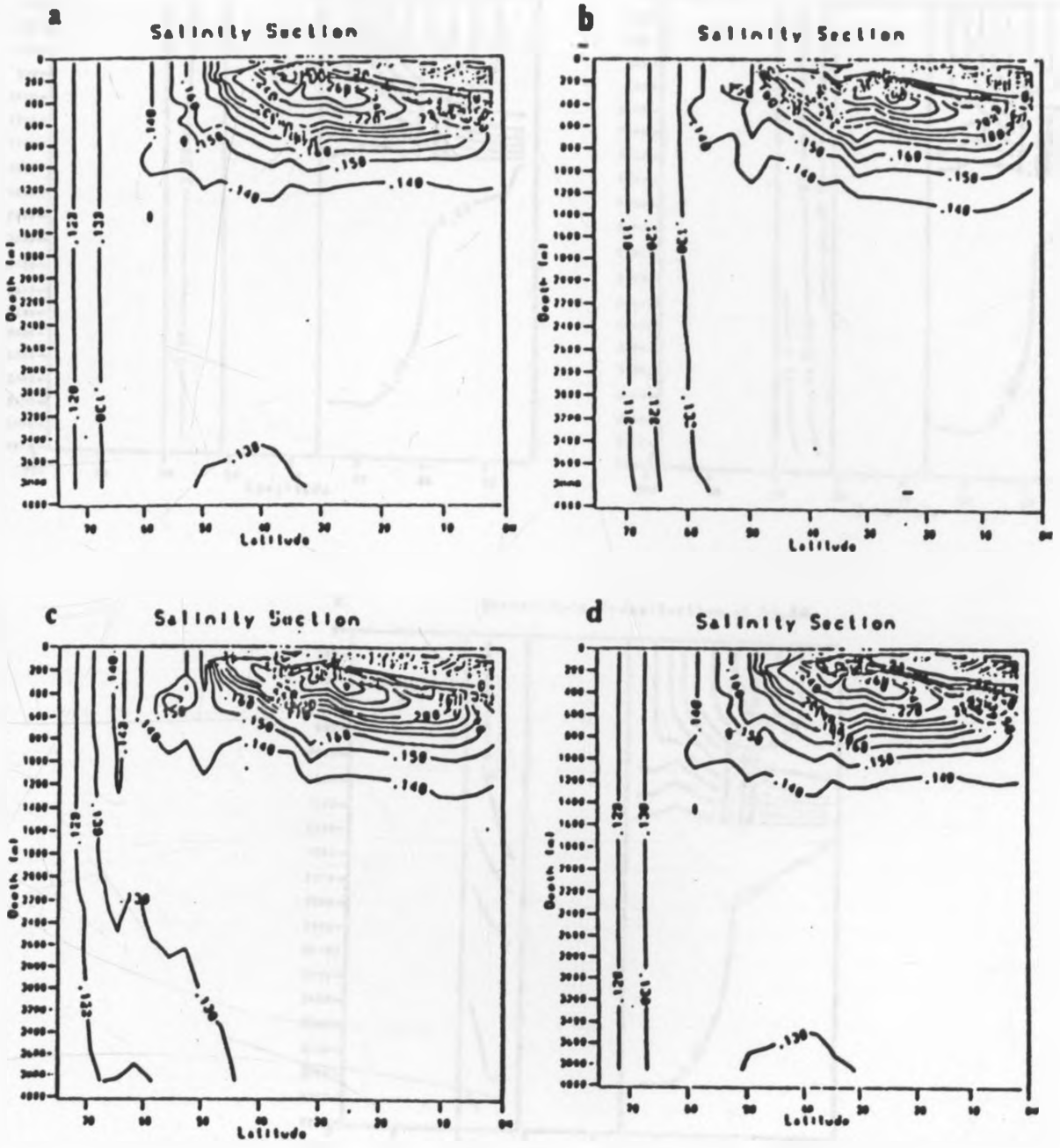

Figure 34: Meridional salinity sections, taken at one grid point off the western boundary of the model domain, corresponding to figure 32 at day a) 1258000, b) 1262000, c) 1264000 and d) 1266000. The contour interval is 0.01 *psu*.

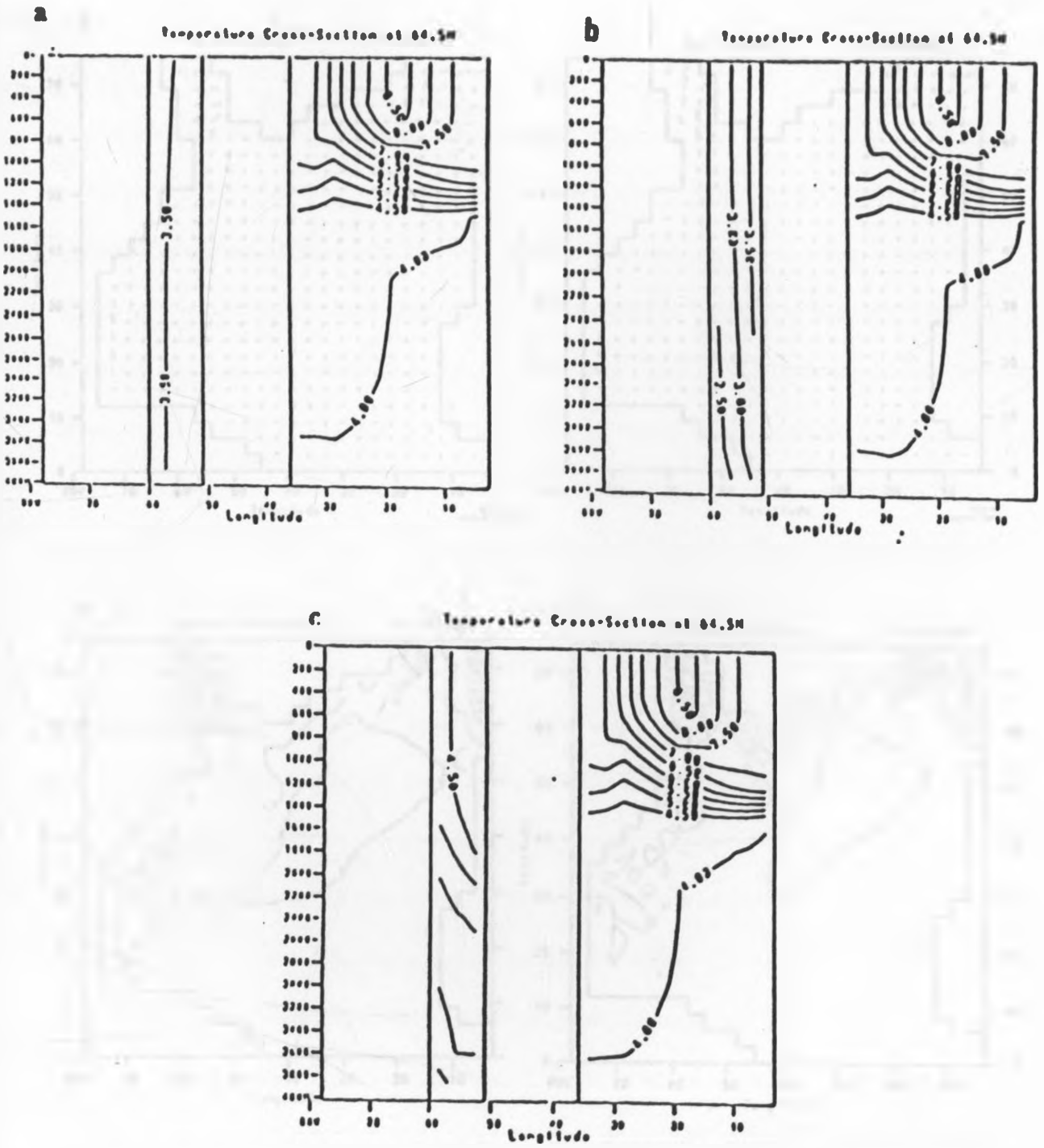

Figure 35: Zonal temperature sections at 64.5°N corresponding to figure 32 at day a) 1258000, b) 1262000 and c) 1264000. The contour interval is 0.5 °C.

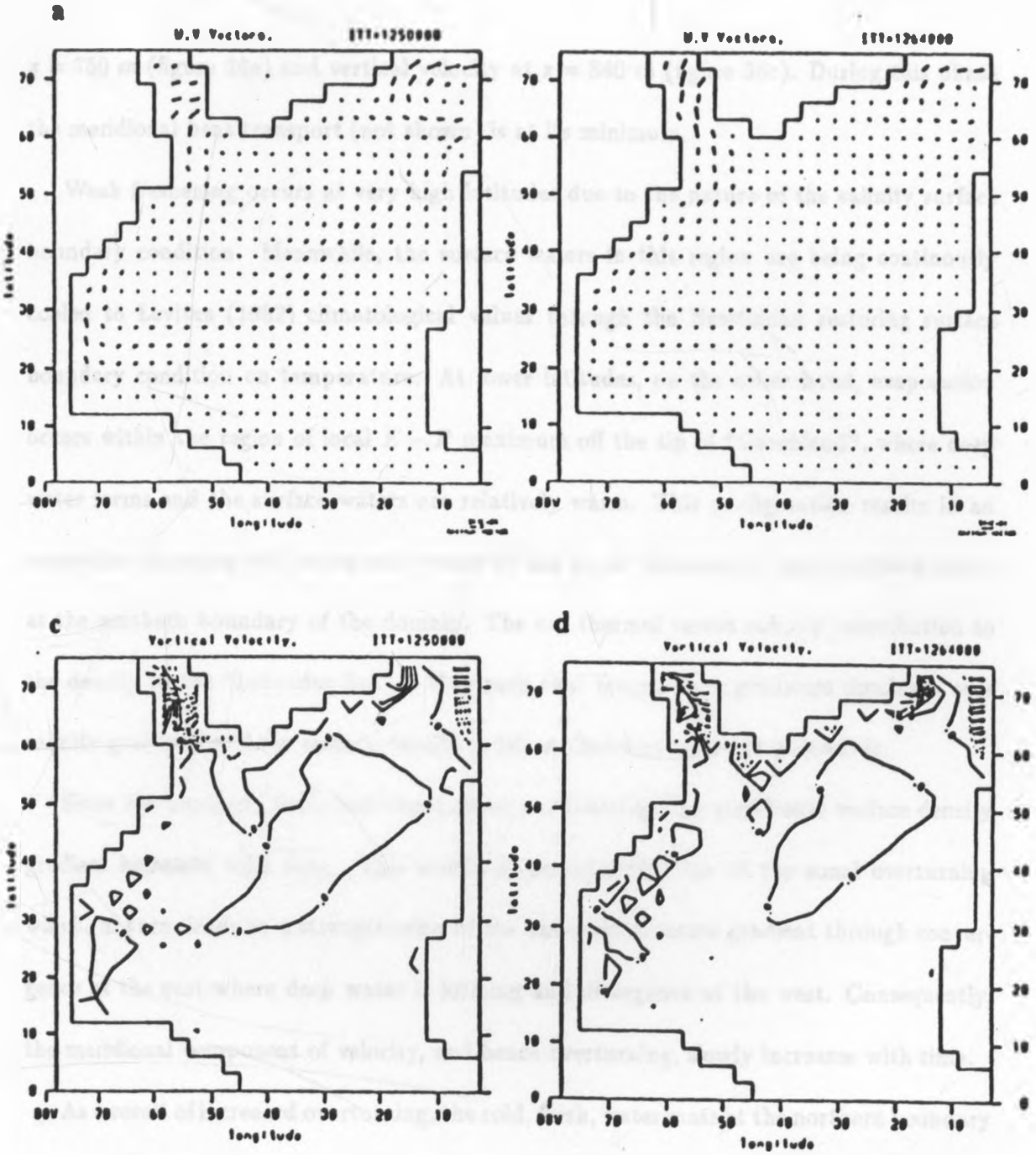

Figure 36: a) Horizontal velocity (cms^{-1}) at 750 m maximum vector of 3.9 cms^{-1}, b) horizontal velocity (cms^{-1}) at 750 m with maximum vector of 5.9 cms^{-1}, c) vertical velocity (10^{-4} cms^{-1}) at 840 m d) vertical velocity (10^{-4} cms^{-1}) at 840 m The maximum vector in a) is 3.9 cms^{-1} and in b) 5.9 cms^{-1}. The contour interval in c) is 20×10^{-4} cms^{-1} and in d) 10×10^{-4} cms^{-1}.

$z = 750\ m$ (figure 36*a*) and vertical velocity at $z = 840\ m$ (figure 36*c*). During this phase the meridional heat transport (not shown) is at its minimum.

Weak freshening occurs at very high latitudes due to the nature of the salinity surface boundary condition. Meanwhile, the surface waters in this region are being continously cooled to Levitus (1982) climatological values through the Newtonian restoring surface boundary condition on temperature. At lower latitudes, on the other hand, evaporation occurs within the region of local $E - P$ maximum off the tip of "Greenland", where deep water forms and the surface waters are relatively warm. This configuration results in an anomalous situation with warm salty water off the tip of "Greenland" and cold fresh water at the northern boundary of the domain. The net thermal versus salinity contribution to the density in the "Labrador Sea" is thus such that temperature gradients dominate over salinity gradients and the surface density gradient therefore increases polewards.

Since the processes described above occur continuously, the meridional surface density gradient increases with time. This results in an intensification of the zonal overturning which, in turn, leads to a strengthening of the east-west pressure gradient through convergence at the east where deep water is forming and divergence at the west. Consequently, the meridional component of velocity, and hence overturning, slowly increases with time.

As a result of increased overturning, the cold, fresh, water mass at the northern boundary is slowly pushed equatorward at depth, suppressing deep convection from below, as it moves under the warm water mass, starting from the western boundary (cf. figures 33*b*, 34*b*, 35*b*). This acts as a feedback mechanism, strenghthening the zonal pressure gradient and hence the meridional overturning (figure 32*b*).

As convection begins to shut off in the west the overturning starts to increase. Once convection is shut off, the overturning rapidly increases and the cold, fresh, water mass is advected equatorward at depth and replaced by warm, salty, thermocline waters from the south. Overturning now occurs at the northen boundary (cf. figure 31*c*, 32*c*); this can also be inferred from the plots of both the horizontal velocity (figure 36*b*) and vertical velocity (figure 36*d*). At this point in the integration the western boundary current extends into the region of deep water formation at the northern boundary of the domain. Associated with this phase is a increase of 0.3 PW in meridional heat transport compared to the phase of minimum kinetic energy.

As the warm watermass sinks to the bottom convection commmences again, continuing until it becomes widespread once more, occuring all across the basin, reducing the east-west pressure gradient. The whole process begins anew.

The time scale associated with the interdecadal variability can be estimated as follows:
i) Cooling of the "Labrador Sea" - During the weak phase convection in the "Labrador Sea" occurs to the bottom of the basin. The diffusive time scale associated with this phase is given by $H^2/A_{TV} \approx 0.5\ years$ for $H = 4020\ m$ and $A_{TV} = 10^4\ cms^{-1}$. This is equivalent to restoring the 4020 m deep basin to Levitus T^* with (cf. equation 5) an e-folding time scale of 11 years.
ii) Set up of "Labrador Sea" zonal overturning - As the northern "Labrador Sea" cools, the net meridional surface density gradient increases, as discussed above, and consequently the zonal overturning increases, leading to an enhanced zonal pressure gradient, which in turn results in an increase in the meridional overturning. The time scale for the zonal overturning

in the "Labrador Sea" is about 4 years, assuming a surface current of 10 cms^{-1}, a deep return flow of 1 cms^{-1} and vertical velocities of order 0.01 cms^{-1}.

iii) Advection of cold, fresh, water in the deep western boundary current - During the intermediate phase of the oscillation, the meridional component of velocity, and hence the overturning, increases slightly due to an enhanced zonal surface pressure gradient. Consequently, the cold, fresh, water mass at the northern boundary is slowly pushed equatorward at depth killing convection from below as it moves under the warm, saline, thermocline water mass. Assuming an advection speed of 2 cms^{-1} over a distance of 600 km, the time scale for the southward advection of the cold, fresh, water mass is about 1 year.

iv) Replacement of the cold, fresh, water mass by the warm, saline, thermocline water mass from the south - Once convection is shut off in the west the overturning rapidly increases and the cold, fresh, water mass is advected equatorward at depth. The time scale associated with the southward advection of the cold, fresh, water mass and its subsequent replacement by the warm, saline, thermocline water mass is about 5 years, assuming a surface flow of 10 cms^{-1}, a deep flow of 3 cms^{-1}, a vertical velocity 10^{-2} cms^{-1} and a horizontal distance of 25°, the latter being the distance from the northern boundary (75°N) to the latitude where the western boundary current separates from the coast (50°N).

Following the above discussion it can be seen that the total time scale associated with the interdecadal oscillations is $\approx$ 21 years. This value compares well with the value of 22 years obtained from the model simulations.

4.2.6 Experiment 5.

Exp. 5 is similar to both Exp. 2 and Exp. 3 except that the Arctic freshwater flux was added to the northernmost grid boxes only in the "Greenland Sea". Further, the model was integrated forward in time for a total period of about 2190 years of tracer time steps in two stages: the first 548 years were run with a 1 day time step and the rest of the integration was carried out with a 0.5 days time step.

This model run exhibited variability similar to that for Exp. 4 on a time scale of about 17 years. It is evident from this run that Arctic freshening in the "Greenland Sea" region does not inhibit interdecadal variability in the model thermohaline circulation.

4.2.7 Experiment 6.

This model run is similar to Exp. 5 except that the Arctic freshening was confined to the two northernmost grid boxes (6°) adjacent to Greenland i.e., in the "East Greenland Current" region of the "Greenland Sea". The integration was carried out for 2190 years of tracer time steps.

This model run again exhibited variability on a timescale of 17 years. This run, like Exp. 5 demonstrates that Arctic freshening in the "Greenland Sea" region does not inhibit interdecadal variability in the simulated thermohaline circulation.

5 Summary and Conclusions

In this thesis, the Bryan-Cox OGCM was used to examine the stability and variability characteristics of the thermohaline circulation. The main aim of this study was to determine if the type of variability that has previously been reported in highly idealized ocean models (e.g., Weaver and Sarachik, 1991*a*,*b*) is robust under steady, non-zonal, surface forcing and realistic geometry. Additionally, the effect of Arctic freshwater flux through both the Canadian Archipelago and the Fram Strait, into the northern North Atlantic, on the thermohaline circulation, was examined.

In an ocean model with realistic geometry, several experiments were carried out using surface forcing fields derived from climatological datasets. In four of the runs fresh water was added to the northernmost grid boxes to simulate Arctic freshwater flux into northern North Atlantic: In Exp. 2 and Exp. 3 the parameterisation was applied to both the "Greenland" and "Labrador Seas", in Exp. 5 it was confined only to the "Greenland Sea" region and in Exp. 6, the effects of Arctic freshwater flux in the "East Greenland Current" region were considered.

This study has demonstrated that non-zonal forcing and realistic geometry give SSS and SST structures that compare quite well with observational data when the Arctic freshwater flux parameterization is included. In the experiment with restoring boundary conditions on SSS the rate of NADW formation was found to be in reasonable agreement with observations. A major shortcoming of the model is the poor reproduction of the structure of the thermocline due to poor representation of vertical mixing.

The experiments with Arctic freshwater flux demonstrate that northern freshening acts

as a fresh water cap and thus pushes the region of deep water formation southward. Forcing the model with freshwater flux derived from the climatological data set of Schmitt et al. (1989) was found to result in rates of NADW formation that were larger than observed estimates. Moore and Reason (1992) found similar results in a model of the global ocean forced by climatological data sets. When the Arctic freshwater flux was doubled it was found that the structure of the zonally-averaged salinity field at high latitudes resembled Levitus (1982) climatological values though the deep ocean was much warmer and saltier in the former. The case with weaker Arctic freshwater flux yielded rates of deep water formation that were large compared to observations.

The first three experiments that were carried out all tended towards steady states. In Exp. 4, however, after a period of initial adjustment, the system settled down to a single-period self-sustained oscillation with a period of about 22 years. The mechanism driving the interdecadal oscillations was closely linked to changes in both the horizontal and vertical extent of convection in the northern "Labrador Sea" and was controlled by the structure of the salinity surface boundary condition. The $E - P$ maximum off the southwestern coast of "Greenland" was found to play a major role in both the initiation and sustenance of the oscillations. In this solution NADW formation was never shut off; associated with the oscillations were changes in the position of the site of maximum overturning in the northern "Labrador Sea" i.e., from the northern boundary during the strongest phase, to the southern "Labrador Sea" region near 63° latitude during the weakest phase of the oscillation. This was reflected in the horizontal velocity field as fluctuations in both the intensity and meridional extent of the branch of the western boundary current which extends into the

"Labrador Sea". The horizontal flow field was found to converge off the southwestern tip of "Greenland" during the weakest phase of the oscillation and at the northern boundary of the domain during the strongest phase reflecting the different regions of deep water formation in this experiment. Fluctuations were also noted in the meridional heat transport which was found to oscillate with amplitude of about 0.3 PW between the phases of maximum and minimum energy. Overturning in the northern "Greenland Sea" remained fairly constant, occuring at more or less the same location, throughout the oscillation.

Other modelling studies have also found variability, in the thermohaline circulation, that persists over long periods of time. In experiments with an idealized ocean model extending over one hemisphere Weaver and Sarachik (1991*b*) found that when the calculations were carried out using double precision, the system remained in a limit cycle for a long time. In other experiments in the same study, Weaver and Sarachik (1992) found that when strong stochastic forcing was applied, the system underwent persistent variability with most of its energy at decadal, interdecadal and longer timescales. In a theoretical study of a simple mixed-layer model Welander (1982) found oscillatory behavior with the system settling in a limit cycle when the Newtonian restoring time scale was faster for temperature than salinity.

The last two experiments that were carried out exhibited variability similar to that in Exp. 4. These experiments, Exp. 5 and Exp. 6, demonstrate that Arctic freshwater flux into the "Greenland Sea" region does not inhibit decadal/interdecadal variability in the model thermohaline circulation. On comparing these results with those for Exp. 2 and Exp. 3 where the Arctic freshwater flux parameterisation was applied to both the "Greenland" and "Labrador Seas" one may infer that when Arctic freshwater flux is added to the "Labrador

Sea" region, decadal/interdecadal variability is inhibited. Addition of Arctic freshwater flux acts to cap the northern "Labrador Sea" region and hence suppress deep water formation. Further, fresh water from the northern source was sufficiently large to dominate over the evaporation in the local region further south. On the other hand, the model that was used in this study had a coarse resolution and the "Labrador sea" was not well resolved; in this region of prominent variability a better resolution would be $1^\circ \times 1^\circ$. Other important omissions in the model include bottom topography and an AABW source.

An important conclusion that can be drawn from this study is that interdecadal variability exists in ocean models even under steady, non-zonal, forcing and realistic geometry. This is of particular climatic importance since there is ample evidence in the literature focussing on observations of climatic variability on decadal/interdecadal time scales as discussed in the introduction. Variations in the thermohaline circulation and hence the poleward heat transport by the ocean would have dramatic implications for the global climate in terms of, for example, feedbacks for greenhouse warming (e.g., Bryan and Spelman 1985). An interesting extension of this work would be inclusion of more realistic coastlines, sea ice, momentum advection, much higher vertical and horizontal resolution, seasonally varying forcing, and a better representation of ocean-atmosphere interactions through surface forcing.

References

Aagaard, K., and E.C. Carmack, 1989: The role of sea ice and other fresh water in the Arctic circulation. *Journal of Geophysical Research.*, **94**, 14,485 – 14,498.

Arakawa, A., and V.R. Lamb, 1977: Computational design of the basic dynamical processes of the UCLA general circulation model. In *Methods in Computational Physics*, **17**, 173 – 265. (J. Chang ed.) Academic press, New York.

Baumgartner, A., and E. Reichel, 1975: The World Water Balance. *Elsevier.* New York.

Boyle, E.A., and L.D. Keigwin, 1982: Deep circulation of the North Atlantic over the past 200,000 years. *Science*, **218**, 784 – 787.

Boyle E.A., and L. Keigwin, 1987: North Atlantic thermohaline circulation during the past 200,000 years linked to high-latitude surface temperture. *Nature*, **330**, 35 – 40.

Brewer, P.G., W.S. Broecker, W.J. Jenkins, P.B. Rhines; C.G. Rooth, J.H. Swift, T. Takahashi, and, R.T. Williams., 1983: A climatic freshening of the deep Atlantic north of York, **222**, 1237 – 1239.

Broecker, W.S., 1979: A revised estimate for the radiocarbon age of North Atlantic Deep Water. *Journal of Geophysical Research.*, **84**, 3218 – 3266.

Broecker, W.S., 1987: Unpleasant surprises in the greenhouse? *Nature*, **328**, 123 – 126.

Broecker, W.S., 1991: The great conveyor, *Oceanography***4**, 79 – 89.

Broecker, W.S., D.M. Peteet, and, D.Rind, 1985: Does the ocean-atmosphere system have more than one stable mode of operation? *Nature*, **315**, 21 – 26.

Broecker, W.S., M. Andree, W. Wolfi, H. Oeschger, Bonini, J. Kennet, and, D. Peteet, 1988: The chronology of the last deglaciation: Implications to the cause of the Younger Dryas event, *Paleoceanogrphy*, **3**, 1 – 19.

Bryan, F., 1986*a*: Maintenance and variability of the thermohaline circulation. Ph.D. thesis, Princeton University, New Jersey, 254pp.

Bryan, F., 1986*b*: High latitude salinity effects and interhemispheric thermohaline circulations. *Nature*, **323**, 301 – 304.

Bryan, F., 1987: Parameter sensitivity of primitive equation ocean general circulation models. *Journal of Physical Oceanography*, **17**, 970 – 985.

Bryan, K., 1962: Measurements of meridional heat transport by ocean currents. *Journal of Geophysical Research*, **67**, 3403 – 3414.

Bryan, K., 1969: A numerical method for the study of the world ocean. *Journal of Computational Physics*, **4**, 347 – 376.

Bryan, K., 1984: Accelerating the convergence to equilibrium of the ocean-climate models. *Journal of Physial Oceanography*, **14**, 666 – 673.

Bryan, K. and M.D. Cox, 1972: An approximate equation of state for numerical models of the ocean circulation. *Journal of Physial Oceanography*, **s**, 510 – 514.

Bryan, K., S. Manabe, and, R.C. Pacanowski, 1975: A global ocean-atmosphere climate model. Part *II*: The oceanic circulation, *Journal of Physical Oceanography*, **5**, 30–46.

Bryan, K. and, M.J., Spelman, 1985: The ocean's response to a CO_2-induced warming. *Journal of Geophysical Research*, **90**, 11679 – 11688.

Bunker, A.F., 1976: Computations of surface energy flux and annual air-sea interaction cycles of the North Atlantic ocean. *Monthly Weather Review*, **104**, 1122 – 1140.

Chamberlin, T.C., 1906: On a possible revresal of deep-sea ciculation and its influence of geological climates. *The Journal of Geology*, **XII**, No.5., 363 – 373.

Clarke, R.A., and J.C. Gascard, 1982: The formation of Labrador water. 1. Large-scale processes. *Journal of Physical Oceanography*, **13**, 1764 – 1778.

Cox, M.D., 1984: A primitive equation, 3-dimensional model of the ocean. GFDL Ocean Group Technical Report No.1., GFDL/NOAA, Princeton University.

Cox, M.D., 1989: An idealised model of the world ocean. Part I: The global-scale water masses. *Journal of Physical Oceanography.*, **20**, 1730 – 1752.

Dickson, R.R., H.H. Lamb, and, J.M. Colebrook, 1975: Climatic reversal in northern North Atlantic. *Nature*, **256**, 479 – 482.

Dickson, R.R., J. Meincke, S. -A. Malmberg; and, A.J. Lee, 1988: The "Great Salinty

Anomaly" in the North Atlantic 1968-1982. *Progress in Oceanography.*, **20**, 103 – 151.

Dorman, C.E., and R.H. Bourke, 1976: Precipitation over the Atlantic Ocean, 30°S to 70°N. *Monthly Weather Review*, **109**, 554 – 563.

Ghil, M., and R. Vautard, 1991: Interdecadal oscillations and the warming trend in global temperature series. *Nature*, **350**, 324 – 327.

Gordon, A.L., 1986: Interocean exchange of thermocline water, *Journal of Geopysical Research*, **91**, 5037 – 5046.

Gordon, A.L., and A.R. Piola, 1983: Atlantic ocean upper layer salinity budget. *American Meteorological Society*, **13**, 1293 – 1300.

Gray, W.M., 1990: Strong association between West African rainfall and United States landfall of intense hurricanes, *Science*, **249**, 1251 – 1256.

Hall, M.M. and H.L. Bryden., 1982: Direct estimates of ocean heat transport. *Deep-Sea Research*, **29**, 339 – 359.

Haney, R.L., 1971: Surface thermal boundary condition for ocean circulation models. *Journal of Physical Oceanography*, **4**, 241 – 248.

Hastenrath, S., 1980: The heat budget of Tropical Ocean and Atmosphere. *Journal of Physical Oceanography*, **10**, 159 – 170.

Hellerman, S., and Rosenstein, M., 1983: Normal monthly wind stress over the world ocean with error estimates. *Journal of Physical Oceanography*, **13**, 1093 – 1104.

Hibler III, W.D., and S.J. Johnsen, 1979: The 20-year cycle in Greenland ice core records. *Nature*, **280**, 481 – 483

Hughes, T.M.C., A.J. Weaver, and, J.S. Godfrey, 1992: Thermohaline forcing of the Pacific Ocean by the Indian Ocean. *Deep-Sea Research* , in press.

Ikeda, M., 1990: Decadal oscillations of the air-ice-ocean system in the northern hemisphere, *Atmosphere-Ocean*, **28**, 106 – 139.

James, N., and P.M. James, 1989: Ultra-low frequency variability in a simple atmospheric circulation model. *Nature*, **342**, 53 – 55.

Killworth, P.D., 1979; On "Chimney" formations in the ocean. *Journal of Physical Oceanography.*, **9**, 531 – 554.

Killworth, P.D., 1983: Deep convection in the world ocean. *Reviews of Geophysics and Space Physics*, **21**, 1 – 26.

Krishnamurti, T.N., S-H Chu, and W. Iglesias., 1986: On the sea level pressure of the southern oscillation, *Archives for Meteorology, Geophysics and Bioclimatology, Series*, **A34**, 385 – 425.

Lazier, R.N., 1973: The renewal of Labrador Sea water. *Deep Sea Research*, **20**: 341 – 351.

Lazier, J.R.N., 1980: Oceanographic conditions at O.W.S. Bravo 1964 – 1974 *Atmosphere-Ocean*, **18**, 227 – 238.

Lazier, M., 1988: Temperature and salinity changes in the deep Labrador Sea, 1962 – 1986. *Deep Sea Research*, **35**, 1247 – 1253.

Levitus, S., 1982: Climatological Atlas of the World Ocean. NOAA Professional paper 13, U.S. Department of Commerce: National Oceanic and Atmospheric Administration.

Levitus, S., 1989: Interpentadal variability of temperature and salinity at intermediate depths of the North Atlantic ocean, 1970 – 1974 versus 1955 – 1959. *Journal of Geophysical Research*, **94**, 6091 – 6131.

Lorenz, E.N., 1990: Can chaos and intransitivity lead to interannual variability? *Tellus*, **42A**, 378 – 389.

Maier-Reimer, E., and U. Mikolajewicz., 1989: Experiments with an OGCM on the cause of the Younger Dryas. Report No. 39, Max-Planck-Institut fur Meteorologie, Hamburg. Reprinted from: *Oceanography*, 1988 (Eds.: Ayala-Casternares, W. Wooster and A. Yanez-Arancibia), UNAM Press, Mexico D.F., 87 – 100.

Malmberg, S-A., 1969: Hydrographic changes in the waters between Iceland and Jan Mayen in the last decade. *Jokull*, **19**, 30 – 43.

Mantyla, A.W., and J.L. Reid, 1983: Abyssal characteristics of the world ocean waters. *Deep Sea Research.*, **30**, 805 – 833.

Marotzke, J., 1989: Instabilities and multiple steady states of the thermohaline circulation.

In *Oceanic Circulation Models: Combining Data and Dynamics*, D.L.T. Anderson and J.Willebrand, Eds., ASI Series, Kluwer, 501 – 111.

Marotzke, J., 1991: Influence of convective adjustment on the stability of the thermohaline circulation, *Journal of Physical Oceanography*, **21**, 903 – 907.

Marotzke, J., and J. Willebrand, 1991: Multiple equilibria of the global thermohaline circulation, *Journal of Physical Oceanography*, **21**, 1372 – 1385.

Marotzke, J, P. Welander, and, J. Willebrand., 1988: Instability and multiple steady states in a meridional-plane model of the thermohaline circulation. *Tellus*, **40A**, 162 – 172.

Moore, A.M., and C.J.C. Reason, 1992: The response of an ocean general circulation model to climatological surface boundary conditions for temperature and salinity. Submitted to *Journal of Physical Oceanography.*

Myers, P.G., and A.J. Weaver., 1992: Low-frequency internal variability under seasonal forcing. *Journal of Geophysical Research*, **97**, in press.

Mysak, L.A., and D.K. Manak, 1989: Arctic sea-ice extent and anomalies, 1953 – 1984, *Atmosphere-ocean*, **27**, 376 – 405.

Mysak, L.A.; D.K. Manak; and, R.F. Marsden, 1990: Sea-ice anomalies observed in the Greenland and Labrador Seas during 1901 – 1984 and their relation to an interdecadal Arctic climate cycle. *Climate Dynamics*, **5**, 111 – 133.

Nicholson, S.E., 1986: *Journal of Climate and Applied Meteorology*, **25**, 1365 – 1381.

Reid, J.L, and R.J. Lynn, 1971: On the influence of the Norwegian-Greenland and Weddel Seas upon the bottom waters of the Indian and Pacific Oceans. *Deep Sea Research*, **18**, 1063 – 1088.

Rooth, C., 1982: Hydrology and ocean circulation, *Progress in Oceanography*, **11**, 131 – 149.

Rudels, B., D. Quadfasel, H. Freidrich, and, M. -N. Houssais, 1989: Journal of Geophysical Research., **94**, 3223 – 3227.

Ruddiman, W.F., and A. McIntyre, 1981: Oceanic mechanisms for the amplification of the 23,000 year ice-volume cycle. *Science*, **212**, 617 – 627.

Schmitt, R.W., P.S. Bogden, and, C.E. Dorman, 1989: Evaporation minus precipitation and density fluxes for the North Atlantic. *Journal of Physical Oceanography*, **19**, 1208 – 1221.

Semtner, A.J., 1974: An oceanic general circulation model with bottom topography. *Numerical simulations of weather and climate*, Tech. Rept. No. 9, Department of Meteorology University of California, Los Angeles, 99 pp.

Siegenthaler, U., and T. Wenk, 1984: Rapid atmospheric CO_2 variations and ocean circulation. *Nature*, **308**, 624 – 626.

Stocker, T.F., and D.G. Wright, 1991: Rapid transitions of the ocean's deep ciculation and climate change. *Nature*, **351**, 729 – 732.

Stommel, H., 1961: Thermohaline convection with two stable regimes of flow. *Tellus*, **13**, 225 – 230.

Street-Perrot, F.A; and, R.A. Perrot, 1990: Abrupt climate fluctuations in the tropics: the influence of Atlantic ocean circulation, *Nature*, **343**, 607 – 612.

Swift, J.H., 1984: A recent $\Theta - S$ shift in the deep water of the northern North Atlantic. In *Climate Processes and Climate Sensitivity*, J.E. Hansen and T. Takahashi, editors, Geophysical Monograph 29, Maurice Ewing, vol. **5**. American Geophysics, University of Washington, D.C., pp39 – 47.

Toggweiler, J.R.; K. Dixon; and, K. Bryan, 1989: Simulations of radiocarbon in a coarse resolution world ocean model 2. Distributions of bomb-produced carbon 14. *Journal of Geophysical research*, **94**, 8243 – 8264.

Veronis, G., 1975: The role of models in tracer studies. In *Numerical Models of Ocean circulation*. National Academy of Science. pp133 – 146.

Vinje, T.E., 1970: Sea ice observations in 1968. *Arbok Norsk Polarinsk* 1968: 95 – 100.

Walsh, J.E. and C.M. Johnson., 1979: An analysis of Arctic sea ice fluctuations. *Journal of Physical Oceanography*, **9**, 580 – 591.

Warren B.A., 1981: Deep circulation of the World Ocean. *Evolution of Physical Oceanography*, B.A Warren and C. Wunsch, Eds., MIT Press, 6 – 41.

Warren, B.A., 1983: Why is no deep water formed in the North Pacific?, *Journal of Marine Research*, 41, 327 – 347.

Weaver, A.J., and E.S. Sarachik, 1990: On the importance of vertical resolution in certain ocean general circulation models. *Journal of Physical Oceanography*, 20, 600 – 609.

Weaver, A.J., and E.S. Sarachik, 1991*a*: The role of mixed boundary conditions in numerical models of the ocean climate. *Journal of Physical Oceanography*, 21, 1470 – 1493.

Weaver A.J., and E.S. Sarachik, 1991*b*: Evidence for decadal variability in an ocean general circulation model: An advective mechanism. *Atmosphere-Ocean*, 29, 197 – 231.

Weaver, A.J, and T.M.C. Hughes 1992: Stability and variability of the thermohaline circulation and its links to climate. Centre for Climate and Glogal Change Research (C^2GCR) Report No. 92 – 5, Department of Atmospheric and Oceanic Sciences, McGill University.

Weaver A.J., E.S Sarachik, and, J. Marotzke, 1991: Internal low frequency variability of the ocean's thermohaline circulation. *Nature*, 353, 836 – 838.

Weaver A.J., J. Marotzke, P.F. Cummins, and, E.S. Sarachik, 1992: Stability and variability of the thermohaline circulation. *Journal of Physical Oceanography*, in press.

Welander, P., 1982: A simple heat oscillator. *Dynamics of atmosphere and oceans*, 6, 233 – 242.

Welander, P., 1986: Thermohaline effects in the ocean circulation and related simple models, In *Large Scale Transport Processes in Oceans and Atmosphere*, Eds., J. Willebrand and D.L.T. Andersen, D. Reidel Publishing Company, 163 – 200.

Wright, D.G., and T.F. Stocker, 1991: A zonally averaged ocean model of!the thermohaline circulation, parts I and II. *Journal of Physical Oceanography*, 21, 1731 – 1739.